

# **Nuclear magnetic resonance on a single quantum dot and a quantum dot in a nanowire system: quantum photonics and opto-mechanical coupling**

**Inauguraldissertation**

zur

Erlangung der Würde eines Doktors der Philosophie

vorgelegt der

Philosophisch-Naturwissenschaftlichen Fakultät

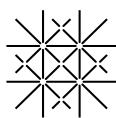
der Universität Basel

von

**Gunter Wüst**

aus Freckenfeld, Deutschland

Basel, 2015



**Universität  
Basel**

---

Originaldokument gespeichert auf dem Dokumentenserver der Universität Basel

[edoc.unibas.ch](http://edoc.unibas.ch)

Genehmigt von der Philosophisch-Naturwissenschaftlichen Fakultät auf Antrag von

Prof. Dr. Richard J. Warburton

Prof. Dr. Val Zwiller

Basel, den 19.05.2015

Prof. Dr. Jörg Schibler  
Dekan

Dies ist eine alltagssprachliche Zusammenfassung der **Lizenz** (die diese nicht ersetzt).

[Haftungsbeschränkung](#)

#### Sie dürfen:

**Teilen** — das Material in jedwedem Format oder Medium vervielfältigen und weiterverbreiten

Der Lizenzgeber kann diese Freiheiten nicht widerrufen solange Sie sich an die Lizenzbedingungen halten.

#### Unter folgenden Bedingungen:



**Namensnennung** — Sie müssen **angemessene Urheber- und Rechteangaben machen**, einen Link zur Lizenz beifügen und angeben, ob **Änderungen vorgenommen** wurden. Diese Angaben dürfen in jeder angemessenen Art und Weise gemacht werden, allerdings nicht so, dass der Eindruck entsteht, der Lizenzgeber unterstütze gerade Sie oder Ihre Nutzung besonders.



**Nicht kommerziell** — Sie dürfen das Material nicht für **kommerzielle Zwecke** nutzen.



**Keine Bearbeitungen** — Wenn Sie das Material **remixen, verändern oder darauf anderweitig direkt aufbauen** dürfen Sie die bearbeitete Fassung der Materials nicht verbreiten.

**Keine weiteren Einschränkungen** — Sie dürfen keine zusätzlichen Klauseln oder **technische Verfahren** einsetzen, die anderen rechtlich irgendetwas untersagen, was die Lizenz erlaubt.

#### Hinweise:

Sie müssen sich nicht an diese Lizenz halten hinsichtlich solcher Teile des Materials, die gemeinfrei sind, oder soweit Ihre Nutzungshandlungen durch **Ausnahmen und Schranken des Urheberrechts** gedeckt sind.

Es werden keine Garantien gegeben und auch keine Gewähr geleistet. Die Lizenz verschafft Ihnen möglicherweise nicht alle Erlaubnisse, die Sie für die jeweilige Nutzung brauchen. Es können beispielsweise andere Rechte wie **Persönlichkeits- und Datenschutzrechte** zu beachten sein, die Ihre Nutzung des Materials entsprechend beschränken.



# Contents

|          |   |           |
|----------|---|-----------|
| <b>1</b> | <b>Introduction</b>   | <b>1</b>  |
| 1.1      | Optical properties . . . . .  | 1         |
| 1.2      | Quantum dot growth and sample design . . . . .  | 3         |
| 1.3      | Single spins in a quantum dot . . . . .   | 4         |
| 1.4      | Nuclear spins in quantum dots . . . . .   | 5         |
| 1.5      | Quantum dots in nanowires . . . . .   | 7         |
| 1.6      | Opto-mechanical coupling . . . . .  | 7         |
|          | References . . . . .  | 10        |
| <b>2</b> | <b>Manipulation of the nuclear spin ensemble in a quantum dot using chirped magnetic resonance pulses</b> | <b>11</b> |
| 2.1      | Introduction . . . . .  | 13        |
| 2.2      | Concepts and experimental realization . . . . .   | 13        |
| 2.2.1    | Adiabatic passage: The Landau-Zener-Problem . . . . .   | 13        |
| 2.2.2    | Experimental setup . . . . .  | 14        |
| 2.3      | Reading and setting the nuclear spin polarization using the dragging effect                               | 16        |
| 2.4      | Manipulation of the nuclear spin ensemble . . . . .   | 16        |
| 2.5      | Chemical composition and nuclear spin temperature . . . . .   | 17        |
| 2.6      | Spectroscopic measurements and quadrupole frequency distributions . . .                                   | 19        |
| 2.7      | Conclusions . . . . .   | 22        |
|          | References . . . . .  | 24        |
| <b>3</b> | <b>Nuclear spin coherence in a quantum dot</b>  | <b>25</b> |
| 3.1      | Introduction . . . . .  | 26        |
| 3.2      | Concept and experimental cycle . . . . .  | 27        |
| 3.3      | Coherence of the nuclear spin ensemble under the influence of QD charge                                   | 29        |
| 3.4      | Conclusion and Outlook . . . . .  | 34        |
|          | References . . . . .  | 35        |

|          |   |           |
|----------|---|-----------|
| <b>4</b> | <b>Bright source of red single photons from a new quantum-dot-in-nanowire system</b>    | <b>37</b> |
| 4.1      | Introduction . . . . .  | 38        |
| 4.2      | The quantum-dot-in-nanowire-system . . . . .  | 38        |
| 4.3      | Optical characterization . . . . .  | 42        |
| 4.3.1    | Localizing single emitters . . . . .  | 42        |
| 4.3.2    | Analysing the photoluminescence polarization . . . . .                                  | 43        |
| 4.3.3    | Characterizing the single photon emission . . . . .                                     | 44        |
| 4.4      | Theory of the quantum confinement . . . . .   | 48        |
| 4.4.1    | Pseudopotential calculations . . . . .  | 48        |
| 4.4.2    | Density functional theory calculations . . . . .  | 49        |
| 4.5      | Conclusion . . . . .  | 50        |
|          | References . . . . .  | 54        |
| <b>5</b> | <b>Quantum Dot Opto-Mechanics in a Fully Self-Assembled Nanowire</b>                    | <b>55</b> |
| 5.1      | Introduction . . . . .  | 56        |
| 5.2      | Experimental setup . . . . .  | 57        |
| 5.3      | Interferometry: Calibrating the motion of the nanowire free end . . . . .               | 58        |
| 5.4      | Spectrally resolved confocal photoluminescence imaging . . . . .                        | 60        |
| 5.5      | Opto-mechanical coupling . . . . .  | 61        |
| 5.5.1    | The effect of nanowire excitation on the quantum dot photoluminescence . . . . .        | 61        |
| 5.5.2    | Determining the opto-mechanical coupling strength . . . . .                             | 62        |
| 5.5.3    | Stroboscopic measurement: Time evolution of the quantum dot photoluminescence . . . . . | 64        |
| 5.6      | Conclusion . . . . .  | 65        |
|          | References . . . . .  | 71        |
| <b>6</b> | <b>Conclusions and outlook</b>  | <b>73</b> |
| <b>A</b> | <b>Supplementary information to chapter 2</b>   | <b>75</b> |
| A.1      | Experimental details . . . . .  | 75        |
| A.1.1    | Sample . . . . .  | 75        |
| A.1.2    | Set-up . . . . .  | 77        |
| A.2      | Supporting experimental results . . . . .   | 78        |
| A.2.1    | Depolarization procedure . . . . .  | 78        |
| A.2.2    | Nuclear-spin lifetime . . . . .   | 79        |

|            |  |            |
|------------|--|------------|
| A.2.3      | Measurement of Rabi oscillations and estimate of $B_x$ . . . . .   | 80         |
| A.3        | Theory . . . . .   | 81         |
| A.3.1      | Concepts . . . . .   | 81         |
| A.3.2      | Quantitative analysis . . . . .                                    | 85         |
| A.3.3      | Discussion and conclusions . . . . .                               | 89         |
| A.3.4      | Nuclear spin temperature . . . . .                                 | 92         |
| References | . . . . .  | 95         |
| <b>B</b>   | <b>Supplementary information to chapter 3</b>                      | <b>97</b>  |
| B.1        | Supporting experimental results . . . . .                          | 97         |
| B.1.1      | Hight accuracy measurement of the central NMR transition . . . . . | 97         |
| B.1.2      | Gate switching bandwidth . . . . .                                 | 97         |
| B.1.3      | g-factors and branching ratio . . . . .                            | 99         |
| B.2        | Theory: Decoherence of the nuclear spin ensemble . . . . .         | 100        |
| B.2.1      | Decoherence rate of a single nuclear spin . . . . .                | 100        |
| B.2.2      | Coherence rate of a NMR signal . . . . .                           | 102        |
| References | . . . . .  | 103        |
| <b>C</b>   | <b>Supplementary information to chapter 4</b>                      | <b>105</b> |
| C.1        | Methods . . . . .  | 105        |
| References | . . . . .  | 107        |
| <b>D</b>   | <b>Supplementary information to chapter 5</b>                      | <b>109</b> |
| D.1        | Mechanical properties of the nanowire . . . . .                    | 109        |
| D.2        | Effect of strain on the exciton transition energy . . . . .        | 112        |
| D.3        | Distribution of the exciton energy shifts . . . . .                | 113        |
| D.4        | Interferometric displacement detection . . . . .                   | 115        |
| D.5        | Displacement, force, and strain sensitivities . . . . .            | 116        |
| References | . . . . .  | 117        |
|            | <b>Acknowledgements</b>  | <b>119</b> |
|            | <b>Curriculum Vitae</b>  | <b>120</b> |
|            | <b>List of Publications</b>  | <b>123</b> |





# Chapter 1

## Introduction

Self-assembled semiconductor quantum dots (QDs) are nano-sized islands of semiconductor material with a smaller band gap than the host material they are embedded in<sup>1</sup> (Fig. 1.1). The resulting 3D confining potential is a trap for single electrons or holes, whose spin states represent a solid state qubit<sup>2,3</sup>. Furthermore, they are high-brightness, narrow linewidth single photon sources<sup>4</sup>. These properties make QDs very attractive for exploring fundamental quantum physics and, if the issue of decoherence<sup>5</sup> and scaling up can be addressed, possible building blocks for quantum information processing<sup>6,7</sup> and quantum computation applications<sup>2</sup>.

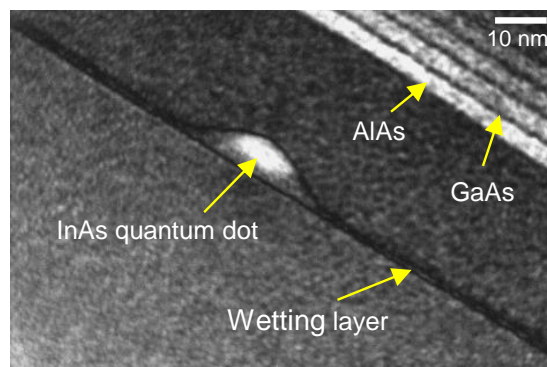


Fig. 1.1. Transmission electron microscopy image of a single InAs quantum dot embedded in charge tunable heterostructure. Courtesy of Jean-Michel Cauveau and Arne Ludwig.

### 1.1 Optical properties

In crystalline solids electrons are described by Bloch waves<sup>8</sup> ( $\psi = \exp(ikx) \cdot u(x)$ ), the product of a plain wave with a periodic function ( $u(x)$ ) reflecting the crystal periodicity. Electronic and optical properties of solids can be explained with a band structure model<sup>9</sup>.

Here, energy bands are plotted as a function of electron momentum  $E = E(k)$ . InAs and GaAs are direct band gap semiconductors, meaning the global conduction band minimum lies directly “above” the global valence band maxima at  $k = 0$ , the so called  $\Gamma$ -point. Hence the radiative recombination of an electron with a hole takes place without involving a phonon. Around the  $\Gamma$ -Point the dispersion relations can be approximated by a parabolas  $E \simeq \hbar^2 k^2 / 2m^*$ , where the solid state properties are included in the effective mass  $m^*$  (Fig. 1.2 (a)). In III-V-semiconductors the conduction (valence) band is composed of atomic s-orbitals (p-orbitals). Spin-orbit coupling splits the  $J = 1/2$  from the  $J = 3/2$  bands by  $E_{SO}$ . The  $J = 3/2$  band again is split into two bands, the light hole band ( $m_j = \pm 1/2$ ) and heavy hole band ( $m_j = \pm 3/2$ ). The confinement of the QD causes them to split by  $E_c$ , thus spontaneous emission only occurs from electron-heavy hole recombination. Furthermore, the confinement quantizes the plane wave part of the Bloch functions, resulting in a few discrete energy levels in the dot<sup>1</sup> (Fig. 1.2(b)).

These properties can be exploited to build a two level quantum system<sup>10</sup>, where the vacuum ground state  $|0\rangle$  is coupled via a dipole transition to the excited state  $|X^0\rangle$ , consisting of a electron hole pair (exciton) bound to the QD. Exciting the transition with a coherent laser and detecting either the transmission signal or resonance fluorescence revealed all the textbook phenomena<sup>10</sup> expected for a driven two level atom. Lorentzian

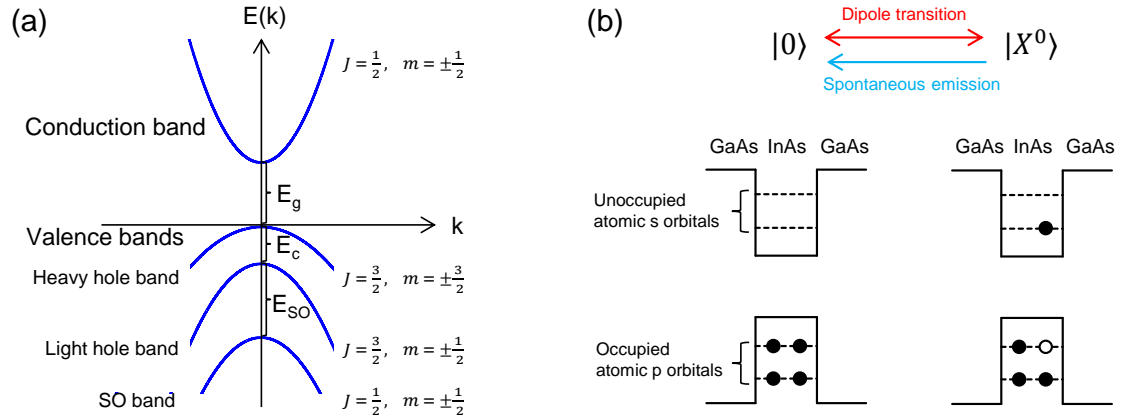


Fig. 1.2. **Schematic band structure of a quantum dot.** (a) Simplified band structure around the  $\Gamma$  point for a direct semiconductor. In the  $\mathbf{k} \cdot \mathbf{p}$  model the energy wave vector relation is parabolic with one over the effective masses as pre-factors. The conduction (valence) band is composed of atomic s (p) orbitals. Due to the spin-orbit interaction the  $J = \frac{1}{2}$  band is split by  $E_{SO}$ . Strain and the strong confining potential split the heavy hole and light hole band by  $E_c$ . (b) 3D confinement resulting from the smaller band gap of InAs leads to quantized energy levels for electrons and holes.  $|0\rangle$  and  $|X^0\rangle$  form a two level quantum system coupled by an optical dipole transition and spontaneous emission.

lineshapes<sup>11</sup>, power broadening, power induced transparency<sup>12</sup>; Rabi oscillations<sup>4</sup>, the Molov triplet and anti-bunched resonance fluorescence<sup>4</sup> have been observed. Typically, the emission wavelength is around 950 nm and the emission rate is around 1 GHz<sup>13</sup>, corresponding to a dipole moment of  $\sim 0.5$  nm $\cdot$ e, where e is the electronic charge. The energy state separation for electrons and holes confined to the dot is on the order of few 10s of meV, large compared to the thermal energy of 0.36 meV at  $T = 4.2$  K. Consequently, many spin experiments can be carried out in a simple bath cryostat.

## 1.2 Quantum dot growth and sample design

The workhorse system consists of InGaAs QDs surrounded by a GaAs matrix. These devices are fabricated by molecular beam epitaxy (MBE) in the Stranski-Krastanov mode. Here, strain due to the lattice mismatch between InAs and GaAs is the driving force behind the self-assembly process, which starts after  $\sim 1.5$  monolayers of InAs<sup>14</sup> are deposited on GaAs. The resulting lens shaped QDs vary in size from dot to dot with a typical height of  $\sim 5$  nm along the growth direction and a diameter of  $\sim 20$  nm. A film of InAs, the so-called wetting layer remains, forming a continuum for non-resonant excitation. Ga diffusion into the dot, enabled by annealing during or after the growth,

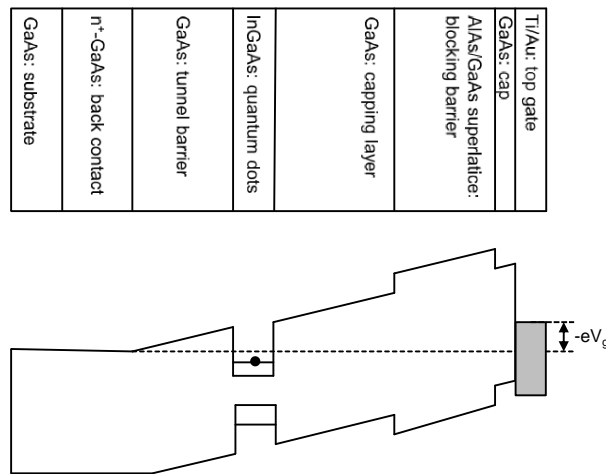


Fig. 1.3. **Sample design.** Layer structure (top) and corresponding band structure (bottom) are shown. Quantum dots are tunnel coupled to the Fermi sea of the highly doped back contact. The dashed line indicates the Fermi Energy. Current flow is prevented by the blocking barrier, hence the device acts like a plate capacitor. By varying the gate voltage  $V_g$  between top gate and back contact one can select the occupancy with electrons.

is exploited to fine tune the confining potential and hence optical emission wavelength. Techniques from the semiconductor industry are available to alter the photonic and electric environment. Post growth processing such as etching and lithography add to the design toolbox. The QDs investigated in the first two chapters of this thesis are embedded in a charge tunable device<sup>15</sup> (Fig. 1.3). Here, electrons from the highly  $n^+$ -doped back contact can tunnel through a small barrier into the dot. This process is controlled by adjusting the QD energy levels relative to the Fermi energy of the back contact. Setting the gate voltage  $V_g$  charges the QD ground state with 1, 2 or 3 electrons. The blocking barrier prevents current flow, making the device act as a plate capacitor. Fine tuning of the exciton resonance is achieved by exploiting the Stark effect.

### 1.3 Single spins in a quantum dot

In principle the vacuum state  $|0\rangle$  and the neutral exciton  $|X^0\rangle$  form a quantum two level system. However, the coherence is limited to the ns time scale due to the rapid radiative decay. Hence all quantum operations must be carried out on the ps time scale with ultra fast optics. An alternative route is to use the spin of an electron (or hole spin) trapped to the QD as a natural qubit<sup>2</sup>. In this case the exciton ground state  $|e^-\rangle$  consists of one electron and the excited trion state  $|X^{1-}\rangle$  consists of one hole and two electrons in a singlet state (Fig. 1.4(a)). Applying an external magnetic field  $B_0$

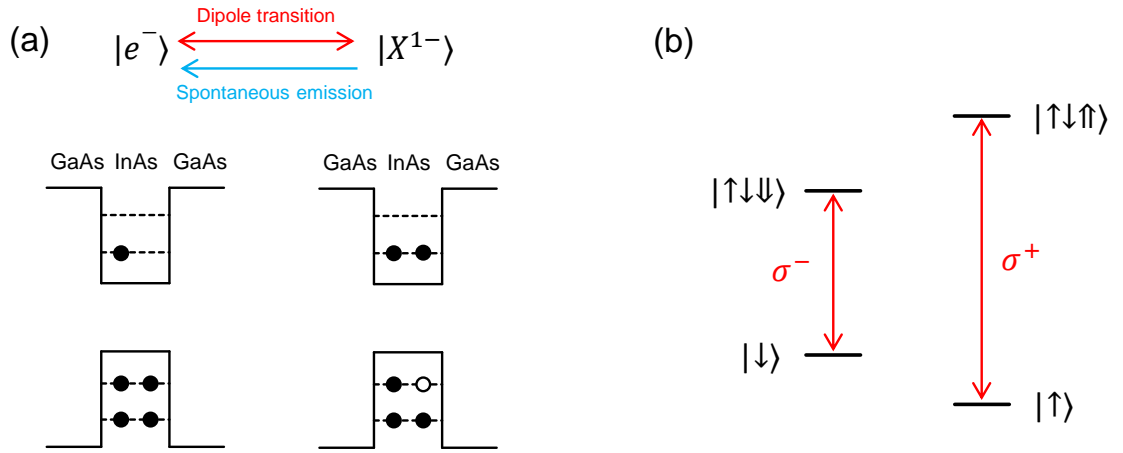


Fig. 1.4. **Singly charged quantum dot.** (a) The ground state  $|e^-\rangle$  consists of one electron, the excited state  $|X^{1-}\rangle$  of two electrons and one hole. (b) A magnetic field  $B_0$  along the growth direction lifts the spine degeneracy.  $|\uparrow\rangle$ ,  $|\downarrow\rangle$  ( $|\uparrow\uparrow\rangle$ ,  $|\downarrow\downarrow\rangle$ ) denotes the electron (hole) spin states. According to the optical selection rules only vertical transitions with the indicated circular polarization are allowed.

along the growth direction splits the electron spin states  $|\uparrow\rangle$  and  $|\downarrow\rangle$  by the electron Zeeman energy  $E_z^e = g_e \mu_B B_0$ , with  $g_e$  the electron g factor and  $\mu_B$  the Bohr magneton. Correspondingly, the trion states are split by the hole Zeeman energy  $E_z^h = g_h \mu_B B_0$ , with  $g_h$  being the hole g factor and  $|\uparrow\rangle, |\downarrow\rangle$  denoting the hole spin states (Fig. 1.4(b)). Since the heavy holes are spin 3/2 particles (Fig. 1.2(a)) the optical selection rules only permit transitions between  $|\downarrow\rangle \longleftrightarrow |\uparrow\downarrow\downarrow\rangle$  ( $\sigma^-$ -polarized) and  $|\uparrow\rangle \longleftrightarrow |\uparrow\downarrow\uparrow\rangle$  ( $\sigma^+$ -polarized). Thus the transitions are specific in energy and polarization. Likewise, level diagrams with the according selection rules can be constructed for in-plane magnetic fields and dots charged with a single excess hole<sup>3</sup>. Electron and hole spins have been initialized with close to unity fidelity via optical pumping schemes<sup>16–18</sup>. Furthermore, electron spin manipulation with detuned laser pulses has been achieved on the 10 ps time scale<sup>19,20</sup>. Also, conventional electron spin experiments with an alternating magnetic field have been carried out on single quantum dots<sup>17</sup>. However, there is a need for experimental improvements increasing the amplitude of the alternating  $B$  field to speed up the electron spin rotations.

## 1.4 Nuclear spins in quantum dots

Self-assembled quantum dots are often referred to as artificial atoms. This is true in the sense that they possess discrete energy levels and mimic two level atom behaviour. However, since they vary in size and composition they are not indistinguishable. Furthermore, the trapped particle's interaction with the solid state environment leads to decoherence<sup>21</sup>. A major crux is the interaction of the electron spin with  $N \sim 10^5$  nuclear spins of the QD. Since the electron wavefunction is composed of atomic s-orbitals the interaction is described by the Fermi contact Hamiltonian:

$$H_{hf}^e = \sum_k^N A_k \mathbf{S} \cdot \mathbf{I}_k, \quad (1.1)$$

where  $\mathbf{S}$  ( $\mathbf{I}$ ) is the electron (nuclear) spin operator and  $A_k$  is the coupling coefficient of the  $k^{\text{th}}$  nuclei<sup>22</sup>. The effect of polarized nuclear spins is described by the Overhauser field  $B_N$ , which is added to the external field, enabling read-out of the nuclear spin polarization by changes in the exciton resonance position<sup>23</sup>. The effect of electron spin polarization on the nuclei is described by the Knight field and flip-flop processes allow spin transfer between electron to nuclei. Thus, nuclear spins can be polarized optically, a process known as dynamic nuclear spin polarization (DNSP). Dipolar coupling between the nuclei leads to fluctuations in  $B_N$ . For large  $N$  one can assume a Gaussian distribu-

tion of  $B_N$ , with a standard deviation  $\sigma_N = B_N^{max}/\sqrt{N}^{24}$ . Due to the mesoscopic size of the ensemble the fluctuations are on the order of  $\sim 10$  mT. This is small compared to the external fields of a few Tesla and thus fluctuations perpendicular to  $B_0$  are not a relevant source of electron spin relaxation. However, fluctuations parallel to  $B_0$  represent a jitter on the electron spin state precession and thus result in fast dephasing. Fully polarizing the nuclear spin ensemble is one route to prolong electron spin coherence, but so far only polarizations degrees of  $\sim 50\%$  have been achieved<sup>25</sup>. It is currently unknown what hinders higher polarizations. Active feedback schemes have extended electron dephasing times up  $\sim 1\mu\text{s}$ .<sup>26</sup> However, the technique is complex. Enhanced experimental resources are needed to tackle these issues. An Alternative route is to use the hole spin states split in an in-plane magnetic field as a qubit basis<sup>3,27</sup>. Here, the hyperfine interaction is strongly reduced since the hole wavefunction is composed of atomic p-orbitals (Fig. 1.2(a)).

In the first two chapters we implement nano-scale nuclear magnetic resources on a single quantum dot. The nuclear spin ensemble is highly inhomogeneous: there are four different main isotopes with different gyromagnetic ratios; spin numbers are 3/2 for As, Ga and 9/2 for In; the highly stained nature of the QD leads to large atom depended quadrupolar shifts. Our method is to apply chirped pulses to address each transition at some point of the sweep. To generate the high radio frequency (RF) field amplitudes ( $\sim 5$  mT) needed for efficient manipulation a low impedance high bandwidth microwire structure was added to the standard device design. We are able to invert the ensemble polarization with an efficiency of 72%. Varying the the pulse duration combined with isotope selective measurements determines the key parameters of the ensemble: chemical composition; effective nuclear spin temperatures, inversion efficiencies and quadrupolar frequency distributions for each isotope.

In chapter 3 we use chirped NMR pulses to maximize the population difference between the  $+1/2$  and  $-1/2$  state and hence boost the signal from the central transition to a detectable level. This enabled pulsed NMR measurements determining isotope selective nuclear coherence times  $T_2$ . For uncharged QDs we find  $T_2 \sim 5$  ms. This is explained by the suppression of the nuclear dipole-dipole interaction due to a second order quadrupolar effect. When charged with a single electron  $T_2$  drops by more than two orders of magnitude. We explain this observation by RKKY interactions, a second order process where nuclear spin flip-flops are mediated by the electron spin. This is confirmed by the recovery of  $T_2$  when the dot is charged with two electrons forming a spin singlet state.

## 1.5 Quantum dots in nanowires

Due to the high refractive index of GaAs ( $\sim 3.5$  at 950 nm) total reflection at the semiconductor vacuum interface occurs already at small angles ( $\sim 17^\circ$ ). Thus one major challenge for using semiconductor quantum dots as single photon sources is to efficiently extract the light from the sample. This issue can be addressed by tailoring the photonic environment. A quantum dot in a nanowire couples efficiently to the guided (Gaussian-like) mode of the wire and extraction can be achieved by adiabatically tapering the wire<sup>28</sup>. However, the top down fabrication is complex. In chapter 4 we investigate the photonic properties from a fully self-assembled quantum dot in a GaAs/AlGaAs core shell nanowire (NW) structure. We note that the QD self-assembly is driven by segregation processes rather than strain. Depending on the core shell structure the hexagonal cross section is several hundred nm thick and the NWs are typically a few tens of  $\mu\text{m}$  long. The quantum dots consist of AlGaAs island with low As concentration surrounded by a AlGaAs barrier with high As concentration and typically emit in the range of 650-730 nm. Interestingly, this is at a shorter wavelength than emission from the nearby continuum formed by the GaAs core ( $\sim 830$  nm). Experiments under non-resonant excitation exhibit narrow emission lines (FWHM  $\sim 30$   $\mu\text{eV}$ ), close to the resolution limit of our spectrometer. Pulsed and continuous wave time correlated single photon counting reveal the highly anti-bunched ( $g^{(2)}(t=0) \leq 2\%$ ) nature of the emission. Also, the CW measurement shows the signature of a pure two level atom with no additional levels. Decay curve measurements following pulsed excitation confirm the radiative lifetime of  $\sim 0.5$  ns. Single photon count rates of exceeding 1 MHz are measured close to saturation.

## 1.6 Opto-mechanical coupling

Due to their small size NWs are natural choice as AFM tips. The nanowires can be functionalized to enhance sensitivity to electric or magnetic environments. In chapter 5 we investigate energy shifts in the quantum dot photoluminescence under the influence of mechanical motion of the nanowire. To do so, we glue individual NWs on the edge of a silicon chip and mount the chip on a piezoelectric transducer (PZT). The mechanical modes of oscillation of the NW are excited by driving the PZT at the resonance frequency of the NW ( $\nu_0 \sim 0.5\text{-}1$  MHz). This results in tensile/compressive stress, strongest close to the clamping. Stress alters the lattice constant and consequently changes the band gap, thus establishing a coupling mechanism between the NW motion and QD emission energy. Large energy modulations exceeding 14 meV have been observed. Following in-

terferometric calibration of the NW's free end motion we determine the opto-mechanical coupling rate  $\lambda = 66 \pm 12$  kHz, similar to the value measured by Yeo *et al.*<sup>29</sup>. Enhancing  $\nu_0/\lambda$  to or above unity would enable a quantum non-demolition readout of the QD exciton state by detecting the free-end motion of the NW. Furthermore, stroboscopic measurements show that different QDs within the focal spot of the microscope can be dynamically tuned into resonance, a possible route to emitter-emitter coupling. Furthermore, for sensing applications reading the QD emission energy is an alternative way to detect the nanowire motion.



## References

1. Warburton, R. J. *Contemporary Physics* **43**, 351–364 (2002).
2. Loss, D. and DiVincenzo, D. P. *Phys. Rev. A* **57**, 120–126 (1998).
3. Warburton, R. J. *Nature Materials* **12**, 483 – 493 (2013).
4. Muller, A., Flagg, E. B., Bianucci, P., Wang, X. Y., Deppe, D. G., Ma, W., Zhang, J., Salamo, G. J., Xiao, M., and Shih, C. K. *Phys. Rev. Lett.* **99**, 187402 (2007).
5. Fischer, J. and Loss, D. *Science* **324**, 1277–1278 (2009).
6. Imamoglu, A., Awschalom, D. D., Burkard, G., DiVincenzo, D. P., Loss, D., Sherwin, M., and Small, A. *Phys. Rev. Lett.* **83**, 4204–4207 (1999).
7. Zheng, S.-B. and Guo, G.-C. *Phys. Rev. Lett.* **85**, 2392–2395 (2000).
8. Bloch, F. *Zeitschrift für Physik A* **52**, 555–600 (1929).
9. Kittel, C. *Introduction to Solid State Physics*. John Wiley & Sons, Inc., 6th edition, (1986).
10. Loudon, R. *The Quantum Theory of Light*. Oxford University Press, (1992).
11. Hogele, A., Seidl, S., Kroner, M., Karrai, K., Warburton, R. J., Gerardot, B. D., and Petroff, P. M. *Phys. Rev. Lett.* **93**, 217401 (2004).
12. Kroner, M., Remi, S., Hogele, A., Seidl, S., Holleitner, A. W., Warburton, R. J., Gerardot, B. D., Petroff, P. M., and Karrai, K. *Physica E* **40**, 1994–1996 (2008).
13. Dalgarno, P. A., Smith, J. M., McFarlane, J., Gerardot, B. D., Karrai, K., Badolato, A., Petroff, P. M., and Warburton, R. J. *Phys. Rev. B* **77**, 245311 (2008).
14. Leonard, D., Pond, K., and Petroff, P. M. *Phys. Rev. B* **50**, 11687–11692 (1994).
15. Warburton, R. J., Schafflein, C., Haft, D., Bickel, F., Lorke, A., Karrai, K., Garcia, J. M., Schoenfeld, W., and Petroff, P. M. *Nature* **405**, 926–929 (2000).
16. Atature, M., Dreiser, J., Badolato, A., Hogele, A., Karrai, K., and Imamoglu, A. *Science* **312**, 551–553 (2006).
17. Kroner, M., Weiss, K. M., Biedermann, B., Seidl, S., Holleitner, A. W., Badolato, A., Petroff, P. M., Öhberg, P., Warburton, R. J., and Karrai, K. *Phys. Rev. B* **78** (2008).

18. Gerardot, B. D., Brunner, D., Dalgarno, P. A., Ohberg, P., Seidl, S., Kroner, M., Karrai, K., Stoltz, N. G., Petroff, P. M., and Warburton, R. J. *Nature* **451**, 441–444 (2008).
19. Press, D., Ladd, T. D., Zhang, B., and Yamamoto, Y. *Nature* **456**, 218–221 (2008).
20. Press, D., De Greve, K., McMahon, P. L., Ladd, T. D., Friess, B., Schneider, C., Kamp, M., Hoefling, S., Forchel, A., and Yamamoto, Y. *Nature Photonics* **4**, 367–370 (2010).
21. Kuhlmann, A. V., Houel, J., Ludwig, A., Greuter, L., Reuter, D., Wieck, A. D., Poggio, M., and Warburton, R. J. *Nature Physics* **9**, 570–575 (2013).
22. Coish, W. A. and Baugh, J. *physica status solidi (b)* **246**, 2203–2215 (2009).
23. Eble, B., Testelin, C., Desfonds, P., Bernardot, F., Balocchi, A., Amand, T., Miard, A., Lemaitre, A., Marie, X., and Chamarro, M. *Phys. Rev. Lett.* **102**, 146601 (2009).
24. Khaetskii, A. V., Loss, D., and Glazman, L. *Phys. Rev. Lett.* **88**, 186802 (2002).
25. Urbaszek, B., Marie, X., Amand, T., Krebs, O., Voisin, P., Maletinsky, P., Högele, A., and Imamoglu, A. *Rev. Mod. Phys.* **85**, 79–133 (2013).
26. Xu, X., Yao, W., Sun, B., Steel, D. G., Bracker, A. S., Gammon, D., and Sham, L. J. *Nature* **459**, 1105–1109 (2009).
27. Brunner, D., Gerardot, B. D., Dalgarno, P. A., Wuest, G., Karrai, K., Stoltz, N. G., Petroff, P. M., and Warburton, R. J. *Science* **325**, 70–72 (2009).
28. Claudon, J., Bleuse, J., Malik, N. S., Bazin, M., Jaffrennou, P., Gregersen, N., Sauvan, C., Lalanne, P., and Gerard, J.-M. *Nature Photonics* **4**, 174–177 (2010).
29. Yeo, I., de Assis, P.-L., Gloppe, A., Dupont-Ferrier, E., Verlot, P., Malik, N. S., Dupuy, E., Claudon, J., Gérard, J.-M., Auffèves, A., Nogues, G., Seidelin, S., Poizat, J.-P., Arcizet, O., and Richard, M. *Nat. Nanotech.* **9**, 106–110 (2014).



## Chapter 2

# Manipulation of the nuclear spin ensemble in a quantum dot using chirped magnetic resonance pulses

### Adapted from:

Mathieu Munsch, Gunter Wüst, Andreas V. Kuhlmann, Fei Xue, Arne Ludwig, Dirk Reuter, Andreas D. Wieck, Martino Poggio and Richard J. Warburton, **“Manipulation of the nuclear spin ensemble in a quantum dot with chirped magnetic resonance pulses”**, *Nature Nanotechnology* **9**, 671-675 (2014).

The nuclear spins in nano-structured semiconductors play a central role in quantum applications<sup>1-4</sup>. The nuclear spins represent a useful resource for generating local magnetic fields<sup>5</sup> but nuclear spin noise represents a major source of dephasing for spin qubits<sup>2,3</sup>. Controlling the nuclear spins enhances the resource while suppressing the noise. Nuclear magnetic resonance (NMR) techniques are challenging: the group-III and group-V isotopes have large spins with widely different gyromagnetic-ratios; in strained material there are large atom-dependent quadrupole-shifts<sup>6</sup>; nano-scale NMR is hard to detect<sup>7,8</sup>. We report NMR on 100,000 nuclear spins of a quantum dot using chirped radio-frequency pulses. Following polarization, we demonstrate a reversal of the nuclear spin. We can flip the nuclear spin back-and-forth a hundred times. We demonstrate that chirped-NMR is a powerful way of determining the chemical composition, the initial nuclear spin temperatures and quadrupole frequency distributions for all the main isotopes. The key observation is a plateau in the NMR signal as a function of sweep-rate: we achieve inversion at the first quantum transition for all isotopes simultaneously. These experiments represent a generic technique for manipulating nano-scale inhomogeneous nuclear spin ensembles and open the way to probe the coherence of such mesoscopic systems.

(Experiments and results presented in this chapter were obtained in close collaboration with Mathieu Munsch.)

## 2.1 Introduction

NMR signals can be boosted by polarizing the nuclei. This is particularly beneficial on the nano-scale where NMR signals are invariably small and hard to detect. The nuclear spins in a self-assembled quantum dot can be polarized optically by exploiting the hyperfine interaction with an electron spin<sup>3,5</sup>. Extremely long-lived polarizations<sup>4,9,10</sup> (appendix A.2) up to about 50% have been achieved. The nuclear spin polarization results in a shift of the optical resonance, the Overhauser shift, facilitating its sensitive detection<sup>5</sup>. These features have enabled the observation of isotope-selective NMR of the nuclear spins associated with strain-free GaAs quantum dots<sup>11,12</sup>. Self-assembled quantum dots, attractive for single photon generation and optically-controlled spin qubits<sup>2</sup>, have highly inhomogeneous nuclear spins<sup>5,13–15</sup>. Additional side peaks appear in the NMR spectra, a consequence of a strain-dependent quadrupole interaction, along with a distribution of chemical shifts<sup>6</sup>. Manipulating the nuclear spin ensemble of a single quantum dot is challenging yet important: projection of the nuclear spins into a specific state boosts the single electron spin dephasing time<sup>4</sup>; developing techniques to probe nano-sized ensembles of highly inhomogeneous nuclear spins has impact also for semiconductor nanowires<sup>16</sup> and nanocrystals.

## 2.2 Concepts and experimental realization

### 2.2.1 Adiabatic passage: The Landau-Zener-Problem

Here we use chirped NMR pulses. The main concept is that by sweeping over a large frequency range, the pulse addresses each nuclear spin at some point. For a spin- $\frac{1}{2}$  nucleus, a 2-level system, the Hamiltonian in the rotating frame is,

$$H = h\Delta\nu(t)I_z + \frac{1}{2}h\gamma B_x I_x \quad (2.1)$$

where  $h$  is the Planck constant,  $I$  the nuclear spin,  $\gamma$  the gyromagnetic ratio of the nuclear isotope (in frequency units) and  $\Delta\nu(t)$  is the time-dependent detuning between the radio frequency (RF) excitation and the Larmor frequency  $\nu_L = \gamma B_z$ . The coupling between the RF magnetic field  $B_x$  and the spin, the second term in the Hamiltonian, leads to an avoided crossing in the eigen-energies with splitting  $h\nu_{RF}$  (Fig. 1(a)), where

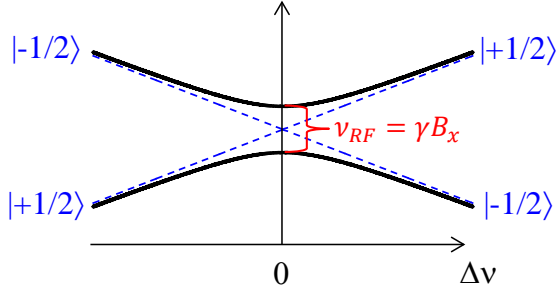


Fig. 2.1. **Eigen-energies of the nuclear spin  $I = \frac{1}{2}$  in the rotating frame versus RF detuning:** The static magnetic field is oriented along  $z$  and the oscillating (radio-frequency, RF) magnetic field along  $x$ . Dashed blue lines show the diabetic states. The size of the avoided crossing  $\nu_{RF}$  is proportional to the strength of the RF field  $B_x$ .

$\nu_{RF} = \gamma B_x$ . On traversing the avoided crossing from large and negative  $\Delta\nu$  to large and positive  $\Delta\nu$  with a single pulse ( $N = 1$ ) at sweep rate  $\alpha$ , the probability that the final state is  $|\uparrow\rangle$  for initial state  $|\uparrow\rangle$ , is

$$P_{LZ} = \exp(-\pi^2 \nu_{RF}^2 / \alpha), \quad (2.2)$$

the Landau-Zener result<sup>17</sup>. In the sudden regime when  $P_{LZ} \simeq 1$ , the system “tunnels” through the avoided crossing and  $|\uparrow\rangle \rightarrow |\uparrow\rangle$ ,  $|\downarrow\rangle \rightarrow |\downarrow\rangle$ . Alternatively, in the limit when  $P_{LZ} \ll 1$ , the states are swapped  $|\uparrow\rangle \rightarrow |\downarrow\rangle$ ,  $|\downarrow\rangle \rightarrow |\uparrow\rangle$ : this is adiabatic passage (Fig. 2.1).

## 2.2.2 Experimental setup

We attempt to apply these concepts to a single nano-scale nuclear spin ensemble. The challenges are, first, each nuclear spin is more complex than a two-level system; and second, there is an inhomogeneous distribution of  $10^5$  nuclear spins. Initialization and detection of the nuclear spin polarization of a single quantum dot is carried out optically with exquisite spectral resolution provided by resonant laser spectroscopy, representing a sensitivity to  $\sim 1,000$  spins. The quantum dots for these experiments are gate-controlled  $\text{In}_x\text{Ga}_{1-x}\text{As}$  quantum dots (appendix A.1), (Fig. 2.2(a)). The bias voltage  $V_g$  controls both the occupation of the quantum dot (here empty) and the exact optical transition frequency via the Stark effect. Key to reaching the adiabatic limit  $P_{LZ} \ll 1$  is the generation of RF fields with high amplitude. We use an on-chip, low-impedance, high bandwidth microwire<sup>18</sup> (appendix A.1), fabricated directly above the gate: large oscillating currents in the microwire generate oscillating magnetic fields ( $B_x \simeq 5$  mT,

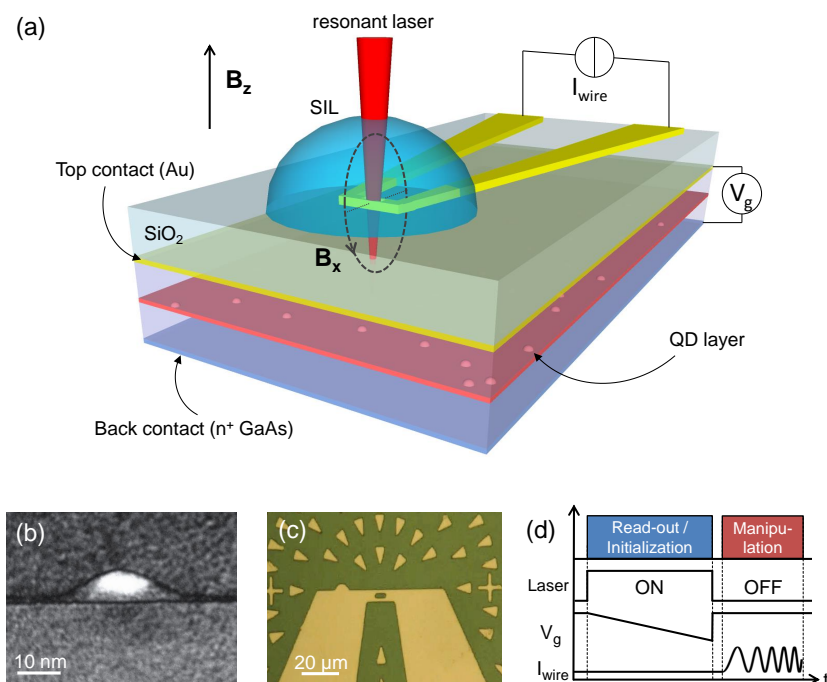


Fig. 2.2. **Experimental setup.** (a) Sample for magnetic resonance experiments on the nuclear spins of a single self-assembled quantum dots. The quantum dots are embedded in a vertical tunnelling structure controlled by gate voltage  $V_g$ . A gold microwire is fabricated above the gate with a hole for optical access. Magnetic resonance is driven with an RF current passing through the microwire. A solid-immersion-lens enhances the collection efficiency of the resonance fluorescence. (b) Cross-section of a single InGaAs quantum dot (TEM image courtesy of Arne Ludwig and Jean-Michel Chauveau). (c) Top view of microwire. (d) Pulse sequence of NMR experiment. A resonance is established with a constant frequency laser. On ramping the gate voltage, the nuclear spins polarize in order to maintain the optical resonance: the Stark effect is compensated by the Overhauser shift. A RF pulse is then applied to manipulate the nuclear spin ensemble. The optical sequence is repeated to read-out the nuclear spin polarization, acting also as initialization for the next sequence.

appendix A.1); the small impedance of the microwire enables fast pulsing. An aperture in the microwire allows optical access to the quantum dots directly underneath (Fig. 2.2(a),(c)). The quantum dot optical resonance ( $X^0$ ) is driven with a coherent laser with resonance fluorescence detection<sup>19,20</sup>, the read-out after one RF pulse providing the initialization for the next (Fig. 2.2(d)).

## 2.3 Reading and setting the nuclear spin polarization using the dragging effect

A resonance fluorescence spectrum of the quantum dot at zero applied magnetic field,  $B_z = 0$  T, is shown in Fig. 2.3(a): the two lines, split by the fine-structure, have linewidths of 1.2  $\mu\text{eV}$ , close to the transform limit of 0.9  $\mu\text{eV}$ <sup>21</sup>. At  $B_z \geq 0.5$  T, on sweeping through the optical resonance, the nuclear spins adjust their polarization to maintain an optical resonance of the quantum dot with the laser, the “dragging” effect<sup>22,23</sup>: the Overhauser shift OHS equals the laser detuning  $\delta_L$ . Dragging represents a way of generating large bi-directional nuclear spin polarizations<sup>22</sup>. An example is shown in Fig. 2.3(b): starting with the nuclei in a depolarized state (appendix A.2), the optical resonance is “dragged” to  $\delta_L = -41$   $\mu\text{eV}$ . The nuclear spin polarization decays extremely slowly (timescale days for an empty quantum dot<sup>4,9,10</sup>) (appendix A.2), resulting in optical memory effects. A sequence of optical sweeps is shown in Fig. 2.3(b): the rise point of each scan is related to the polarization set by the previous scan whereas the end of the plateau sets the new polarization state.

## 2.4 Manipulation of the nuclear spin ensemble

For a given laser sweep direction, the change in width of the dragging “plateau” following an NMR pulse is used to measure the change in the Overhauser field,  $\Delta_{\text{OHS}}$  in Fig. 2.4(a). Manipulation of the nuclear spin ensemble is demonstrated in Fig. 2.4(a). The nuclear spin polarization along  $z$ ,  $\langle I_z \rangle$ , is initialized with a sweep from positive to negative  $\delta_L$ . With the laser off, a chirped NMR pulse is applied,  $\nu = \nu_1 \rightarrow \nu_2$ . The laser is then turned back on and the sweep from positive to negative  $\delta_L$  repeated. The optical signal now appears not at negative  $\delta_L$  but at positive  $\delta_L$ , unambiguous evidence that the RF pulse inverts the nuclear spin polarization. In this particular case, following optical polarization,  $\langle I_z \rangle / I_z^{\text{max}} \simeq +32\%$ , and after one NMR pulse,  $\langle I_z \rangle / I_z^{\text{max}} \simeq -13\%$  (appendix A.3). This interpretation is backed up by applying not one but a sequence of chirped pulses,  $\nu_1 \rightarrow \nu_2 \rightarrow \nu_1 \rightarrow \nu_2 \dots$ . As a function of pulse number  $N$ ,  $\langle I_z \rangle$  oscillates from positive to negative, evidence of close-to-adiabatic manipulation of  $\langle I_z \rangle$ . We can invert-restore the nuclear spin polarization  $\sim 100$  times before the signal is lost (Fig. 2.4(b)).



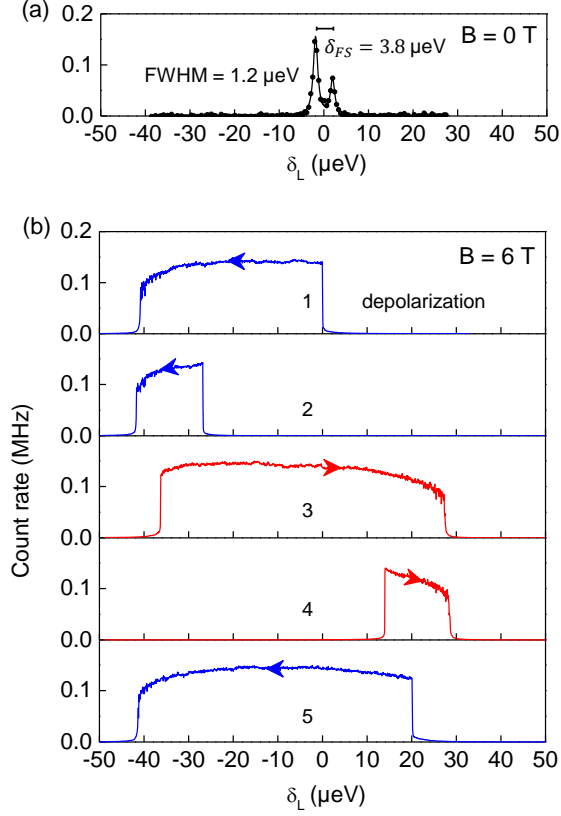


Fig. 2.3. **Resonance fluorescence versus laser detuning from a single quantum dot ( $X^0$  transition).** (a) At  $B_z = 0$ , where  $\delta_{FS}$  is the fine structure splitting. (b) Resonance fluorescence versus laser detuning at  $B_z = 6 \text{ T}$  on the blue  $X^0$  transition showing “dragging”. The plateau-like features signify nuclear spin polarization. A sequence of sweeps shows clear memory effects. The extent of the plateaux are reproducible to within  $0.6 \mu\text{eV}$  on repeating a specific cycle. In blue (red) the laser is tuned to more negative (positive) values.

## 2.5 Chemical composition and nuclear spin temperature

We explore the dependence on sweep rate  $\alpha$  on tuning from low  $\nu_1$  to high  $\nu_2$  such that all nuclear spins are addressed. The signal increases with decreasing sweep rate (Fig. 2.6). Significantly, there is an exponential increase followed by a plateau and then another exponential increase. The step-wise transition from the sudden to the adiabatic regime is a consequence of a hierarchy of avoided crossings in the energy level structure. It arises from a quadrupole interaction of the nuclear spin with a local electric field

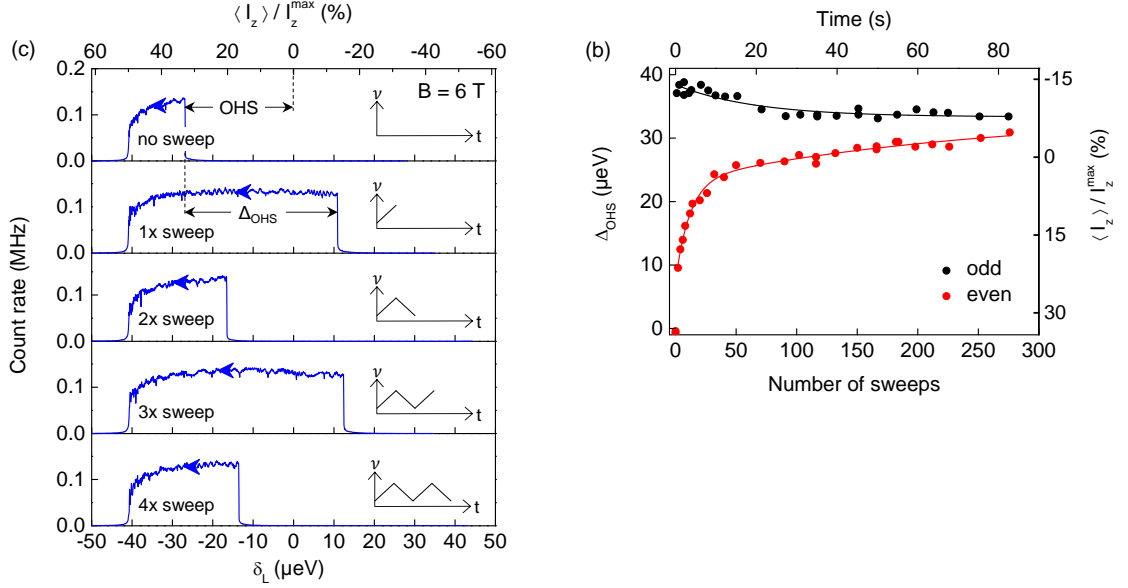


Fig. 2.4. **Adiabatic passage of the nuclear spin ensemble.** (a) A sequence of resonance fluorescence sweeps with  $N$  chirped RF pulses ( $\nu_1 = 32.5 \text{ MHz}$ ,  $\nu_2 = 87.5 \text{ MHz}$ ,  $\alpha = 0.18 \text{ GHz/s}$ ) following nuclear spin polarization ( $N = 0, 1, 2, 3, 4$ ).  $N = 0$  reads initial  $\langle I_z \rangle$  (appendix A);  $N = 1$  inverts  $\langle I_z \rangle$ ;  $N = 2$  restores  $\langle I_z \rangle$  to almost its  $N = 0$  value, etc. The Overhauser shift (OHS) and the change in Overhauser shift  $\Delta_{\text{OHS}}$  following a chirped pulse are labelled. (b)  $\Delta_{\text{OHS}}$  versus  $N$  for large  $N$ . The decay at large  $N$  arises mostly from relaxation processes during the sweep; the residual signal at large  $N$  is presently not understood. Solid lines are guides for the eye.

gradient resulting in an additional term in the Hamiltonian,

$$H_Q = \frac{1}{6} h \nu_Q [3I_z^2 - I(I+1)]. \quad (2.3)$$

where  $h\nu_Q$  is the strength of the quadrupole field (appendix A.3). Fig. 2.5 shows the eigen-energies for  $I = \frac{3}{2}$ , both in the laboratory and in the rotating frame.

When  $\nu_Q \gg \nu_{RF}$ , a hierarchy of avoided crossings appears, large for the first quantum transitions (bare states separated by  $|\Delta m| = 1$ ); intermediate at the second quantum transitions ( $|\Delta m| = 2$ ); and small at the third quantum transition ( $|\Delta m| = 3$ ). A similar but more complex hierarchy also arises in the In ( $I = \frac{9}{2}$ ) eigen-energies. Given the exponential dependence of  $P_{LZ}$  on the energy separation at the avoided crossing, this means that the different quantum transitions satisfy the adiabaticity condition at quite different sweep rates<sup>24–26</sup>. At the plateau in Fig. 2.6, the sweep is adiabatic for the first quantum transitions ( $P_{LZ} \ll 1$ ) whereas the others are still in the sudden regime ( $P_{LZ} \simeq 1$ ). At first sight, it is surprising that the step signifying adiabaticity at the first

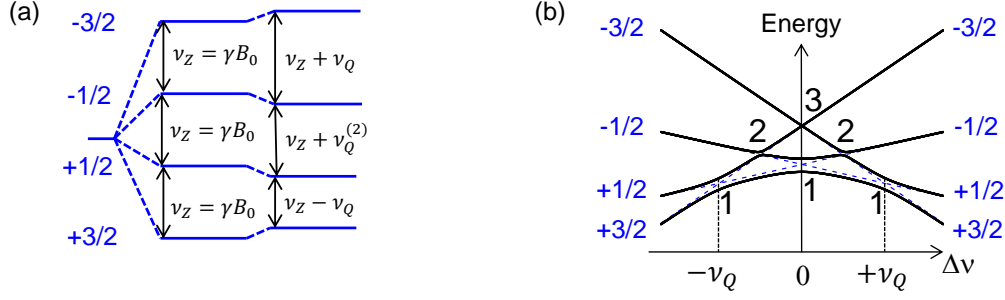


Fig. 2.5. **Energy levels for a spin  $I = \frac{3}{2}$ .** (a) In the laboratory frame. The static field  $B_z$  causes the spin states to split into the Zeeman ladder, equally spaced by the Larmor frequency  $\nu_L$ . The nuclear quadrupolar moments couple to the electric field gradient resulting in alterations to the level spacing. The central transition is only affected by second order terms. (b) In the rotating frame energy versus RF detuning in the limit of  $\nu_Q \ll \nu_{RF}$ . There is a hierarchy of avoided crossings, the first, second and third quantum transitions ( $|\Delta m| = 1$ ,  $|\Delta m| = 2$  and  $|\Delta m| = 3$ , respectively) (appendix A.3).

quantum transitions survives the ensemble averaging. The explanation is to be found in the scaling of the energies at the avoided crossings,  $h\nu_{\text{eff}}$ . In the limit  $\nu_Q \gg \nu_{RF}$ ,  $\nu_{\text{eff}} \propto \nu_{RF}(\nu_{RF}/\nu_Q)^{|\Delta m|-1}$  for all  $I$ <sup>24-26</sup> (appendix A.3). This means that for  $|\Delta m| = 1$ ,  $\nu_{\text{eff}}$  does *not* depend on  $\nu_Q$  (to first order), suppressing the sensitivity of the adiabaticity criterion to the quadrupole interaction.

The plateau in the sweep rate dependence is the key observation that allows both the indium concentration  $x$  and the initial nuclear spin temperature  $T$  to be determined. The point is that the signal at the plateau,  $\Delta_{\text{OHS}} = 28.8 \mu\text{eV}$ , and the initial Overhauser shift,  $\text{OHS} = 27.0 \mu\text{eV}$ , are determined solely by  $x$ ,  $T$  and the known nuclear parameters (nuclear spins, hyperfine coupling constants and abundances of  $^{75}\text{As}$ ,  $^{115}\text{In}$ ,  $^{69}\text{Ga}$  and  $^{71}\text{Ga}$ ), see appendix A.3. We find  $x = (20.2 \pm 5.7)\%$  and  $T = (8.2 \pm 0.8) \text{ mK}$ . The composition  $x$  represents the indium concentration over the extent of the electron wave function; the temperature, much lower than the bath temperature of 4.2 K, interprets the dynamic nuclear spin polarization as a laser cooling phenomenon.

## 2.6 Spectroscopic measurements and quadrupole frequency distributions

Spectroscopic identification of the isotopes is presented in Fig. 2.7 where the NMR pulse is chirped from a fixed  $\nu_1$  to a variable  $\nu_2$  using a slow and constant sweep rate. The NMR signal  $\Delta_{\text{OHS}}$  increases step-wise around 44 MHz. This arises when  $\nu_2$  goes above

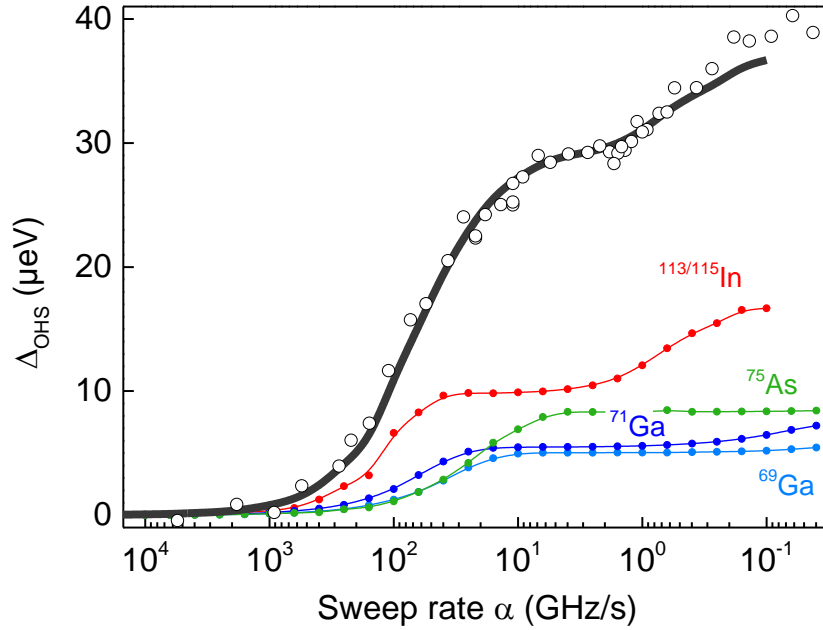


Fig. 2.6. **Nuclear spin inversion at the first quantum transition in chirped NMR.** NMR signal,  $\Delta_{\text{OHS}}$ , following a single chirped RF pulse with  $\nu_1 \rightarrow \nu_2$  ( $\nu_1 = 32.5$  MHz,  $\nu_2 = 87.5$  MHz) as a function of sweep rate  $\alpha$ : experimental data (open circles) along with theory (dark gray line). The theory uses  $x = 20.2\%$ ,  $T = 8.2$  mK,  $B_x = 3.8$  mT,  $\langle \nu_Q[^{75}\text{As}] \rangle = 3.0$  MHz,  $\langle \nu_Q[^{115}\text{In}] \rangle = 1.5$  MHz,  $\langle \nu_Q[^{69}\text{Ga}] \rangle = 3.1$  MHz,  $\langle \nu_Q[^{71}\text{Ga}] \rangle = 2.1$  MHz. The relative abundances are  $^{75}\text{As}$  (100%),  $^{113}\text{In}$  (4.3%),  $^{115}\text{In}$  (95.7%);  $^{69}\text{Ga}$  (60.1%)  $^{71}\text{Ga}$  (39.9%).  $\Delta_{\text{OHS}}$  versus  $\alpha$  is shown for the four isotopes separately (colour plots). The plateau arises because a range of  $\alpha$  exists in which inversion at the first quantum transition is achieved for all isotopes yet inversion at the second quantum transition is achieved for none. At the smallest  $\alpha$ , inversion at the first and second quantum transitions is achieved for the majority of In nuclei but only inversion at the first quantum transition for the majority of  $I = \frac{3}{2}$  nuclei.

the central NMR frequency of a particular isotope, in this case  $^{75}\text{As}$ . Another clear step arises at 79 MHz, the  $^{71}\text{Ga}$  resonance. Around the central transition, the single spin satellite steps (appendix A.3) are broadened through atom-dependent quadrupole couplings. This is particularly visible in the In contribution because of the large number of satellites. This curve enables us to determine the average quadrupole frequency  $\langle \nu_Q \rangle$  and an approximate distribution  $p(\nu_Q)$  for *all* the main isotopes,  $^{75}\text{As}$ ,  $^{115}\text{In}$ ,  $^{69}\text{Ga}$  and  $^{71}\text{Ga}$ .

For a specific  $I$ ,  $\nu_Q$  and  $\nu_{RF}$ , we occupy the initial nuclear states according to the known  $T$ , and integrate the Schrödinger equation numerically to determine  $\langle I_z \rangle$  after a single NMR pulse, converting  $\langle I_z \rangle$  to  $\Delta_{\text{OHS}}$  with the appropriate hyperfine coefficient. We find that the  $\nu_2$ -dependence is a strong function of both  $\langle \nu_Q \rangle$  and  $p(\nu_Q)$  (appendix

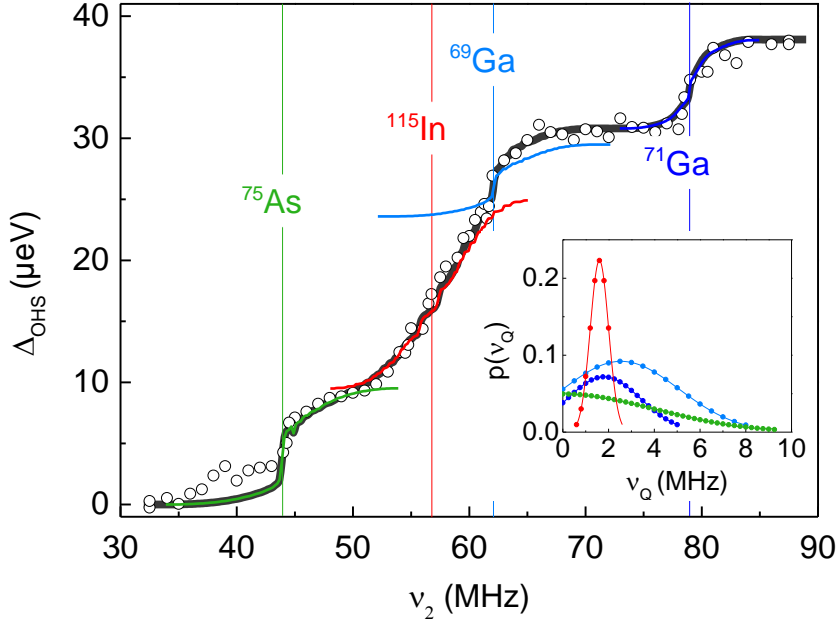


Fig. 2.7. **Isotope-sensitive NMR with chirped pulses.** NMR signal  $\Delta_{\text{OHS}}$  following a single chirped RF pulse,  $\nu_1 \rightarrow \nu_2$  as a function of  $\nu_2$ : experimental data (open circles) along with theory (dark gray line). The sweep rate  $\alpha = 0.09$  GHz/s and  $\nu_1 = 32.5$  MHz. The vertical lines show the text-book NMR frequencies of the In ( $I = \frac{9}{2}$ ), Ga ( $I = \frac{3}{2}$ ) and As ( $I = \frac{3}{2}$ ) isotopes: step-wise increases in signal occur each time  $\nu_2$  crosses these particular frequencies. The theory uses  $x = 20.2\%$ ,  $T = 8.2$  mK and  $B_x = 3.8$  mT as in Fig. 3, along with Gaussian distributions for the quadrupole frequencies (inset).

A.3) and is therefore ideal to determine them. The  $^{75}\text{As}$  and  $^{71}\text{Ga}$  are well isolated as a function of  $\nu_2$  and in both cases,  $\langle \nu_Q \rangle$  and  $p(\nu_Q)$  are readily determined by comparing the experimental results to the theory. The  $^{69}\text{Ga}$   $\nu_2$ -dependence can be predicted from the  $^{71}\text{Ga}$   $\nu_2$ -dependence simply by the known abundances and quadrupole moments (appendix A.3). The remaining signal at intermediate  $\nu_2$  arises mostly from  $^{115}\text{In}$  allowing us to determine the  $^{115}\text{In}$  quadrupole parameters. Fig. 2.7 shows that, first, we achieve an excellent description of the experimental results; and second, the signals from the four isotopes  $^{75}\text{As}$ ,  $^{115}\text{In}$ ,  $^{69}\text{Ga}$  and  $^{71}\text{Ga}$  overlap little facilitating the determination of each quadrupole distribution.

We return to the sweep rate dependence. We calculate the  $\alpha$ -dependence, adding the results from each isotope with  $x$ ,  $T$ ,  $\langle \nu_Q \rangle$  as input parameters. ( $B_x$  is adjusted within its error window to ensure that the plateau occurs at the correct  $\alpha$ .) The *same* set of parameters describes *both* the  $\nu_2$ - and  $\alpha$ -dependences. Fig. 2.6 shows the contribution from each isotope.  $^{115}\text{In}$  has the largest  $h\nu_{\text{eff}}$  (on account of its large spin,  $I = \frac{9}{2}$ )

and inversion at the first quantum transition is achieved first of all, closely followed by inversion at the first quantum transition for the  $I = \frac{3}{2}$  nuclei. At the smallest  $\alpha$ , inversion at the second quantum transition is achieved for most of the In nuclei (and some of the  $^{71}\text{Ga}$  nuclei) but for most of the  $^{75}\text{As}$  and  $^{69}\text{Ga}$  nuclei, inversion at the first quantum transition is complete but inversion at the second quantum transition is not yet achieved. This explains the second change in gradient at the smallest  $\alpha$  in the experiment. The combination of the  $\nu_2$  and the  $\alpha$ -dependences allows in principle an initial nuclear spin temperature to be determined for each isotope. In practice, these temperatures are not significantly different to within the random error (appendix A.3) and we take a common temperature for simplicity.

## 2.7 Conclusions

The overall conclusion is that frequency-swept NMR enables the determination of all key parameters of the nuclear spins even at the single quantum dot level: the chemical composition, the effective temperatures and the quadrupole frequency distribution of each isotope. In chapter 3 we demonstrate that a sweep adiabatic for  $|\Delta m = 1|$  but sudden for  $|\Delta m = 2|$  can be used to produce highly non-thermal distributions of the spin states, boosting the NMR signal of the central transitions. This is the prerequisite for the following nuclear spin coherence measurements (chapter 2). As an outlook we note that at an intermediate sweep rate, a superposition of the spin states is created with a chirped NMR pulse, and back-and-forth frequency sweeps result in quantum interferences, the Stückelberg oscillations<sup>17,27-30</sup>. This experiment represents the ideal springboard to explore quantum coherence in a complex nuclear spin ensemble using multiple chirped pulses.

## References

1. Ribeiro, H. and Burkard, G. *Nature Materials* **12**, 469 – 471 (2013).
2. Warburton, R. J. *Nature Materials* **12**, 483 – 493 (2013).
3. Chekhovich, E. A., Makhonin, M. N., Tartakovskii, A. I., Yacoby, A., Bluhm, H., Nowack, K. C., and Vandersypen, L. M. K. *Nature Materials* **12**, 494–504 (2013).
4. Greilich, A., Shabaev, A., Yakovlev, D. R., Efros, A. L., Yugova, I. A., Reuter, D., Wieck, A. D., and Bayer, M. *Science* **317**, 1896–1899 (2007).
5. Urbaszek, B., Marie, X., Amand, T., Krebs, O., Voisin, P., Maletinsky, P., Högele, A., and Imamoglu, A. *Rev. Mod. Phys.* **85**, 79–133 (2013).
6. Chekhovich, E., Kavokin, K., Puebla, J., Krysa, A., Hopkinson, M., Andreev, A., Sanchez, A., Beanland, R., Skolnick, M., and Tartakovskii, A. *Nature Nanotechnology* **7**, 646–650 (2012).
7. Staudacher, T., Shi, F., Pezzagna, S., Meijer, J., Du, J., Meriles, C. A., Reinhard, F., and Wrachtrup, J. *Science* **339**, 561–563 (2013).
8. Mamin, H. J., Kim, M., Sherwood, M. H., Rettner, C. T., Ohno, K., Awschalom, D. D., and Rugar, D. *Science* **339**, 557–560 (2013).
9. Maletinsky, P., Kroner, M., and Imamoglu, A. *Nature Physics* **5**, 407–411 (2009).
10. Latta, C., Srivastava, A., and Imamoglu, A. *Phys. Rev. Lett.* **107**, 167401 (2011).
11. Gammon, D., Brown, S. W., Snow, E., Kennedy, T., Katzer, D., and Park, D. *Science* **277**, 85–88 (1997).
12. Makhonin, M., Kavokin, K., Senellart, P., Lemaître, A., Ramsay, A., Skolnick, M., and Tartakovskii, A. *Nature Materials* **10**, 844–848 (2011).
13. Flisinski, K., Gerlovin, I. Y., Ignatiev, I. V., Petrov, M. Y., Verbin, S. Y., Yakovlev, D. R., Reuter, D., Wieck, A. D., and Bayer, M. *Phys. Rev. B* **82**, 081308 (2010).
14. Cherbunin, R. V., Flisinski, K., Gerlovin, I. Y., Ignatiev, I. V., Kuznetsova, M. S., Petrov, M. Y., Yakovlev, D. R., Reuter, D., Wieck, A. D., and Bayer, M. *Phys. Rev. B* **84**, 041304 (2011).
15. Bulutay, C. *Phys. Rev. B* **85**, 115313 (2012).

16. Peddibhotla, P., Xue, F., Hauge, H. I. T., Assali, S., Bakkers, E. P. a. M., and Poggio, M. *Nature Physics* **9**, 631 (2013).
17. Shevchenko, S., Ashhab, S., and Nori, F. *Physics Reports* **492**, 1–30 (2010).
18. Poggio, M., Degen, C. L., Rettner, C., Mamin, H., and Rugar, D. *Applied Physics Letters* **90**, 263111 (2007).
19. Kuhlmann, A. V., Houel, J., Ludwig, A., Greuter, L., Reuter, D., Wieck, A. D., Poggio, M., and Warburton, R. J. *Nature Physics* **9**, 570–575 (2013).
20. Kuhlmann, A. V., Houel, J., Brunner, D., Ludwig, A., Reuter, D., Wieck, A. D., and Warburton, R. J. *Review of Scientific Instruments* **84**, 073905 (2013).
21. Kuhlmann, A. V., Pechtel, J. H., Houel, J., Ludwig, A., Reuter, D., Wieck, A. D., and Warburton, R. J. *arXiv:1307.7109* (2013).
22. Latta, C., Hoegele, A., Zhao, Y., Vamivakas, A. N., Maletinsky, P., Kroner, M., Dreiser, J., Carusotto, I., Badolato, A., Schuh, D., Wegscheider, W., Atatüre, M., and Imamoglu, A. *Nature Physics* **5**, 758–763 (2009).
23. Högele, A., Kroner, M., Latta, C., Claassen, M., Carusotto, I., Bulutay, C., and Imamoglu, A. *Phys. Rev. Lett.* **108**, 197403 (2012).
24. Vega, S. *The Journal of Chemical Physics* **68**(12), 5518–5527 (1978).
25. Haase, J., Conradi, M., Grey, C., and Vega, A. *Journal of Magnetic Resonance, Series A* **109**, 90–97 (1994).
26. van Veenendaal, E., Meier, B. H., and Kentgens, A. P. M. *Molecular Physics* **93**, 195–213 (1998).
27. Stüchelberg, E. *Helv. Phys. Acta.* **5**, 369 (1932).
28. Yoakum, S., Sirko, L., and Koch, P. M. *Phys. Rev. Lett.* **69**, 1919–1922 (1992).
29. Oliver, W. D., Yu, Y., Lee, J. C., Berggren, K. K., Levitov, L. S., and Orlando, T. P. *Science* **310**, 1653–1657 (2005).
30. Huang, P., Zhou, J., Fang, F., Kong, X., Xu, X., Ju, C., and Du, J. *Phys. Rev. X* **1**, 011003 (2011).



## Chapter 3

# Nuclear spin coherence in a quantum dot

Self-assembled semiconductor quantum dots (QD) are excellent single photon sources<sup>1</sup> and possible hosts for electron spin qubits<sup>2</sup>, which can be initialized, manipulated and read-out optically<sup>3</sup>. For most solid state electron spin qubits in GaAs one unmastered source of decoherence is the hyperfine interaction with the nuclear spins, whose coherence is inevitably limited by nuclear dipole-dipole interactions. Recent work<sup>4,5</sup> on uncharged QDs showed that in strained nano-structures quadrupolar effects suppress dipole-dipole interactions and prolong nuclear spin coherence times up to a few ms. It has been argued this would also lead to enhanced electron spin coherence times. However, the effect of actually loading the QD with an electron on nuclear spin coherence has so far only been investigated theoretically<sup>6</sup>. Here we measure the nuclear spin ensemble coherence for a single InGaAs quantum dot embedded in a charge tunable device<sup>7</sup>. For an empty dot we confirm Hahn echo coherence times  $T_2$  of a few ms. In contrast, on charging with a single electron  $T_2$  drops by more than a factor 100 down to a few tens of  $\mu\text{s}$ . The reduction of coherence is explained by electron mediated coupling between nuclear spins due to the hyperfine interaction<sup>6</sup>, an example of RKKY-type interaction. Charging the QD with two electrons (a singlet state) recovers the  $T_2$  times of the empty dot, ruling out any systematic errors resulting from the switching process itself.

### 3.1 Introduction

The proposal to use the spin of an electron bound to a quantum dot as a the basis for quantum information processing<sup>2</sup> has stimulated great research effort<sup>8</sup>. However, a central crux for quantum dot based electron qubits is dephasing due to the interaction with the  $\sim 10^4 - 10^5$  nuclear spins of the host material. Hence understanding, and if possible controlling the underlying mechanisms is essential. The hyperfine coupling between the electron spin and nuclear spins is described by the Fermi contact interaction. Typically the static effect of the nuclear spins acting on the electron spin is described by the Overhauser field  $B_N$ . For optically active quantum dots,  $B_N$  and hence the nuclear spin polarization can read-out by measuring changes in the excitonic resonance position. The static effect of the electron spin on the nuclear spins is described by the Knight field. Furthermore, a flip-flop term in the Hamiltonian enables spin transfer between the nuclei and the electron, enabling dynamic nuclear spin polarization (DNSP) by optical means.

Dipolar coupling between the nuclear spins results in statistical fluctuations of  $B_N$  with a standard deviation  $\sigma_N = B_N^{max}/\sqrt{N}$  around 10 mT<sup>9,10</sup> for  $N \sim 10^5$ . Here  $B_N^{max}$  is the maximum Overhauser field and  $N$  the number of nuclei. Narrowing  $\sigma_N$  by suppressing dipolar coupling is supposed to be beneficial for the electron spin coherence. In the case of high external magnetic fields the dipole-dipole interactions between two nuclear spins  $I$  and  $J$  has the following form<sup>11</sup>:

$$H_{dd} = \nu_{dd}(I_z J_z - \frac{1}{2}(I_x J_x + I_y J_y)), \quad (3.1)$$

where the coupling strength  $\nu_{dd} \leq 200$  Hz for nearest neighbours in InGaAs<sup>4</sup> and scales as  $r^{-3}$  with the nuclear distance  $r$ . For strained QDs atom-dependent quadrupolar shifts<sup>12</sup> (chapter 2) lead to modifications of the Zeeman energy ladder (Fig. 2.5). These shifts are quantified by the quadrupole frequency  $\nu_Q$ , typically a few MHz (chapter 2). However, the central transition (CT) ( $+1/2 \leftrightarrow -1/2$ ) is only affected by second order quadrupolar effects  $\nu_Q^{(2)}$ , resulting in a broadening of the CT with a width of just a few 10-100 kHz<sup>4</sup>. Since  $\nu_Q, \nu_Q^{(2)} \gg \nu_{dd}$  flip-flop processes described by the second term of equation 3.1 are energetically forbidden. Thus nuclear spin diffusion out of the dot is strongly suppressed resulting in  $T_1$  times for the ensemble polarization in the order of days (appendix A.2) and spin bath coherence times  $T_2$  increased by a factor of  $\sim 5$  compared to values measured in unstrained structures<sup>4</sup>.

In this chapter we investigate the effect of charging the QD on nuclear spin coherence

for indium and arsenic isotopes. To do so, we combine chirped and pulsed NMR techniques with minimally invasive resonance fluorescence on a single QD embedded in a charge tunable structure. For an empty and a doubly charged QD we confirm coherence times of a few ms, as expected for suppressed nuclear dipolar interaction. In stark contrast the nuclear spin coherence is strongly reduced (by more than a factor 100) when the QD is charged with a single electron. We attribute this observation to an RKKY interaction, a second order process where nuclear spins are coupled to each other via hyperfine interaction with the conduction electron. Adapting the theory for electron mediated nuclear spin coupling in QDs developed by Klauser *et al*<sup>6</sup> we can explain the decrease in nuclear spin coherence.

## 3.2 Concept and experimental cycle

The hardware of the experimental setup is the same as in chapter 2 (appendix A.1). A measurement cycle is shown in Fig. 3.1(a). Again, we start with a dragging process<sup>13</sup>, reading the previous nuclear spin polarization and setting the initial thermal nuclear spin distribution (appendix A.3) for the next cycle. In order to obtain a detectable signal we maximize the population difference between the  $+1/2$  and the  $-1/2$  state with a preparation pulse. This is best understood by looking at the energy levels of a spin  $3/2$  in the rotating frame (Fig. 3.1(b)). In the limit of  $\nu_Q \gg \nu_{RF}$  the three first order transitions are well separated in frequency. Furthermore, one can transverse the first order transitions fully adiabatically, while still being in the fully sudden regime for the higher order transitions (chapter 2). A chirped RF pulse starting from a large negative (positive) detuning through the transition at  $-\nu_Q$  ( $+\nu_Q$ ) and stopping before coming close to the central transition swaps the population between  $+3/2$  and  $+1/2$  ( $-3/2$  and  $-1/2$ ). The sweep rate  $\alpha = 10$  GHz/s was chosen so that first (second) order quantum transitions are traversed fully adiabatic (sudden). Next, we select the QD charge state by setting the gate voltage  $V_g$  and apply a coherent pulse (Rabi or Hahn-echo sequence) on resonance with the central transition.

To minimize depolarization effects due to changing  $V_g$ , we keep the charging time fixed and short ( $\leq 50$  ms) compared to depolarization resulting from electron spin exchange with the back contact. Even for  $V_g$  in between the empty and singly charged state, the cotunneling regime, were the electron spin flip rate due to coupling with the back contact is fastest,  $T_1$  processes can be neglected for times shorter than 50 ms (Fig. 3.2). Furthermore, we determine the switching time of the device for charging the QD to be  $\sim 10$   $\mu$ s (appendix B) and hence introduce a 100  $\mu$ s delay between setting  $V_g$  and

applying the coherent RF pulse sequence.

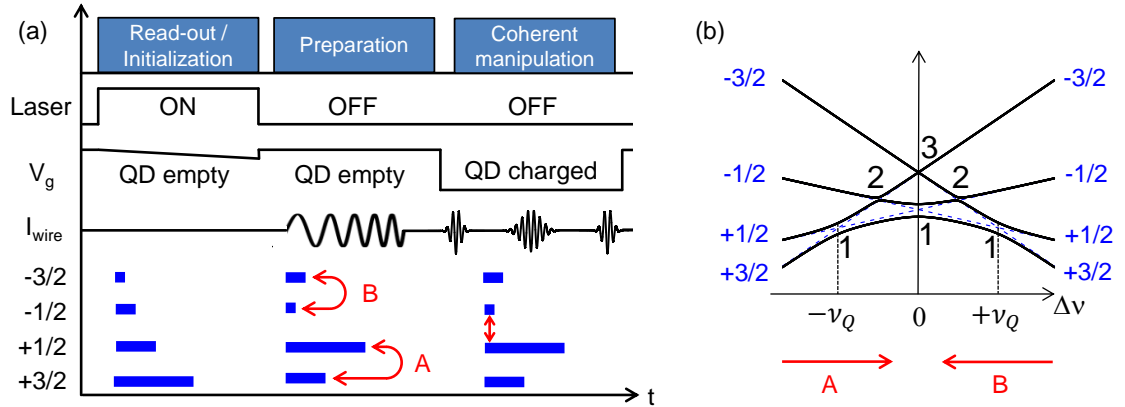


Fig. 3.1. **Measurement cycle.** (a) The initial dragging process reads the previous nuclear spin polarization and sets a new state, thermal distribution. Next, chirped pulses maximize the population difference between the  $+1/2$  and  $-1/2$  state. Finally, we charge the QD and apply a pulse resonant with the central transition. (b) Energy levels for a  $3/2$  spin in the rotating frame versus RF detuning in the limit of  $\nu_Q \gg \nu_{RF}$ . The preparation pulses are indicated by red arrows.

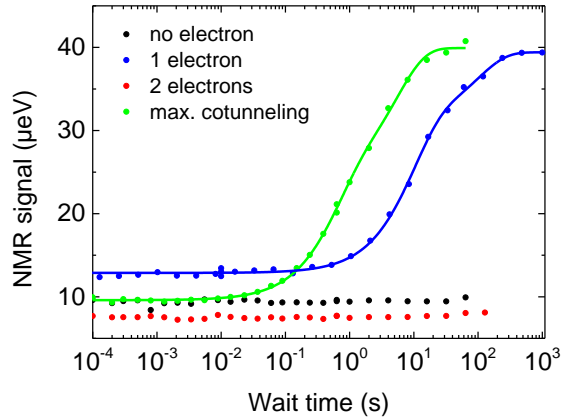


Fig. 3.2. **Decay of the nuclear spin polarization for different gate voltages.** For an uncharged and a doubly charged QD the nuclear spin polarization decays extremely slowly (order of days), see chapter A.1. The decay for a singly charged QD and in the region of maximum cotunneling is much faster, but still slow compared to the time scale of a Hahn echo measurement (50 ms). Solid lines are double exponential fits:  $\text{NMR signal} = C_0 + C_1 \exp(-t/\tau_1) + C_2 \exp(-t/\tau_2)$ . For the one electron regime (max cotunneling regime) the fit yields  $C_0 = 12.9 \mu\text{eV}$ ,  $C_1 = 18.0 \mu\text{eV}$ ,  $t_1 = 9.7 \text{ s}$ ,  $C_2 = 8.5 \mu\text{eV}$ ,  $t_2 = 101 \text{ s}$  ( $C_0 = 9.6 \mu\text{eV}$ ,  $C_1 = 14.3 \mu\text{eV}$ ,  $t_1 = 0.6 \text{ s}$ ,  $C_2 = 16.0 \mu\text{eV}$ ,  $t_2 = 5.6 \text{ s}$ ).

### 3.3 Coherence of the nuclear spin ensemble under the influence of QD charge

Applying a coherent pulse on resonance with the central transition drives the population between the  $+1/2$  and  $-1/2$  state, where the exact resonance of the central transition is determined using a method described in appendix B. Fig. 3.3 shows the NMR signal (i.e. the change in the dragging plateau width) against pulse duration for indium and arsenic in the case of three different QD charging states. Rabi oscillations, a signature of coherent manipulation, are clearly resolved in all cases. The signal is proportional to the population difference between two levels, rather than the occupancy of one level. A function of the following form was used to fit the data:

$$\text{NMR signal} = D_0 + D_1 e^{-t/\tau_{\text{Rabi}}} (\sin^2(\pi\nu_{\text{eff}}t) - 0.5). \quad (3.2)$$

The damping term results from inhomogeneous broadening of the CT, mainly due to second order quadrupolar effects<sup>12</sup>. We observe that the damping is a factor  $\sim 2$  faster for the singly charged QD compared to the empty or doubly charged QD. This effect could result from the Knight field enhancing the inhomogeneous broadening or from a reduced nuclear spin coherence due to electron mediated coupling, see below. The Rabi frequency  $\nu_{\text{eff}} = k\gamma_i B_x$  is unaffected by the charging state.  $\gamma_i$  is the gyromagnetic ratio of the respective isotope,  $B_x$  is the amplitude of the RF field and  $k$  is the scaling factor in the effective 2 level approximation (appendix A.3).  $k = 2$  for As and  $k = 5$  for In. Together with the different gyromagnetic ratios this explains the difference in the Rabi frequencies:  $\nu_{\text{eff}} = 65$  kHz for As and  $\nu_{\text{eff}} = 250$  kHz for In. These measurements confirm the results of chapter 2 that  $B_x$  is around 5 mT. Knowing  $\nu_{\text{eff}}$  we can calibrate the pulse duration for  $\pi/2$  and  $\pi$  rotations on the Bloch sphere.

Next we perform a Hahn echo measurements by applying a  $\pi/2 - \tau - \pi - \tau - \pi/2$  pulse sequence. This technique cancels out ensemble effects resulting from inhomogeneous broadening and hence reveals the inherent  $T_2$  processes. The decay of the echo amplitude is plotted against the total free precession time  $2\tau$  for In and As in the case of three different charging states in Fig. 3.4. Single exponential functions  $\sim \exp(2\tau/T_2)$  are fitted to the data to determine the coherence time  $T_2$ . For As (In) we find  $T_2 = 4.5 \pm 0.7$  ms ( $T_2 = 3.3 \pm 0.8$  ms) when the dot is empty,  $T_2 = 20 \pm 4$   $\mu$ s ( $T_2 = 25 \pm 6$   $\mu$ s) when charged with a single electron and  $T_2 = 5.1 \pm 0.8$  ms ( $T_2 = 3.0 \pm 0.7$  ms) when the dot is charged with two electrons forming a spin singlet. We note that the revival of  $T_2$  for the doubly charged QD rules out any systematic effect (loss of coherence via fast electron tunneling

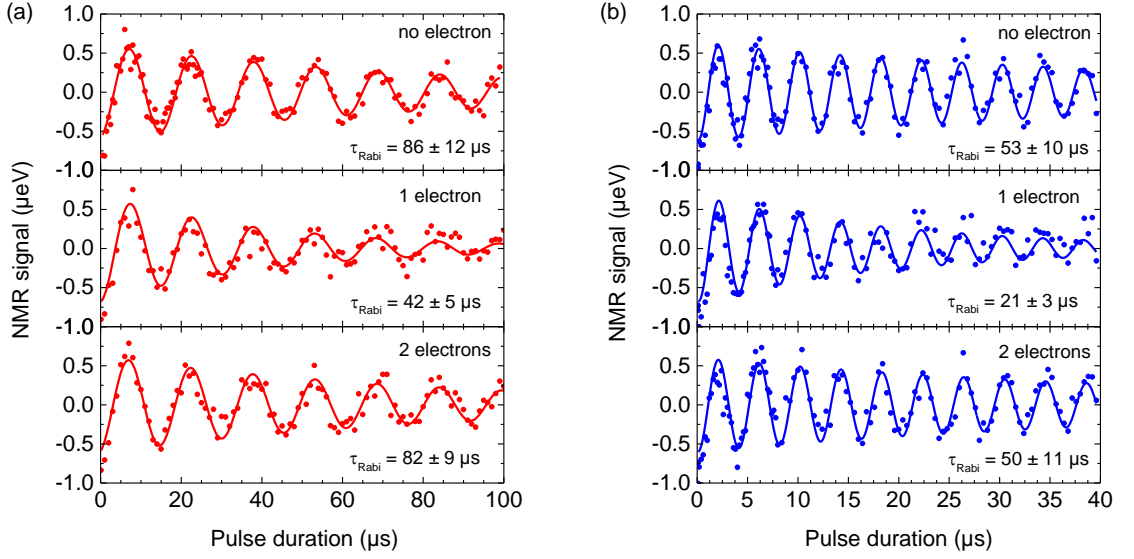


Fig. 3.3. **Rabi oscillations of the nuclear spin ensemble.** (a) Arsenic. (b) Indium. After the state preparation we charge the QD (0,1 or 2 electrons) and apply a pulse resonant with the central transition. Varying the pulse duration drives the population between the  $+1/2$  and  $-1/2$  state. The function  $D_0 + D_1 \exp(-t/\tau_{\text{Rabi}})(\sin^2(\pi\nu_{\text{eff}}t) - 0.5)$  is fitted to the data (solid lines). We find that the Rabi frequency  $\nu_{\text{eff}} = 65$  kHz for As ( $\nu_{\text{eff}} = 250$  kHz for In) is not affected by the charging. Damping of the oscillation amplitude is attributed to inhomogeneous broadening of the central transition due to second order quadrupolar effects, whereas charging the dot with a single electron increases the damping by a factor of two.

at the charging) caused by switching  $V_g$ .

A detailed investigation of  $T_2$  as a function of  $V_g$  is shown in Fig. 3.5 (b). The different charging regions (vacuum, 1  $e^-$  and 2  $e^-$ ) are identified by mapping the maximum intensity of the  $X^0$  and  $X^{1-}$  plateau (Fig. 3.5(a)). We observe a steady decrease in nuclear spin ensemble coherence from about 5 ms down to 20  $\mu\text{s}$  when  $V_g$  is changed from the empty to singly charged region and a subsequent steady recovery of  $T_2$  when  $V_g$  is tuned to the doubly charged region. In contrast, the electron spin coherence is highest at voltages corresponding to the center of the charging plateau because electron spin flip-flops due to co-tunneling to the Fermi reservoir of the back contact are strongest at the edges of the plateau<sup>14,15</sup>.

We can estimate the cotunneling rate  $\gamma_{ct}$  as a function of  $V_g$  by measuring the  $X^{1-}$  linewidth under resonant excitation and apply the model of Smith et al (Fig. 3.5(a)). In

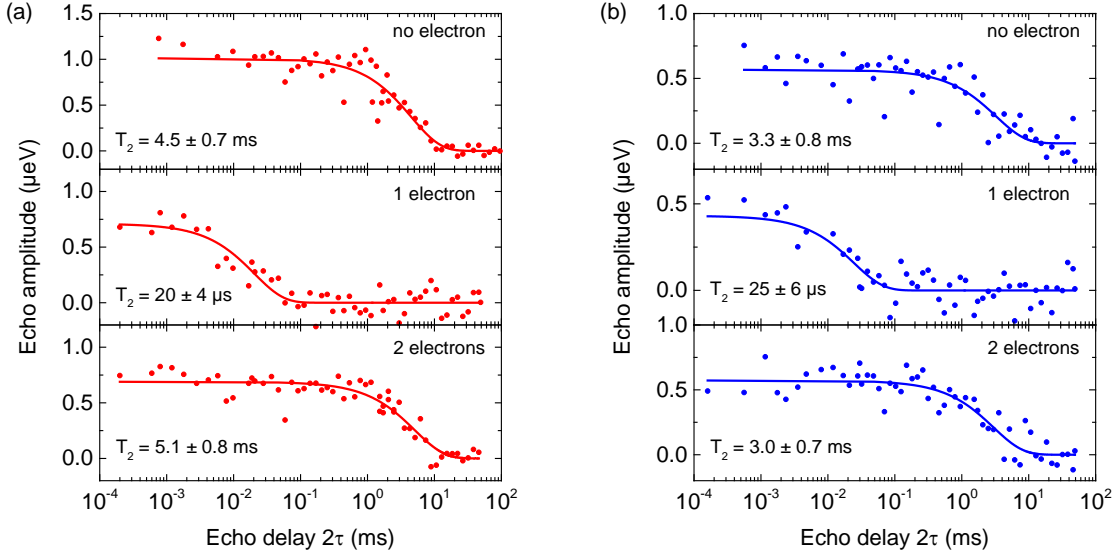


Fig. 3.4. **Hahn echo  $T_2$  measurement.** (a) Arsenic. (b) Indium. After the state preparation we charge the QD (0,1 or 2 electrons) and apply a  $\pi/2 - \tau - \pi - \tau - \pi/2$  sequence. The echo amplitude is plotted against the total delay  $2\tau$ . We use single exponential fits ( $\sim \exp(-2\tau/T_2)$ ) to determine the coherence times.  $T_2$  for the singly charged dot is more than a factor 100 lower than for the empty or doubly charged QD.

the model  $\gamma_{ct}$  is given by:

$$\gamma_{ct} = \frac{\Delta^2}{h} \int_{\epsilon} \left| \frac{1}{\epsilon + e(V_g - V_1)/\lambda + \frac{i}{2}\Gamma} + \frac{1}{e(V_2 - V_g)/\lambda - \epsilon + \frac{i}{2}\Gamma} \right|^2 \times f(\epsilon)[1 - f(\epsilon)] d\epsilon. \quad (3.3)$$

With the Fermi energy defined to lie at zero energy,  $f(\epsilon) = 1/(\exp(\epsilon/k_B T) + 1)$  is the Fermi-Dirac function,  $\Delta$  is the tunnel energy,  $\Gamma$  is the energy broadening deduced from the linewidth measurements,  $\lambda$  is the lever arm determined by the sample structure,  $V_1$  and  $V_2$  denote the edges of the charging plateau. The cotunneling rate as a function of  $V_g$  is shown in Fig. 3.5(c). At the center of the plateau we find a co-tunneling rate of  $\sim 30$  MHz. The magnitude of this value is confirmed by the absence of spin pumping combined with the knowledge of the branching ratio (appendix B).

To model the nuclear spin ensemble coherence under the presence of an electron spin Franziska Maier and Daniel Loss adapted the theory developed by Klauser *et al.*<sup>6</sup>. The details can be found in appendix B. Here we will give a qualitative description of the calculations and their relevance for the observed phenomena. In this model nuclear spins are described as spin 1/2 particles with a common gyromagnetic ratio and common

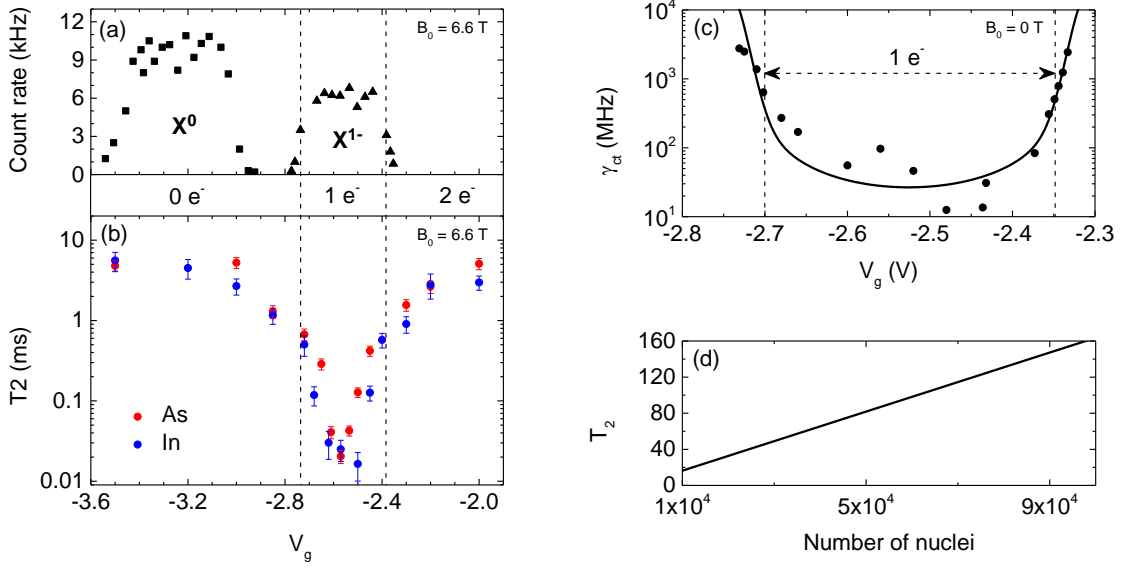


Fig. 3.5. **Nuclear and electron spin coherence times as a function of gate voltage.** (a) Maximum resonance fluorescence intensity maps of the neutral ( $X^0$ ) and singly charged exciton ( $X^{1-}$ ). Dashed lines correspond to an  $X^{1-}$  emission intensity drop of 50% and indicate the charging plateau boundaries. Here,  $0 e^-$  and  $1 e^-$  ground state energies are the same and are thus occupied 50:50. (b) Nuclear spin coherence times  $T_2$  versus  $V_g$ . (c) Co-tunneling rates extracted from linewidth measurements. The solid line describes the dependence according to the model of Smith *et al.*<sup>16</sup>, see equation 3.3. Input parameters used are:  $V_1 = -2.75$  V,  $V_2 = -2.302$  V,  $\lambda = 18.93$ ,  $\Delta = 0.21$  meV (d) Calculated nuclear spin coherence as a function of QD size based on equation 3.8, with input parameters  $\omega = 257$   $\mu$ eV,  $A = 86$   $\mu$ eV.

hyperfine coupling constant. Quadrupolar and dipolar interactions are neglected and the only coupling considered is mediated by hyperfine interactions with the electron spin, where each of the  $N$  nuclear spins is coupled to the remaining  $N - 1$  nuclear spins. In reality the nuclear spin transitions for the entire ensemble are spread over a bandwidth  $\sim 40$  MHz at  $B_0 = 6.6$  T, due to different gyromagnetic ratios and stain broadened side bands (chapter 2). Since this bandwidth is comparable to the minimum value at the cotunneling rate  $\gamma_{ct}^{min} = 30$  MHz (at center of the charging plateau, (Fig. 3.5(c))) Breit-Wiegner broadening enables coupling between all transitions. As will be shown below  $T_2$  is proportional to  $N$ . The systematic error/uncertainty on  $\gamma_{ct}^{min}$  is large, so that  $\gamma_{ct}^{min}$  can be viewed as an upper limit. For reduced  $\gamma_{ct}^{min}$  the involved number of nuclei and consequently  $T_2$  are also reduced.



The relevant Hailtonian  $H = H_0 + V$  for modelling electron mediated nuclear spin coupling is taken from Klauser *et al.*<sup>6</sup>, where:

$$H_0 = \epsilon_z S_z + \eta_z \sum_j I_j^z + S_z \text{OHS}, \quad (3.4)$$

$$V = \frac{1}{8\omega} \sum_{j \neq l} A_j A_l \left[ \left( \frac{1}{2} + S_z \right) (I_j^- I_l^+ + I_l^- I_j^+) - \left( \frac{1}{2} - S_z \right) (I_j^+ I_l^- + I_l^+ I_j^-) \right]. \quad (3.5)$$

Here,  $S_z$  is the  $z$  component of the electron spin operator,  $I_j^{z,\pm}$  ( $I_j^\pm = 1/\sqrt{2}(I_j^x \pm iI_j^y)$ ) are the components of the nuclear spin operator of the  $j$ th nuclear spin, and  $\epsilon_z$  and  $\eta_z$  are the electron spin and nuclear spin Zeeman splitting, respectively. The Overhauser shift is given by  $\text{OHS} = \sum_j A_j I_j^z$ , where  $A_j = A\nu_0 |\psi(r_j)|^2$ , where  $A$  is the averaged hyperfine coupling constant,  $\nu_0$  is the volume of a single nucleus unit cell and  $\psi(r_j) = \psi(0)e^{-(r_j/a_B)^2/2}$  is the electron envelope function (i.e. the QD is assumed to be spherical). Here, the effective Bohr radius  $a_B$  defines the total number of nuclear spins interacting with the electron spin,  $N = \frac{4}{3}\pi a_B^3/\nu_0$ .  $\omega = \epsilon_z + \text{OHS} = g_e \mu_B B_0 + \text{OHS}$  denotes the effective Zeeman splitting of the electron spin. From equation 3.5 we see that the electron mediated coupling strength in frequency units is  $\nu_{RKKY} = A_j A_l / (8h\omega)$ , where  $h$  is the Plank constant. Knowing the indium concentration of 20% (chapter 2) we calculate  $A = 86 \mu\text{eV}$  (appendix A.3). With  $g_e = -0.7$  (appendix B),  $B_0 = 6.6 \text{ T}$ ,  $\text{OHS} \sim 30 \mu\text{eV}$  (chapter 2), we determine  $\omega = 287 \mu\text{eV}$  and consequently  $\nu_{RKKY} \sim 0.78 \text{ GHz}$ . If  $S_z$  in equation 3.5 is zero the electron mediated coupling is turned off. This is of course the case for an empty dot and a doubly charged dot, when the electron spins couple to a singlet state. Furthermore, if  $S_z$  fluctuates more rapidly than  $\nu_{RKKY}$  the coupling is suppressed, this is the case at the edges of the charging plateaus, where the co-tunneling rates are high (Fig. 3.5(c)). Hence we can understand the steady decrease in  $T_2$  when  $V_g$  is tuned from the edges to the center of the charging plateau.

Although the exact dependence of  $T_2$  on  $V_g$  is not described by the model we can find a value for  $T_2$  at the center of the plateau since there  $\nu_{RKKY}$  is  $\sim 25$  times larger than  $\nu_{ct}$  and thus the effect of co-tunneling can be neglected. To do so we investigate the time evolution of the transverse component of a single nuclear spin  $\langle I_k^+(t) \rangle$  coupled to all other nuclear spins and calculate its decoherence rate:

$$\Gamma_k = \frac{A^3 \nu_0^2}{4\pi^{5/2} \hbar \omega^2 a_B^6} e^{-3(r_k/a_B)^2} \frac{r_k}{a_B}. \quad (3.6)$$

For a homogeneous ensemble polarization and short times ( $\Gamma_k t \ll 1$ , appendix B) the decoherence rate of the ensemble can be approximated by:

$$\hat{\Gamma}_N = \sum_k \Gamma_k = \frac{A^3 \nu_0}{18\pi^{3/2} \hbar \omega^2 a_B^3}. \quad (3.7)$$

Since the Bohr radius determines the number of nuclei, the nuclear spin ensemble coherence time depends linearly on the number of nuclei:

$$T_2 = \hat{\Gamma}_N^{-1} = \frac{27\sqrt{\pi}\hbar\omega}{2A} N \quad (3.8)$$

For  $\omega = 257 \mu\text{eV}$ ,  $A = 86 \mu\text{eV}$  this relation is plotted in Fig. 3.5(d). For realistic dot sizes ( $10^4 - 10^5$  nuclei)  $T_2$  is around  $20 - 150 \mu\text{s}$ . Given the simplifications of the model and the uncertainty on  $\gamma_{ct}^{min}$  this result agrees well with the measured value. We conclude that electron mediated interactions are responsible for the reduction in  $T_2$ .

### 3.4 Conclusion and Outlook

Chirped NMR pulses adiabatic for first order, but fully sudden for second order quantum transitions were used to maximize the population difference between the  $+1/2$  and  $-1/2$  spin states. The resulting boost in signal from the central transition enables pulsed NMR measurements to determine nuclear spin coherence times  $T_2$  in a highly strained nanometer sized structure. We find that  $T_2$  strongly depends on the charging state of the quantum dot: for an empty or doubly charged QD the net electron spin is zero and  $T_2$  is on the order of a few milliseconds. This prolongation in coherence compared to unstrained structures results from the suppression of nuclear dipole-dipole interactions due to atom dependent quadrupolar shifts. When charged with a single electron,  $T_2$  drops by more than two orders of magnitude. We attribute this phenomenon to an RKKY interaction, where the electron mediates spin flip-flop processes between different nuclei. This interpretation is backed up by model calculations yielding coherence times of the same order of magnitude for this type of interaction.

## References

1. Bayer, M. and Forchel, A. *Phys. Rev. B* **65**, 041308 (2002).
2. Loss, D. and DiVincenzo, D. P. *Phys. Rev. A* **57**, 120–126 (1998).
3. Liu, R. B., Yao, W., and Sham, L. J. *Advances in Physics* **59**, 703–802 (2010).
4. Chekhovich, E., Hopkinson, M., Andreev, A., Skolnick, M., and Tartakovskii, A. *ArXiv preprint, arXiv:1403.1510v2* (2014).
5. Dzhioev, R. I. and Korenev, V. L. *Phys. Rev. Lett.* **99**, 037401 (2007).
6. Klauser, D., Coish, W. A., and Loss, D. *Phys. Rev. B* **78**, 205301 (2008).
7. Warburton, R. J., Schafflein, C., Haft, D., Bickel, F., Lorke, A., Karrai, K., Garcia, J. M., Schoenfeld, W., and Petroff, P. M. *Nature* **405**, 926–929 (2000).
8. Warburton, R. J. *Nature Materials* **12**, 483 – 493 (2013).
9. Khaetskii, A. V., Loss, D., and Glazman, L. *Phys. Rev. Lett.* **88**, 186802 (2002).
10. Merkulov, I. A., Efros, A. L., and Rosen, M. *Phys. Rev. B* **65**, 205309 (2002).
11. Slichter, C. P. *Principles of Magnetic Resonance*. Springer, (1990).
12. Chekhovich, E., Kavokin, K., Puebla, J., Krysa, A., Hopkinson, M., Andreev, A., Sanchez, A., Beanland, R., Skolnick, M., and Tartakovskii, A. *Nature Nanotechnology* **7**, 646–650 (2012).
13. Latta, C., Hoegele, A., Zhao, Y., Vamivakas, A. N., Maletinsky, P., Kroner, M., Dreiser, J., Carusotto, I., Badolato, A., Schuh, D., Wegscheider, W., Atature, M., and Imamoglu, A. *Nature Physics* **5**, 758–763 (2009).
14. Atature, M., Dreiser, J., Badolato, A., Hogege, A., Karrai, K., and Imamoglu, A. *Science* **312**, 551–553 (2006).
15. Kroner, M., Weiss, K. M., Biedermann, B., Seidl, S., Manus, S., Holleitner, A. W., Badolato, A., Petroff, P. M., Gerardot, B. D., Warburton, R. J., and Karrai, K. *Phys. Rev. Lett.* **100**, 156803 (2008).
16. Smith, J. M., Dalgarno, P. A., Warburton, R. J., Govorov, A. O., Karrai, K., Gerardot, B. D., and Petroff, P. M. *Phys. Rev. Lett.* **94**, 197402 (2005).



## Chapter 4

# Bright source of red single photons from a new quantum-dot-in-nanowire system

### Adapted from:

M. Heiss, Y. Fontana, A. Gustafsson, G. Wüst, C. Margen, D. D. O'Regan, J. W. Lou, B. Ketterer, S. Conesa-Boj, A. V. Kuhlmann, J. Houel, E. Russo-Averchi, J. R. Morante, M. Cantoni, N. Marzari, J. Arbiol, A. Zunger, R. J. Warburton and A. Fontcuberta i Morral,

**“Self-assembled quantum dots in a nanowire system for quantum photonics”**,  
Nature Materials **12**, 439-444 (2013).

Quantum dots embedded within nanowires represent one of the most promising technologies for applications in quantum photonics. While the top-down fabrication of such structures remains a technological challenge, their bottom up fabrication through self-assembly is a potentially more powerful strategy. However, present approaches often yield quantum dots with large optical linewidths, making reproducibility of their physical properties difficult. We present a versatile quantum-dot-in-nanowire system which reproducibly self-assembles in core-shell GaAs/AlGaAs nanowires. The quantum dots form at the apex of a GaAs/AlGaAs interface, are highly stable, and can be positioned with nanometer precision relative to the nanowire centre. Unusually, their emission is blue-shifted relative to the lowest energy continuum states of the GaAs core. Large-scale electronic structure calculations show that the origin of the optical transitions lies in quantum confinement due to Al-rich barriers. By emitting in the red and self-assembling on silicon substrates, these quantum dots could therefore become building blocks for solid-state lighting devices and third-generation solar cells.

(Experiments and results presented in this chapter were obtained in a large collaboration. My contribution was designing, setting up, performing and analysing the following experiments to characterize the optical quality of the QDs: confocal images; continuous wave (cw) and pulsed second-order intensity correlation  $g^{(2)}(t)$  measurements; determining radiative lifetimes; determining linewidths and single photon count rates.)

## 4.1 Introduction

Semiconductor quantum dots have been shown to be excellent building blocks for quantum photonics applications, for instance single photon sources and nano-sensing applications. Desirable properties of a single photon emitter include high fidelity anti-bunching (very small  $g^{(2)}(t = 0)$ ), narrow emission lines (ideally transform limited to a few  $\mu\text{eV}$ ) and high brightness ( $> 1$  MHz count rate on standard detector). For simplicity, these properties should be achieved either with electrical injection or non-resonant optical excitation. Desirable properties of a nano-sensor include a high sensitivity to local electric and magnetic fields, with the quantum dot located as close as possible to the target region. A popular realization involves Stranski-Krastanow (SK) InGaAs quantum dots embedded in a 3D matrix, which are excellent building blocks for the realization of practical single photon sources<sup>1</sup>. However, the photon extraction out of the bulk semiconductor is highly inefficient on account of the large mismatch in refractive indices of GaAs and vacuum. An attractive way forward is to embed the quantum dots in a nanowire<sup>2</sup>. To solve the extraction problem, the nanowire is designed to operate as a single mode waveguide, a so-called photonic nanowire, with a taper as photon out-coupler<sup>3</sup>. Also, for nano-sensing applications, a quantum dot in a nanowire can be located much closer to the active medium. Top-down fabrication of the photonic waveguide is technologically complex, however. Bottom-up fabrication of the photonic waveguide is very attractive<sup>4-6</sup>, but it is presently challenging to self-assemble quantum dots in the nanowires with narrow linewidths and high yields<sup>7,8</sup>. Nano-sensing applications are presently not highly developed. Other degrees of freedom of the quantum-dot-in-nanowire system that can be usefully exploited are the mechanical modes for opto-mechanics (chapter 5); and doping for p-n junctions with applications in light harvesting<sup>9,10</sup>.

## 4.2 The quantum-dot-in-nanowire-system

We present here a promising new quantum-dot-in-nanowire system. A schematic of the physical structure is shown in Fig. 4.1(a). The structure consists of Al-poor  $\text{Al}_x\text{Ga}_{1-x}\text{As}$

( $x \sim 10\%$ ) quantum dots in an Al-rich  $\text{Al}_x\text{Ga}_{1-x}\text{As}$  ( $x \sim 60\%$ ) barrier wrapped in an intermediate Al-content matrix ( $x \sim 33\%$ ). The quantum dots form in the ridge of an AlGaAs nanowire. The self-assembly is driven by the different Ga and Al adatom mobilities on the nanowire surface, leading to Al segregation. The quantum dots can be positioned close to the nanowire surface or close to the nanowire core during the growth simply by choosing the growth mode, lateral or radial, and the overall diameter of core and shell. We note that the quantum dot size is independent of the core diameter. Significantly, the nanowire growth is not complicated by fluctuations in crystal structure (polytypism). We find that the quantum dots are very stable, surviving prolonged electron beam bombardment, exposure to air and so on, and that the quantum-dot-in-nanowire growth is very reproducible from one run to the next: there is a wide window of parameters under which they form. The quantum dots have excellent optical properties even when they are located just a few nanometers from the surface: individual quantum dots are very bright (MHz count rate) even without engineering the photonic modes, the linewidths are small (sub-100  $\mu\text{eV}$ ) and the photons are highly anti-bunched (the upper bound on  $g^{(2)}(t=0)$  is just 2%) even with intense non-resonant excitation.

An unusual feature is the *blue-shift* of the quantum dot emission relative to emission from electrons and holes in the lowest energy continuum states, in this case emission from the GaAs substrate, the core. This wavelength ordering of quantum dot and continuum emission is reversed relative to SK quantum dots. We interpret this unusual result with large scale calculations using both the empirical pseudopotential method (modeling explicitly 500,000 atoms in this dot-in-wire structure) and density functional theory (modeling a wire geometry with up to 12,000 atoms). The calculations show that whereas the states at the band edge of the system as a whole are indeed located in the GaAs layers, states at higher energy exist, confined to the quantum dot. The results are summarized in an energy level diagram (Fig. 4.1(b)), which shows the band edge valence and conduction states,  $h_0$  and  $e_0$ , and the quantum dot valence and conduction states,  $h_{\text{QD}}$  and  $e_{\text{QD}}$ . For SK dots, the continuum states are associated with the wetting layer, a thin 2D layer connecting the quantum dots, and lie at higher energy than the lowest energy quantum dot states,  $e_0$  and  $h_0$ . For the quantum-dot-in-nanowire system presented here, this energy reversal of quantum dot and continuum emission represents a new Ansatz for a solid-state single photon emitter. For SK dots, the wetting layer creates problems on non-resonant excitation: it can emit strongly<sup>11</sup> and trap charges over times comparable to the radiative lifetime<sup>12</sup>, resulting in an increase in  $g^{(2)}(t=0)$  as the pump power is increased<sup>13</sup>. These problems are bypassed here. This, along with the high material quality, is responsible for the very high fidelity photon anti-bunching

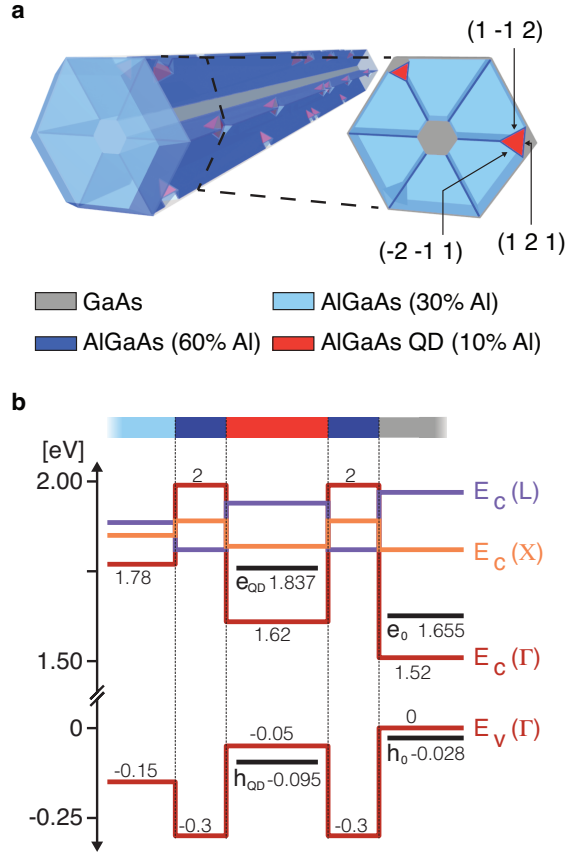


Fig. 4.1. **Schematics of the quantum-dot-in-nanowire system.** (a) The nanowire core consists of GaAs. The quantum dots form close to the outer edge of an  $\text{Al}_x\text{Ga}_{1-x}\text{As}$  shell. Aluminium segregates at the nanowire edges owing to the lower mobility of aluminium. At the outer edge of the  $\text{Al}_x\text{Ga}_{1-x}\text{As}$  layer, Al segregates further in the  $[112]$  directions leading to Al depletion and the formation of a nanoscale inclusion, an Al-poor  $\text{Al}_x\text{Ga}_{1-x}\text{As}$  quantum dot. (b) The band edge diagram showing from left to right the  $\text{Al}_x\text{Ga}_{1-x}\text{As}$  matrix and barriers, the lowest energy states confined to the quantum dot and the external GaAs capping taken from atomistic pseudopotential theory.

in the emission from a single quantum-dot-in-nanowire.

GaAs nanowires were grown by molecular beam epitaxy on a 2 inch Si (111) substrate using the gallium-assisted method<sup>14</sup>. After stopping the axial growth, the conditions were switched from axial to lateral to grow  $\text{Al}_x\text{Ga}_{1-x}\text{As}$  shells with Al compositions of  $x = 33\%$  and  $x = 51\%$ <sup>15,16</sup>. In the lower Al content shell, we also alternated the  $\text{Al}_x\text{Ga}_{1-x}\text{As}$  shells with 20 nm thick GaAs quantum wells. The nanowires were characterized structurally in cross-section using high-angle annular dark field scanning-transmission electron microscopy. Images of a GaAs nanowire covered with alternating



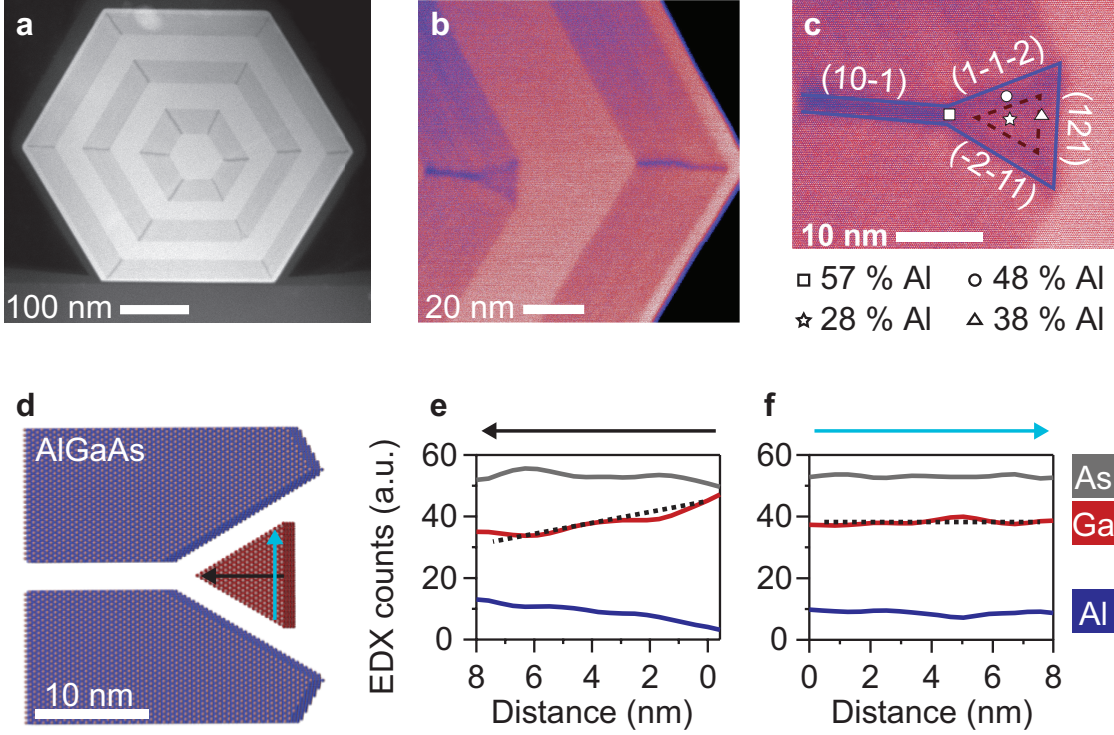


Fig. 4.2. **Structure of quantum-dots-in-a-nanowire.** (a) Aberration corrected HAADF STEM image of the entire cross-section of a GaAs nanowire coated with multiple  $\text{Al}_{0.33}\text{Ga}_{0.77}\text{As}$  /GaAs shells. (b) Zoom in of (a). (c) Detail of the Al-poor quantum dot located within the fork-like Al-rich stripes. The colouring has been chosen to enhance the contrast between the different regions. (d) 3D atomic model of the cross-sectional STEM image shown in (c). The different colours have been introduced for clarity. (e), (f) Chemical profiling of a single quantum-dot-in-nanowire using EDX (energy-dispersive X-ray) spectroscopy along two orthogonal directions.

layers of  $\text{Al}_{0.33}\text{Ga}_{0.77}\text{As}$  and GaAs are shown in Fig. 4.2(a)-(c). The lighter regions correspond to GaAs, the darker regions to  $\text{Al}_x\text{Ga}_{1-x}\text{As}$ , the contrast correlating directly with the Al content (Z-contrast). We observe the formation of dark stripes at the nanowire corners indicating Al enrichment. This accumulation is consistent with the difference in chemical potential and adatom mobility on (110) and (112)-type facets<sup>17–20</sup>. More intriguing is the morphology of some stripes at the end of the  $\text{Al}_x\text{Ga}_{1-x}\text{As}$  layer (Fig. 4.2(b),(c)). The stripes open up, leaving a region of few nanometer extent with low Al content: this region constitutes the quantum dot. Fig. 4.2(c) shows how the Al-rich stripe following the  $(10\bar{1})$  plane bifurcates into two Al-rich stripes parallel to the  $(1\bar{1}\bar{2})$  and  $(\bar{2}\bar{1}1)$  planes, forming a Y-like shape, terminated on a polar (121) plane. Chemical profiling realized by energy-dispersive X-ray (EDX) spectroscopy along the two princi-

pal directions of the quantum dot is shown in Fig. 4.2(e),(f). In the direction from the quantum dot base towards the apex, the Ga signal decreases and the Al signal increases whereas across the base, the Ga and Al signals remain constant. This information is consistent with a shape in the form of a pyramid<sup>21</sup>.

## 4.3 Optical characterization

### 4.3.1 Localizing single emitters

After the growth the nanowires are detached from the growth substrate and deposited on a silicon chip. Single emitters can be localized using photoluminescence (Fig. 4.3) or cathodoluminescence (Fig. 4.4) measurements. In both cases, in addition to a broadband emission around 820 nm (1.51 eV) which we attribute to emission from the GaAs core, we observe sharp emission lines at higher energy, in the red part of the spectrum (Fig. 4.5(a)). Representative cathodoluminescence measurements in the spectral region 630 – 690 nm (1.97 – 1.80 eV) along with the corresponding electron microscopy image are shown in Fig. 4.4. While the 820 nm CL is spatially continuous<sup>21</sup>, the 677 nm CL is spatially discontinuous along the nanowire (Fig. 4.4(b)-(d)): there is a chain of bright, nanoscale emitters. This suggests that the quantum dots identified in the structural characterization are indeed responsible for the optical emission in the red. This is reinforced by images at higher magnification (Fig. 4.4(c),(d)), which show extremely localized emitters separated laterally by less than 200 nm, corresponding to quantum dots on adjacent edges of the nanowire.

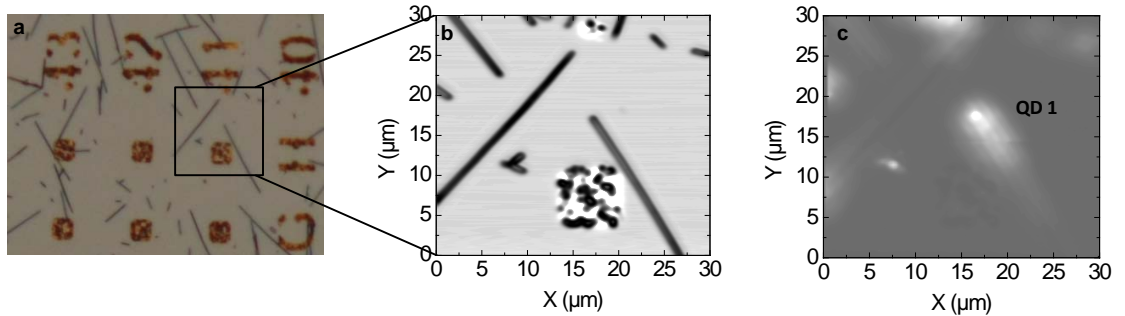


Fig. 4.3. **Confocal imaging.** (a) Light microscope image with 200x magnification. Gold markers enable orientation. (b) Confocal reflectivity scan, illumination with a laser diode ( $\lambda = 695$  nm). (c) Spectrally integrated (664-836 nm) confocal PL image from the same region as in (b), excitation with HeNe-laser ( $\lambda = 633$  nm). Strong emission from QD 1 located at the end of a NW is observed.

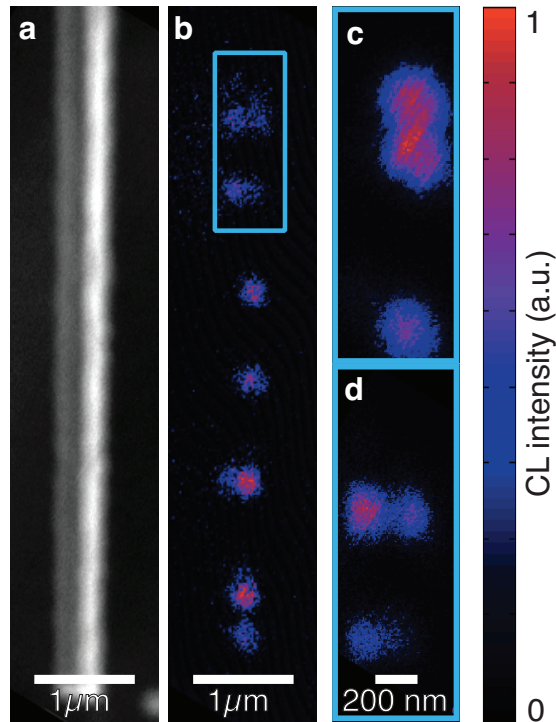


Fig. 4.4. **Cathodoluminescence of a single nanowire** (a) Electron microscopy image of a GaAs nanowire with a  $\text{Al}_{0.75}\text{Ga}_{0.25}\text{As}$  shell. (b) Cathodoluminescence (CL) mapping of a nanowire detecting emission at 677 nm. (c), (d) Detailed CL map showing spatially localized CL centres corresponding to quantum dots less than 200 nm apart on two adjacent edges of the nanowire emitting at 677 nm.

### 4.3.2 Analysing the photoluminescence polarization

Further confirmation that the structures identified in the TEM analysis are optically active comes from PL characterization of individual quantum dots. The PL was collected in a side-on geometry and its polarization dependence was measured as a probe of the dielectric environment. The broadband emission from the core is strongly polarized along the axis of the nanowire, reflecting the pronounced dielectric anisotropy (Fig 4.5 (b)). However, the sharp PL lines from individual quantum dots are preferentially polarized in quantum-dot-dependent directions, and in some cases, the polarization lies in a direction perpendicular to the nanowire axis (Fig. 4.5(b)). This observation supports the assignment of the sharp quantum dot PL lines to emitters located not on the nanowire axis but close to the surface.

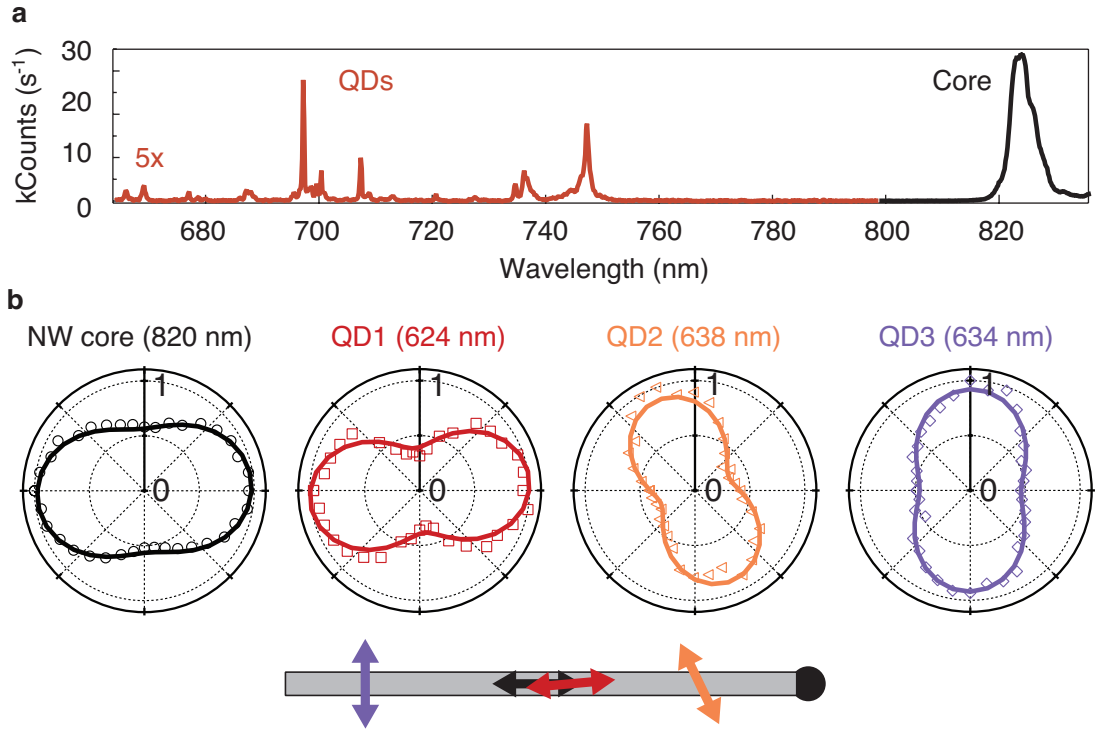


Fig. 4.5. **Photoluminescence of a quantum-dot-in-nanowire system.** (a) Photoluminescence recorded from a nanowire with non-resonant excitation at 488 nm. The broad peak at 820 nm arises from emission from the GaAs core; the sharp peaks at shorter wavelength arise from the quantum dots. (b) Azimuthal polarization analysis of the emission from the nanowire core and from three quantum dots.

### 4.3.3 Characterizing the single photon emission

A zoom-in of a typical PL spectrum of a single quantum dot is depicted in Fig. 4.6. For this particular quantum dot, the emission is centred at 676 nm (1.83 eV), with a full-width-at-half-maximum of 36  $\mu\text{eV}$ . The linewidth varies from dot to dot. The smallest linewidth observed so far is  $\sim 29 \mu\text{eV}$ , with most quantum dots showing sub-100  $\mu\text{eV}$  linewidths.

The following data was recorded from the emission of QD 1 (Fig. 4.3(c)). Exciting with a HeNe-laser ( $\lambda = 632.8 \text{ nm}$ ) the PL was sent through a Gaussian bandpass filter (FWHM = 0.5 nm) and detected with a Si avalanche photo diode without spectrally resolving the line. Fig. 4.7(a) shows how the integrated intensity increases linearly (exponent 0.99) with excitation power until the total count rate saturates at around 2 MHz. We investigate the exciton decay using a Q-switched diode laser (pulse width 80 ps) as

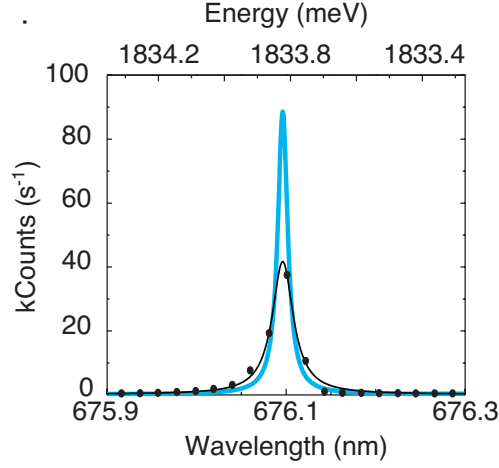


Fig. 4.6. **PL spectrum of a single quantum dot.** Recorded at  $T = 4.2$  K with  $0.03 \mu\text{W}/\mu\text{m}^2$  at wavelength 632.8 nm of excitation. The points are the measured counts on the charge-coupled-device camera, the black curve a Lorentzian fit. The blue curve corresponds to the spectrum after deconvoluting the spectral response of the detector (Lorentzian with FWHM 46  $\mu\text{eV}$ ) and therefore represents the quantum dot alone: the quantum dot PL spectrum has a FWHM of 36  $\mu\text{eV}$  for this particular quantum dot.

excitation source and time-correlated single photon counting. The decay curve is fitted extremely well over 3 decades of intensity to a convolution of a single exponential decay with the instrumental response function (IRF) (Fig. 4.7(b)). The IRF was measured with the same setup by detecting a small amount of laser light. The decay curve provides no evidence of a second decay channel: radiative decay clearly dominates. The fit yields a decay time of 450 ps. This is an important result: even though the exciton state is metastable, radiative decay is much faster than relaxation to the electron and hole ground states in the core. In other words, once an electron-hole pair is created in the quantum dot, it decays by spontaneous emission and not by electron and hole relaxation to the band edge states,  $e_0$  and  $h_0$ . The value of  $\tau$  is sub-nanosecond, consistent with a large electron-hole overlap<sup>22</sup>, i.e. inconsistent with a transition involving an electron and hole localized in different regions of space: both electron and hole are confined to the quantum dot.

In order to determine the quantum character of the emission, i. e. the nature of the anti-bunching, we have measured the time-dependence of the second-order intensity correlation  $g^{(2)}(t)$  with a Hanbury Brown-Twiss interferometer.  $g^{(2)}(t = 0)$  characterizes the fidelity of the anti-bunching. Furthermore, with cw excitation, the full  $g^{(2)}(t)$  func-

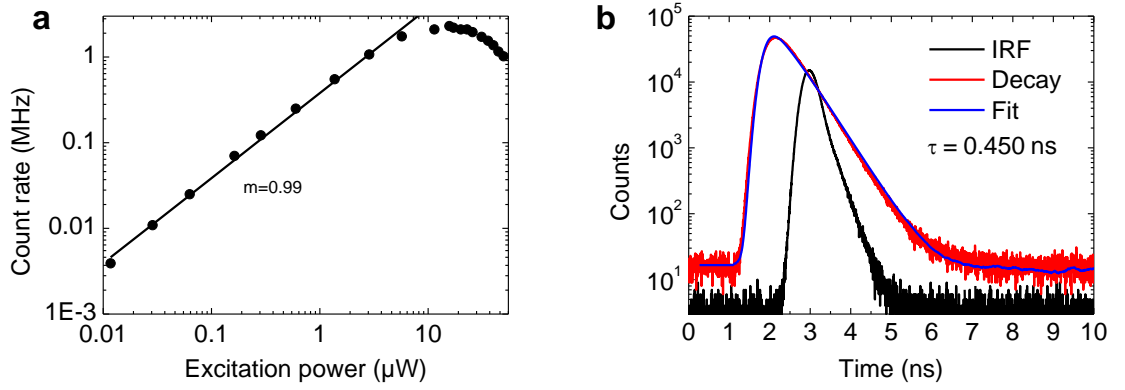


Fig. 4.7. (a) **Excitation power dependence of PL from the quantum dot.** A single photon count rate of two Megahertz is reached at saturation. (b) **Decay curve of the quantum dot.** The black curve shows the instrument response function (IRF) of the setup. Convoluting a single exponential decay with the IRF (blue curve) is used to fit the measured decay (red curve). There are no hints to a secondary decay process.

tion is sensitive to the dynamics with 2-level, 3-level systems behaving very differently. This allows us to probe if the quantum-dot-in-nanowire behaves like a 2-level atom for which  $g^{(2)}(t) = 1 - \exp(-|t|/\tau)$ . A histogram of stop-start delays with cw (HeNe-laser) excitation is shown in Fig. 4.8(a). There is a very clear dip at time delay zero ( $t = 0$ ), demonstrating anti-bunching in the photon statistics. To probe 2-level behaviour, we take  $\tau$  from the lifetime measurement, and we measure *in situ* the temporal response function of the experimental setup to quantify the jitter (dominated by the detectors). We then calculate the convolution of the 2-level atom result with the system response. Fig. 4.8(a) shows that this procedure describes the experimental results extremely well. We stress that this method does not involve any fit parameters; in fact, the agreement cannot be improved by allowing  $\tau$  to vary in a fit procedure. In this way, we find that the upper bound on the true value of  $g^{(2)}(t = 0)$  is 2%: the fidelity of the photon anti-bunching is extremely high.

The autocorrelation was also measured with the Q-switched diode laser as excitation source to complement the autocorrelation recorded with a continuous wave laser. Apart from the laser source, the setup for the autocorrelation measurement remained the same. The autocorrelation measured with the pulsed laser is shown in Fig. 4.8(b) at a laser power close to saturation. An upper bound for  $g^{(2)}(t = 0)$  is determined by integrating the counts in the peak at  $t = 0$  and dividing this by the average integrated counts in the peaks at finite delay. The upper bound on  $g^{(2)}(t = 0)$  is around 11%. Unlike the bare

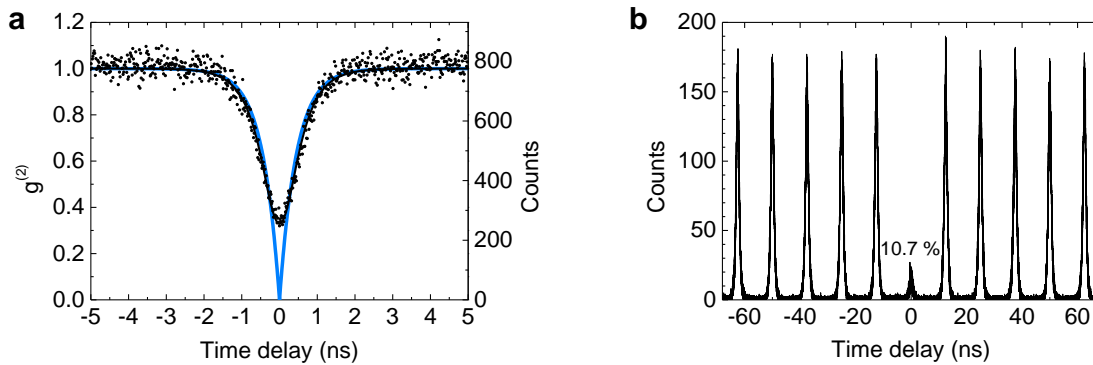


Fig. 4.8. **Second-order intensity correlations.** (a) A  $g^{(2)}$  measurement of QD 1 (Fig. 4.3(c)) using continuous wave excitation at 632.8 nm. The count rate (right  $y$ -axis) was normalized to 1 far from the dip at delay zero  $t = 0$  (left  $y$ -axis). The radiative lifetime  $\tau$  of this quantum dot was measured to be 450 ps by recording the decay curve following pulsed excitation (Fig. 4.7(a)). The black curve shows the convolution of the ideal 2-level atom result,  $g^{(2)}(t) = 1 - \exp(-|t|/\tau)$ , with the response of the detectors (Gaussian with FWHM 0.62 ns) and describes the data extremely well. The blue curve shows the 2-level atom response only. (b) A  $g^{(2)}$  measurement under pulsed (FWHM = 80 ps) excitation at 638 nm. The relative intensity of the  $t = 0$  delay peak is 11%. This deviation from 0 is understood by considering that  $\tau$  is comparable to the pulse duration, which leads to a finite probability of generating two photons per pulse.

data in the continuous wave measurement, this result is not influenced by the jitter of the detectors. It represents however an upper bound on  $g^{(2)}(t = 0)$  because the duration of the laser pulse, 80 ps, is comparable to the radiative lifetime of the quantum dot exciton, 450 ps. This means that there is a finite probability of the creation of two photons per laser pulse. These two photons should be antibunched, but the jitter of the detectors prevents us from resolving a dip in the  $t = 0$  peak. In the limit of high excitation (exciton creation on a time much shorter than the laser pulse duration), for a 2-level atom the relative integrated intensity of the  $t = 0$  peak in the autocorrelation follows  $1 - \exp(-l/\tau)$  where  $l$  is the laser pulse duration and  $\tau$  is the radiative lifetime. This ratio explains fully the observed value of 11%. In other words, the bare pulsed autocorrelation result establishes a smaller lower bound on  $g^{(2)}(t = 0)$  than the continuous wave measurement, and its analysis supports a true  $g^{(2)}(t = 0)$  value below about 2%.

However, as a more significant and general statement, we find that this quantum-dot-in-nanowire mimics a 2-level atom very closely. The origin of these 2-level-atom-like optical properties is, at first sight, not so obvious based on a comparison with the well-known SK dots. In a conventional SK InGaAs quantum dot embedded in a GaAs matrix, the GaAs has the *highest* energy band edges, higher than the InGaAs

quantum dot, and higher too than the wetting layer which forms an intermediate 2D energy band. Photoexcitation of the wetting layer creates electrons and holes which relax rapidly into the quantum dot levels. In contrast, in the current quantum-dot-in-nanowire system (Fig. 4.1(a)) GaAs forms the *lowest* energy band edges (Fig. 4.1(b)), and acts as the ultimate sink for photoexcited carriers. Furthermore, the 2.5 nm 60% Al shell at first sight poses a rather ineffective barrier for the quantum dot-confined electrons. Theoretical calculations modelling the confinement are shown in the next section.

## 4.4 Theory of the quantum confinement

To understand the two-level-like emission features at energies above the GaAs band gap, we have studied theoretically quantum confinement in these large scale nanostructures. The two state-of-the-art approaches used are the empirical pseudopotential method for a quantum-dot-in-nanowire of more than a half-million atoms, and density functional theory for a quantum wire of more than ten thousand atoms.

### 4.4.1 Pseudopotential calculations

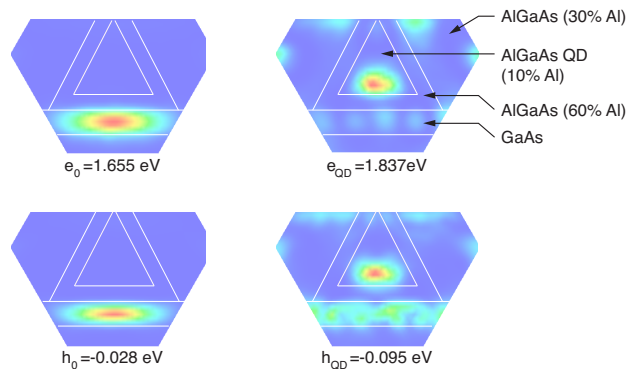


Fig. 4.9. **Pseudopotential eigenstate densities.** Results for a 10% Al content  $\text{Al}_x\text{Ga}_{1-x}\text{As}$  quantum dot, 9 nm high surrounded by a 2.5 nm thickness 60% AlGaAs barrier embedded in an 30% AlGaAs matrix and sitting on pure GaAs substrate (4 nm thickness in computational cell). Plotted are the lowest energy conduction and valence states ( $e_0$  and  $h_0$ , respectively) and the lowest energy quantum dot-bound conduction and valence states ( $e_{19}$  and  $h_{67}$ , respectively).

For the empirical pseudopotential calculations, the computational cell (Fig. 4.2(e)) contains (i) the 10% Al quantum dot with a square base in the (121) plane, quantum dot height 9.0 nm, and four facets (112), (211), (121), and (212) to complete the pyramid;



(ii) the 60% Al barrier, parallel to the quantum dot facets, having a thickness of 2.5 nm; (iii) the 30% Al layer; and (iv) the GaAs substrate, parallel to the quantum dot (121) plane containing 14 monolayers of GaAs. The total number of atoms in the computational cell is 511,104. We solve the atomistic Schrödinger equation using as potential the superposition of the atomistic pseudopotentials of Ga, Al and As at the corresponding lattice sites given by the structure, in a basis of the linear combination of bulk bands<sup>23</sup> using the folded spectrum method<sup>24</sup>, allowing the eigensolutions to be obtained in a physically interesting energy window. Excitonic effects are calculated from the single-particle states with a configuration interaction calculation. We find that the highest occupied molecular orbital (HOMO) and lowest unoccupied molecular orbital (LUMO) of the whole system reside indeed on the GaAs substrate (correspondingly, in the nanowire core) (Fig. 4.9). This supports our assignment of the broadband emission at 1.51 eV to the nanowire GaAs core. The 67 lowest hole levels of the system as a whole ( $h_0$ - $h_{66}$ ) are localized in the GaAs. The first hole state confined to the quantum dot is  $h_{\text{QD}}$  and corresponds to hole state  $h_{67}$  with energy 95 meV below the bulk GaAs valence band edge (67 meV below the system HOMO state  $h_0$ ) (Fig. 4.1(b)). For the electron states, the lowest 19 electron levels of the entire system ( $e_0$ - $e_{18}$ ) are localized on GaAs, and the first state confined to the quantum dot is  $e_{\text{QD}}$  corresponding to  $e_{19}$  with energy 317 meV above the bulk GaAs conduction band edge (182 meV above the system LUMO state  $e_0$ ) (Fig. 4.1(b)). The wave functions of states  $e_0$ ,  $h_0$ ,  $e_{\text{QD}}$  and  $h_{\text{QD}}$  are shown in Fig. 4.9. The calculated emission energy of the quantum dot-localized states is 1.902 eV (652 nm), red-shifted from the single-particle transition energy 1.932 eV by excitonic effects.

#### 4.4.2 Density functional theory calculations

Turning next to the density functional theory calculations, we have studied a quantum wire bound by polar and non-polar interfaces, thereby taking into account both internal electric fields and charge reorganisation effects. We model the 10% Al quantum dot by an infinite  $[1\bar{2}1]$  oriented wire embedded in a 60% Al matrix with thickness either 1.4 nm (5,000 atom system) or 2.5 nm (12,168 atom system) (Fig. 4.10). In both cases, the interface polarity was found to be insufficient to induce charge separation. We observe well defined quantum dot-localized states close to the valence and conduction band edges (Fig. 4.10). Using the experimental bulk GaAs band gap for the core region where the edge states are dominant, but otherwise retaining our computed band offsets, we predict transitions between these levels at 1.94 eV (640 nm), in broad agreement with both the unscreened calculation and the experimental observation. We find that the thin 1.4 nm,

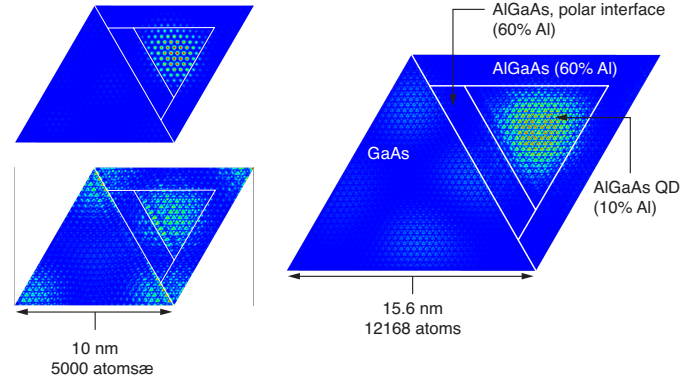


Fig. 4.10. **Localized Kohn-Sham states nearest the band edges.** Computed using self-consistent linear-scaling density functional theory, and viewed along the  $[1\bar{1}1]$  axis. (a) Highest localized valence state, 0.07 eV below the band edge, for a 5,000 atom model system ( $10.0 \times 10.0 \times 1.3 \text{ nm}^3$ , fully periodic), simulating the thin (1.4 nm) 60% Al barrier between the 10% Al quantum dot with a pure GaAs nanowire shell. (b) Corresponding conduction state, located at 0.36 eV above the band edge. (c) As (b) but for a 12,168 atom system ( $15.6 \times 15.6 \times 1.3 \text{ nm}^3$ , fully periodic, with a barrier of width 2.5 nm); 0.27 eV above the conduction edge. Figures were produced using VESTA 3<sup>25</sup>.

60% Al barrier is sufficient to provide quantum confinement irrespective of the polarity of the facets. Hence, both atomistic pseudopotential of the quantum-dot-in-nanowire and DFT of a charge-reorganised nanowire with the same cross-section predict states with both electrons and holes confined to the quantum dot.

## 4.5 Conclusion

In summary, we report the self-assembly of a high quality quantum-dot-in-nanowire system using two basic components, GaAs and AlAs. Self-assembly is not strain driven. Instead, it proceeds by the different adatom mobility of Ga and Al on the host substrate. This mechanism may well be effective with other semiconductor materials<sup>21</sup>. The shape and composition of the quantum dots has been determined by high resolution, atom-selective electron microscopy. Individual quantum dots are bright and spectrally pure emitters of highly anti-bunched light even with non-resonant excitation and even, furthermore, when they are positioned just a few nanometers from the nanowire surface. The operating principle is that both electron and hole states involved in the transition lie above the respective band edges of the nanowire itself, a point we understand quantitatively using atomistic calculations of the electronic states. In addition to applications as single photon sources, an immediate possibility is the application of these quantum dots

as nano-sensors and in forging a coupling between the optical and mechanical properties (chapter 5). By adjusting the core and shell diameters of the nanowires, the quantum dot emission can be efficiently funnelled into a waveguide mode in the nanowire. Furthermore, there are easy routes to embedding the quantum dots in a radial p-n junction<sup>26</sup> opening up applications involving not just quantum light creation but also charge control<sup>27</sup>, single photon detection<sup>28</sup> and spin<sup>29,30</sup>.

## References

1. Shields, A. J. *Nature Photonics* **1**, 215–223 (2007).
2. Borgstrom, M. T., Zwiller, V., Muller, E., and Imamoglu, A. *Nano Lett.* **5**, 1439–1443 (2005).
3. Claudon, J., Bleuse, J., Malik, N. S., Bazin, M., Jaffrennou, P., Gregersen, N., Sauvan, C., Lalanne, P., and Gerard, J. M. *Nature Photonics* **4**, 174–177 (2010).
4. Bulgarini, G., Reimer, M. E., Zehender, T., Hocevar, M., Bakkers, E. P. A. M., Kouwenhoven, L. P., and Zwiller, V. *Appl. Phys. Lett.* **100**, 121106 (2012).
5. Heinrich, J., Huggenberger, A., Heindel, T., Reitzenstein, S., Höfling, S., Worschech, L., and Forchel, A. *Applied Physics Letters* **96**, 211117 (2010).
6. Reimer, M. E., Bulgarini, G., Akopian, N., Hocevar, M., Bavinck, M. B., Verheijen, M. A., Bakkers, E. P. A. M., Kouwenhoven, L. P., and V., Z. *Nature Communications* **3**, 737 (2012).
7. Uccelli, E., Arbiol, J., Morante, J. R., and Fontcuberta i Morral, A. *ACS Nano* **4**, 5985–5993 (2010).
8. Bounouar, S., Elouneg-Jamroz, M., Hertog, M. d., Morchutt, C., Bellet-Amalric, E., André, R., Bougerol, C., Genuist, Y., Poizat, J.-P., Tatarenko, S., et al. *Nano letters* **12**, 2977–2981 (2012).
9. Agarwal, R. and Lieber, C. M. *Appl. Phys. A* **85**, 209–215 (2006).
10. Kelzenberg, M. D., Boettcher, S. W., Petykiewicz, J. A., Turner-Evans, D. B., Putnam, M. C., Warren, E. L., Spurgeon, J. M., Briggs, R. M., Lewis, N. S., and Atwater, H. A. *Nature Materials* **9**, 239 (2010).
11. Moreau, E., Robert, I., Gerard, J. M., Abram, I., Manin, L., and Thierry-Mieg, V. *Appl. Phys. Lett.* **79**, 2865–2867 (2001).
12. Moskalenko, E. S., Larsson, M., Schoenfeld, W. V., Petroff, P. M., and Holtz, P. O. *Phys. Rev. B* **73**, 155336 (2006).
13. Dalgarno, P. A., McFarlane, J., Brunner, D., Lambert, R. W., Gerardot, B. D., Warburton, R. J., Karrai, K., Badolato, A., and Petroff, P. M. *Appl. Phys. Lett.* **92**, 193103 (2008).

14. Colombo, C., Spirkoska, D., Frimmer, M., Abstreiter, G., and Fontcuberta i Morral, A. *Phys. Rev. B* **77**, 155326 (2008).
15. Heigoldt, M., Arbiol, J., Spirkoska, D., Rebled, J. M., Conesa-Boj, S., Abstreiter, G., Peiro, F., Morante, J. R., and Fontcuberta i Morral, A. *J. Mater. Chem.* **19**, 840–848 (2009).
16. Fontcuberta i Morral, A., Spirkoska, D., Arbiol, J., Heigoldt, M., Morante, J. R., and Abstreiter, G. *Small* **4**, 899–903 (2008).
17. Biasiol, G. and Kapon, E. *Phys. Rev. Lett.* **81**, 2962–2965 (1998).
18. Biasiol, G., Gustafsson, A., Leifer, K., and Kapon, E. *Phys. Rev. B* **65**, 205306 (2002).
19. Steinke, L., Cantwell, P., Zakharov, D., Stach, E., Zaluzec, N. J., Fontcuberta i Morral, A., Bichler, M., Abstreiter, G., and Grayson, M. *Appl. Phys. Lett.* **93**, 193117 (2008).
20. Skold, N., Wagner, J. B., Karlsson, G., Hernan, T., Seifert, W., Pistol, M.-E., and Samuelson, L. *Nano Letters* **6**, 2743–2747 (2006).
21. Heiss, M., Fontana, Y., Gustafsson, A., Wüst, G., Magen, C., O’Regan, D. D., Luo, J. W., Ketterer, B., Conesa-Boj, S., Kuhlmann, A. V., Houel, J., Russo-Averchi, E., Morante, J. R., Cantoni, M., Marzari, N., Arbiol, J., Zunger, A., Warburton, R. J., and Fontcuberta i Morral, A. *Nat. Mater.* **12**, 439–444 (2013).
22. Dalgarno, P. A., Smith, J. M., McFarlane, J., Gerardot, B. D., Karrai, K., Badolato, A., Petroff, P. M., and Warburton, R. J. *Phys. Rev. B* **77**, 245311 (2008).
23. Wang, L. W. and Zunger, A. *Phys. Rev. B* **59**, 15806–15818 (1999).
24. Franceschetti, A., Fu, H., Wang, L. W., and Zunger, A. *Phys. Rev. B* **60**, 1819–1829 (1999).
25. Momma, K. and Izumi, F. *Journal of Applied Crystallography* **44**, 1272–1276 (2011).
26. Colombo, C., Heiss, M., Gratzel, M., and Morral, A. F. *Applied Physics Letters* **94**, 173108–173108 (2009).
27. Bjork, M. T., Thelander, C., Hansen, A. E., Jensen, L. E., Larsson, M. W., Wallenberg, L. R., and Samuelson, L. *Nano Letters* **4**, 1621–1625 (2004).

28. Hayden, O., Agarwal, R., and Lieber, C. M. *Nature Materials* **5**, 352–356 (2006).
29. van Weert, M. H. M., Akopian, N., Perinetti, U., van Kouwen, M. P., Algra, R. E., Verheijen, M. A., Bakkers, E. P. A. M., Kouwenhoven, L. P., and Zwiller, V. *Nano Letters* **9**, 1989–1993 (2009).
30. Witek, B. J., Heeres, R. W., Perinetti, U., Bakkers, E. P. A. M., Kouwenhoven, L. P., and Zwiller, V. *Phys. Rev. B* **84**, 195305 (2011).

## Chapter 5

# Quantum Dot Opto-Mechanics in a Fully Self-Assembled Nanowire

### Adapted from:

Michele Montinaro, Gunter Wüst, Mathieu Munsch, Yannik Fontana, Eleonora Russo-Averchi, Martin Heiss, Anna Fontcumberta i Morral, Richard J. Warburton and Martino Poggio,

**“Quantum Dot Opto-Mechanics in a Fully Self-Assembled Nanowire”**,

Nano Letters **14**, 4454-4460 (2014).

We show that optically-active quantum dots (QDs) embedded in MBE-grown GaAs/AlGaAs core-shell nanowires (NWs) are coupled to the NW mechanical motion. Oscillations of the NW modulate the QD emission energy in a broad range exceeding 14 meV. Furthermore, this opto-mechanical interaction enables the dynamical tuning of two neighbouring QDs into resonance, possibly allowing for emitter-emitter coupling. Both the QDs and the coupling mechanism – material strain – are intrinsic to the NW structure and do not depend on any functionalization or external field. Such systems open up the prospect of using QDs to probe and control the mechanical state of a NW, or conversely of making a quantum non-demolition readout of a QD state through a position measurement.

(Experiments and results presented in this chapter were obtained in close collaboration with Michele Montinaro.)

## 5.1 Introduction

Experiments on micro- and nanomechanical oscillators are now addressing what were once purely theoretical questions: the initialization, control, and read-out of the quantum state of a mechanical oscillator. Researchers are able both to initialize the fundamental vibrational mode of a mechanical resonator into its ground state<sup>1,2</sup> and even to produce non-classical coherent states of motion<sup>3</sup>. The prospects are bright for exploiting these achievements to produce mechanical sensors whose sensitivity is limited only by quantum effects or to use a mechanical state to encode quantum information. The ability to initialize and observe the quantization of mechanical motion is particularly noteworthy not only from a fundamental point of view, but also because mechanical oscillators are excellent transducers. By functionalizing a resonator with an electrode, magnet, or mirror, mechanical motion can be transformed into the modulation of electric, magnetic, or optical fields<sup>4</sup>. The ease of this process has inspired proposals to use mechanical resonators as quantum transducers, mediating interactions between different quantum systems<sup>5–8</sup>. Furthermore, such couplings have now been demonstrated in a variety of quantum systems including optical<sup>9</sup> and microwave<sup>10</sup> cavities, superconducting devices<sup>11</sup>, laser-cooled atoms<sup>12</sup>, quantum dots<sup>13</sup> and nitrogen vacancy centers in diamond<sup>14–16</sup>. In most cases, however, the functionalization of the mechanical oscillator with a coupling element competes with the requirement of a small resonator mass, required for achieving a high coupling strength<sup>4</sup>. Moreover, the functionalization process often adds additional paths of dissipation and decoherence, reducing the lifetime of the coupled quantum system, or “hybrid” system.

In this letter, we report on the coupling of a nanomechanical oscillator with controllable quantum states, in which both the coupling interaction and the quantum states themselves – here, optically addressable quantum dots – are intrinsic to the oscillator’s structure. Not only is the strength of this coupling unusually strong, but its “built-in” nature produces a hybrid system whose inherent coherence is unspoiled by external functionalization and whose fabrication is simpler than top-down techniques. The specific nanoresonator that we study is a bottom-up GaAs/AlGaAs core-shell nanowire containing optically-active quantum dots<sup>17</sup>. These QDs have been shown to emit narrow optical linewidth (down to  $29 \mu\text{eV}$ ) single photons with high brightness (count rates in the MHz range)<sup>17</sup>, see chapter 4. Here we show that their energy levels are coupled to the mechanical vibrations of the NW through intrinsic material strain. We demonstrate that mechanical motion allows a reversible tuning of the QD optical frequency with no measurable influence on its photoluminescence intensity.



## 5.2 Experimental setup

Our quantum-dot-in-nanowire structures are fully self-assembled by molecular beam epitaxy (MBE). As shown schematically in Fig. 5.1(a), there is strong evidence that the QDs form at the apex of the GaAs/AlGaAs interface, in Al-poor regions embedded in the Al-rich corners of the NW hexagonal cross-section<sup>17,18</sup>, see chapter 4. QD-like emission centers observed in similar core-shell NWs have also been attributed to randomly distributed alloy fluctuations or defects within the AlGaAs shell<sup>19</sup>. In either case, by controlling the overall diameter of core and shell during growth, it is possible to position the QDs within a few nanometers of the NW surface. This proximity to the surface allows for the optimal coupling of the QDs to the strain in the NW (Fig. 5.1(b)). Despite their position near the surface, these QDs retain their high optical quality, making them ideal for sensing applications. The NWs studied here have a predominantly zinc-blende crystalline structure and display a regular hexagonal cross-section. The synthesis starts with a 290-nm thick NW core, grown along  $[1\bar{1}1]$  on a Si substrate by the Ga-assisted method detailed in Refs. 20,21. Once the NWs are about 25  $\mu\text{m}$  long, the axial growth is stopped by temporarily blocking the Ga flux and reducing the substrate temperature from 630 down to 465 °C. Then a 50-nm thick  $\text{Al}_{0.51}\text{Ga}_{0.49}\text{As}$  shell capped by a 5-nm GaAs layer is grown as detailed in Ref. 22.

In order to study the opto-mechanical coupling, individual NWs are detached from their growth substrate with micro-manipulators and glued (using an ultra-violet curing adhesive) in a cantilever configuration to the edge of a Si chip, which has been patterned with lithographically defined alignment markers (Ti/Au, 10/30 nm thick). The suspended length of the NWs typically amounts to 20  $\mu\text{m}$ . The chip is then rigidly fixed to a piezoelectric transducer (PZT), which is used to excite mechanical oscillations of the NW (Fig. 5.1(c)). The chip and PZT are mounted to a three-dimensional positioning stage which has nanometer precision and stability (Attocube AG), in a low-pressure  $^4\text{He}$  chamber ( $p = 0.35$  mbar) at the bottom of a  $^4\text{He}$  cryostat ( $T = 4.2$  K). The positioning stage allows precise alignment of individual QDs within each NW with the 400-nm collection spot of a confocal optical microscope<sup>23</sup> with high numerical aperture ( $\text{NA} = 0.82$ ). As shown schematically in Fig. 5.1(c), the microscope consists of a low-power, non-resonant HeNe excitation laser at 632.8 nm, a camera for imaging the sample, and a high-resolution spectrometer for analyzing the emitted photoluminescence (PL). The mechanical oscillation of each NW is detected via laser interferometry<sup>24</sup>. 80  $\mu\text{W}$  of laser light from a wavelength-tunable, highly coherent 780-nm laser diode are focused onto the NW free end and the reflected light is collected by a fast photodetector. A low-finesse

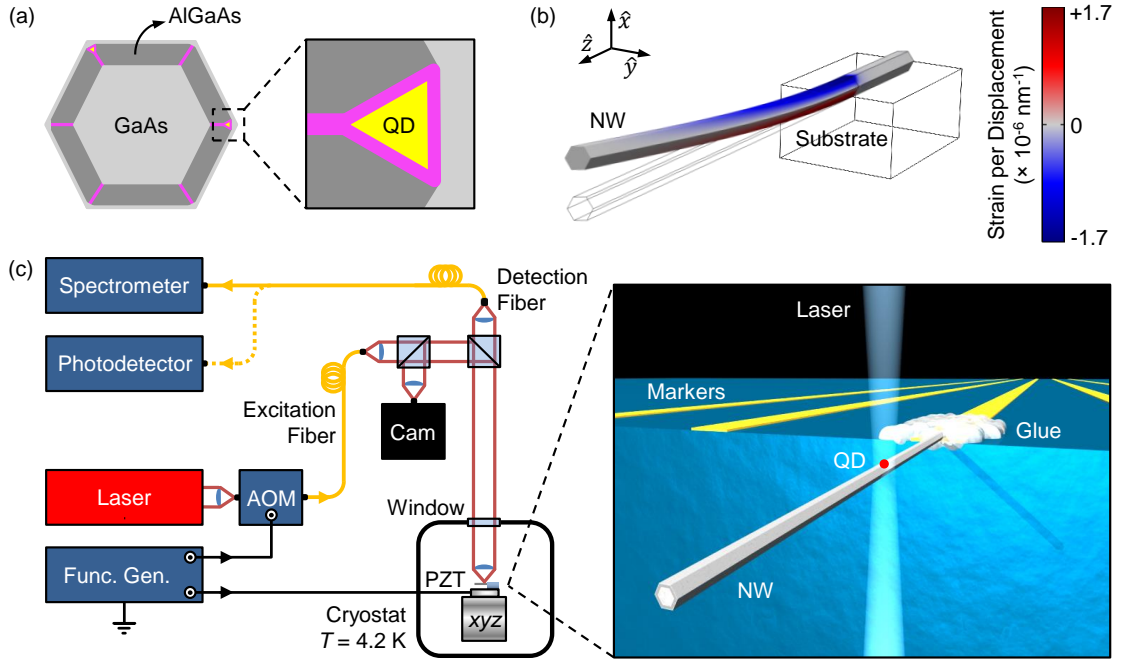


Fig. 5.1. **Experimental setup.** (a) Sketch of the NW cross-section, showing the composition of the core/shell structure and the close proximity of the QDs to the surface of the NW. The purple regions are rich in Al content and surround an Al-poor region (yellow), defining a QD<sup>17,18</sup>. (b) Finite element model of the displacement-dependent strain in the NW. The color scale is proportional to the  $\varepsilon_{zz}$  component of the strain tensor  $\varepsilon$ , computed for the prominent flexural vibration along  $\hat{x}$ . (c) Schematic diagram of the experimental setup.

Fabry-Pérot cavity, with a length of  $118 \pm 5$  cm, forms between the NW and a low-reflective window at the entrance of the  $^4\text{He}$  chamber, as confirmed by a measurement of its free spectral range. Measurements of the NW displacement by the interferometer are calibrated by an accurate determination of the laser wavelength (for more details, see appendix D).

### 5.3 Interferometry: Calibrating the motion of the nanowire free end

Using the PZT, we excite the fundamental mechanical mode of a NW and detect the resulting oscillations with the interferometer. Fig. 5.2(a) shows the spectral response of the free-end displacement  $x$  of the NW. A main resonance and a smaller peak at lower frequency are clearly observable, separated by 350 Hz. The asymmetric clamping of the

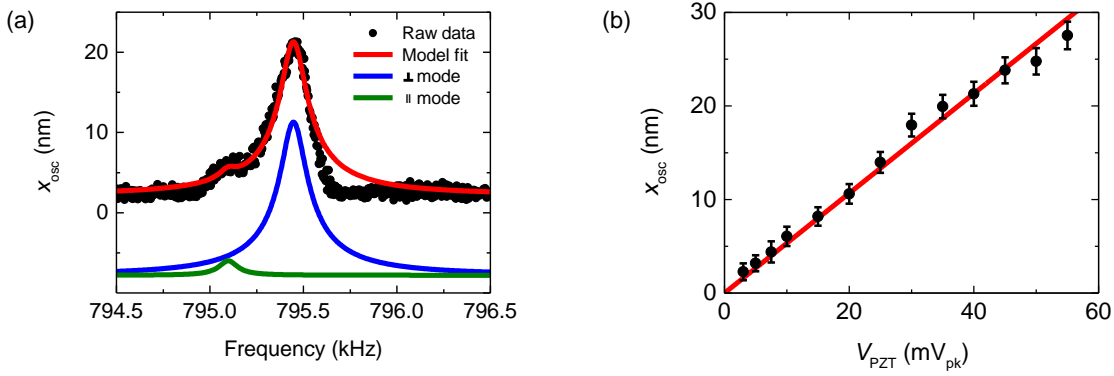


Fig. 5.2. **NW mechanical characterization.** (a) Spectrum of the NW free-end oscillation amplitude  $x_{\text{osc}}$  corresponding to its lowest order flexural vibrations at  $T = 4.2$  K, driven by the PZT at  $V_{\text{PZT}} = 40$  mV<sub>pk</sub>. The red line is a model fit (see main text), highlighting two resonances split by 350 Hz, corresponding to polarized, non-degenerate vibrational modes. The green curve represents the vibration parallel to the NW substrate, while the blue curve represents the perpendicular one (both are shifted for clarity). The mechanical quality factors of the two modes, extracted from the fit, are  $Q_{\parallel} = 7600$  and  $Q_{\perp} = 5800$ . (b) NW free-end oscillation amplitude  $x_{\text{osc}}$  as a function of the amplitude of the PZT excitation voltage  $V_{\text{PZT}}$ . The error bars correspond to the peak-to-peak amplitude of the interferometric noise. The red line is a linear fit, from which we extract the conversion factor  $\partial x / \partial V_{\text{PZT}} = 0.53 \pm 0.01$  nm/mV.

NW to the Si chip, realized by gluing the NW with one hexagonal facet in contact with the Si surface (Fig. 5.1(c)), splits the fundamental mode into a doublet of flexural modes, oriented either perpendicular or parallel to the Si surface. This interpretation is confirmed by a finite element model (FEM) of the experimental system, see appendix D. The mode oscillating perpendicular to the surface is preferentially driven by the PZT, because its oscillation direction coincides with the axis along which the PZT moves. This mode is also more easily detected by the interferometer, since its direction of oscillation coincides with the interferometer optical axis. For these reasons, we interpret the main resonance (Fig. 5.2(a)) as corresponding to the perpendicular mode. The asymmetry visible in this resonance is due to the onset of a weak mechanical non-linearity of the NW<sup>25,26</sup>. When excited in the linear regime, each of these mechanical resonances can be modeled as a driven, dissipative, harmonic oscillator<sup>27</sup>. Fitting the NW response using this model, we extract for the perpendicular mode a resonant frequency  $\Omega_0/2\pi = 795.4$  kHz and a mechanical quality factor  $Q_{\perp} = 5800$  and for the parallel mode  $Q_{\parallel} = 7600$ . Furthermore, by driving the main resonance as a function of the excitation amplitude  $V_{\text{PZT}}$ , we explore the linear regime of the NW's free-end displacement (Fig. 5.2(b)). With a linear fit, we extract a conversion factor,  $\partial x / \partial V_{\text{PZT}} = 0.53 \pm 0.01$  nm/mV, between the PZT

drive amplitude and the amplitude of the free-end displacement.

## 5.4 Spectrally resolved confocal photoluminescence imaging

We study the opto-mechanical coupling by collecting PL from individual QDs within a single NW. QDs in proximity of the clamped end of the NW have the largest energy modulation, since the oscillation-induced material strain is highest in this area (Fig. 5.1(b)). Using the scanning confocal microscope, a number of suitable QDs are identified near the clamped NW end, having bright, narrow, and spectrally isolated exciton emission lines. Fig. 5.3 shows a spatial map of the PL at 1.867 eV (664 nm) under non-resonant laser excitation of the sample. The plot also includes a weak component of reflected light at the filtered energy, which reveals the position of the NW and the Si substrate with its alignment markers. The map highlights a conveniently located QD, which we label QD 1, whose PL spectral signature includes an exciton emission peak, shown in the inset.

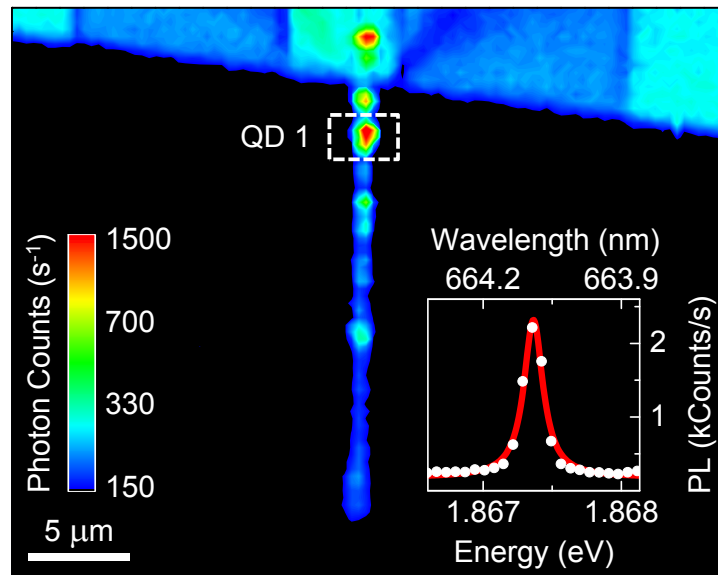


Fig. 5.3. **Spectrally filtered scanning confocal micrograph.** As a function of the excitation laser position, we plot the light intensity detected from the sample (logarithmic color scale), spectrally filtered at the peak PL energy  $E_{\text{ex}}^0 = 1.867$  eV, corresponding to exciton emission of QD 1. The inset shows the corresponding PL spectrum (white dots), together with a Lorentzian fit (red line). The linewidth (FWHM) is  $140 \mu\text{eV}$ .

## 5.5 Opto-mechanical coupling

### 5.5.1 The effect of nanowire excitation on the quantum dot photoluminescence

In the next step, the laser beam is maintained in alignment with QD 1's position and its PL spectrum is recorded as a function of the PZT excitation frequency  $\Omega/(2\pi)$ , while holding the amplitude  $V_{\text{PZT}}$  constant. Several emission peaks are detected within the same laser detection spot (Fig. 5.4(a)). As  $\Omega$  is swept through the NW resonance  $\Omega_0$ , the exciton emission peaks are broadened and deformed as a consequence of the time-integrated sinusoidal motion of the NW<sup>13</sup>. The envelope of the PL spectra as a function of  $\Omega$  resembles the NW displacement spectrum shown in Fig. 5.2(a). In particular, the low-frequency shoulder of the broadened envelope corresponds to the oscillation mode parallel to the Si surface.

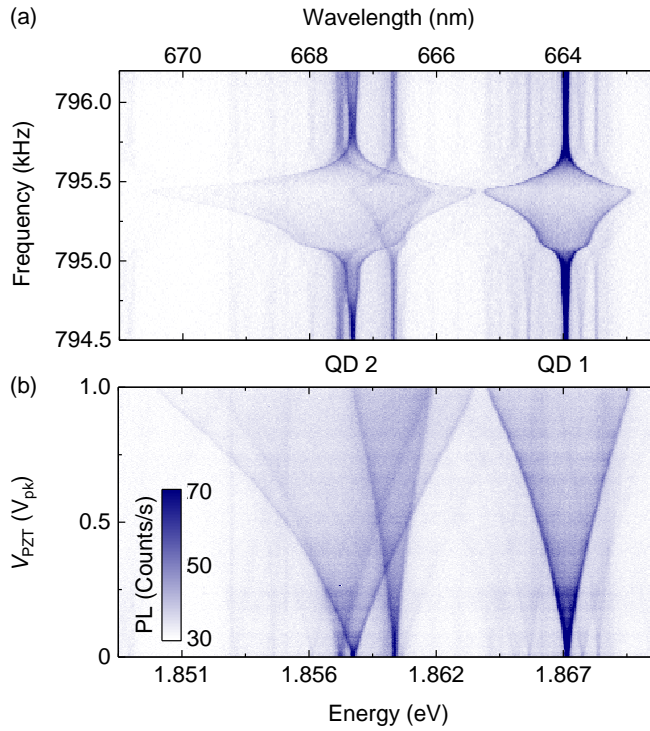


Fig. 5.4. **Effect of the NW excitation on the QD photoluminescence.** PL spectra of some neighbouring QDs (labeled QD 1 and QD 2) acquired while sweeping (a) the frequency of the PZT excitation, with  $V_{\text{PZT}} = 1 V_{\text{pk}}$ , and (b) the amplitude of the excitation, with the frequency set to the resonance of the NW's perpendicular flexural oscillation ( $\Omega = \Omega_0 = 2\pi \times 795.4$  kHz).

We explore the range of the exciton energy modulation by recording PL spectra as a function of the excitation amplitude  $V_{\text{PZT}}$ , while driving the NW on resonance with the dominant perpendicular mode ( $\Omega = \Omega_0$ ). Each spectral line exhibits a different broadening (Fig. 5.4(b)), as a consequence of its specific sensitivity to the local strain. For high excitation voltages, we observe an asymmetric energy broadening, due to the different response of the QD band structure under compressive or tensile stress in the NW<sup>28,29</sup>. Note that a further increase of the excitation amplitude leads to a saturation of the peak-to-peak exciton modulation width just beyond 14 meV. It is currently not known whether this modulation is limited merely by how hard we are able to drive the NW motion, or whether a more fundamental saturation eventually limits the range.

### 5.5.2 Determining the opto-mechanical coupling strength

While the mechanical motion of the NW in this experiment is best described in classical terms, individual PL peaks from an embedded QD can be approximated as resulting from a quantum two-level system with an exciton transition energy  $E_{\text{ex}}(x)$  between ground and excited states  $|g\rangle$  and  $|e\rangle$ <sup>17</sup>. The coupling between the NW motion and the QD can then be introduced as a shift in the exciton energy that depends on the displacement  $x$  of the NW's free end. Considering only the prominent perpendicular flexural vibration and neglecting non-linear terms in  $x$  (as in Ref. 4), the time-dependent Hamiltonian of our hybrid system can be written as:

$$\hat{H}(t) = \frac{1}{2}m\dot{x}^2 + \frac{1}{2}m\Omega_0^2x^2 + E_{\text{ex}}^0 \frac{\hat{\sigma}_z}{2} + \left. \frac{\partial E_{\text{ex}}}{\partial x} \right|_{x=0} x \frac{\hat{\sigma}_z}{2}, \quad (5.1)$$

where the first two terms describe the mechanical energy of the unperturbed NW, the third term describes the emission energy of the unperturbed QD, and the last one describes the opto-mechanical interaction. In the equation,  $m$  is the NW motional mass,  $E_{\text{ex}}^0$  is the transition energy of a QD exciton for the NW at its rest position,  $\hat{\sigma}_z = |e\rangle\langle e| - |g\rangle\langle g|$  is the Pauli operator of the two-level system, and  $\left. \frac{\partial E_{\text{ex}}}{\partial x} \right|_{x=0}$  is the opto-mechanical coupling parameter at the NW rest position. The NW motion produces a time-varying deformation of the NW's crystalline structure, in turn altering the energy levels of the embedded QD via a deformation potential, and resulting in a time-varying shift in the QD exciton emission energies. The sign and magnitude of this shift under compressive or tensile strain depend on the localization of the QD within the NW cross section and possibly on intrinsic properties of each QD<sup>30</sup>.

To evaluate the strength of the opto-mechanical coupling, we extract the PL profiles of the exciton lines (Fig. 5.5(a)) for various values of the drive  $V_{\text{PZT}}$ . The profiles

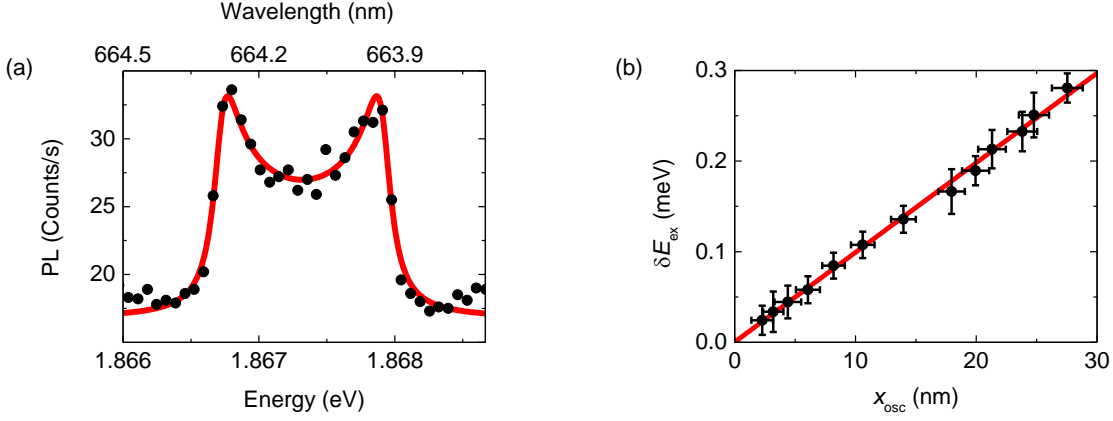


Fig. 5.5. **Strength of the opto-mechanical coupling.** (a) PL spectrum of QD 1 (black dots) under NW excitation on resonance with the perpendicular flexural mode ( $\Omega = \Omega_0$ ,  $V_{PZT} = 250$  mV<sub>pk</sub>). The red line is a model fit (see main text), from which the exciton energy shift amplitude  $\delta E_{\text{ex}}$  is extracted. (b)  $\delta E_{\text{ex}}$  of QD 2 versus the NW free-end displacement amplitude  $x_{\text{osc}}$ . The red line is a linear fit, from which we extract the opto-mechanical coupling parameter  $\left. \frac{\partial E_{\text{ex}}}{\partial x} \right|_{x=0} = 9.9 \pm 0.7$   $\mu\text{eV}/\text{nm}$ . The error bars on  $x_{\text{osc}}$  are the same as mentioned in Fig. 5.2(b); those on  $\delta E_{\text{ex}}$  are the standard deviations extracted from the fits of the mechanically excited PL spectra, as in (a).

are then fit with a Lorentzian whose central energy  $E_{\text{ex}}^0$  is modulated by a sinusoid of amplitude  $\delta E_{\text{ex}}$ <sup>14</sup>. Using our interferometer measurements (Fig. 5.2(b)), we then relate the displacement amplitude  $x_{\text{osc}}$  of the NW free end with the amplitude  $\delta E_{\text{ex}}$ . The result, displayed in Fig. 5.5(b) for QD 2 (which resides in the same optical spot as QD 1), shows that in the linear regime of mechanical excitation,  $\delta E_{\text{ex}}$  is also linear in  $x_{\text{osc}}$ . A fit to this data provides an opto-mechanical coupling parameter  $\left. \frac{\partial E_{\text{ex}}}{\partial x} \right|_{x=0} = 9.9 \pm 0.7$   $\mu\text{eV}/\text{nm}$ , which is one of the largest observed in our measurements.

The energy shift of a QD exciton can be modeled by considering the strain-dependent band structure of a semiconductor<sup>31,32</sup>. The deformation potentials and Poisson ratio have been recently measured in an experiment on zinc-blende GaAs/AlGaAs core/shell NWs grown along  $\langle 111 \rangle$ <sup>29</sup>. These parameters and a FEM of the NW strain tensor at the position of the QD in question have been used to estimate the displacement-dependent energy shift. The result of  $13 \pm 2$   $\mu\text{eV}/\text{nm}$  is in agreement with our measurement and corroborates the strain-dependence of the band structure as the dominant coupling mechanism, see appendix D.

In order to compare our results with other hybrid quantum systems<sup>4,13</sup>, the opto-mechanical interaction described in Eq. 5.1 can also be expressed in terms of the coupling

rate

$$\lambda \equiv \frac{1}{2\hbar} \left. \frac{\partial E_{\text{ex}}}{\partial x} \right|_{x=0} x_{\text{ZPF}}, \quad (5.2)$$

which is the exciton frequency shift per vibrational quantum. Here,  $x_{\text{ZPF}} = \sqrt{\frac{\hbar}{2m\Omega_0}}$  is the NW's zero-point motion at its free end and  $\hbar$  is the reduced Planck's constant. Using the FEM of the NW, we calculate its motional mass  $m = (3.5 \pm 0.7) \times 10^{-15}$  kg, where the error is dominated by the measurement imprecision of the NW thickness. This result, combined with knowledge of  $\Omega_0$ , allows us to calculate  $x_{\text{ZPF}} = (5.5 \pm 0.6) \times 10^{-14}$  m. Therefore, for QD 2, the coupling rate  $\lambda/2\pi = 66 \pm 12$  kHz. This opto-mechanical coupling rate is similar to that recently measured by Yeo *et al.*<sup>13</sup> for etched nanopillars containing self-assembled QDs, where  $\lambda/2\pi = 230 \pm 50$  kHz (note that in Ref. 13  $g_0 = 2\lambda$ ).

### 5.5.3 Stroboscopic measurement: Time evolution of the quantum dot photoluminescence

We study the time evolution of the QD exciton energy shift by acquiring stroboscopic PL spectra<sup>13,19</sup>. Two synchronized and isochronous signals drive the NW on resonance through the PZT and, using an acousto-optic modulator (AOM), chop the laser excitation with a 5% duty-cycle. The QDs are therefore excited only for 5% of the mechanical oscillation period of the NW. By recording PL spectra as a function of the phase between the two modulation signals (Fig. 5.6) we explore the temporal evolution of the QD exciton lines during a NW oscillation period. This experiment reveals exciton lines, such as those of QD 1 and QD 2 in Fig. 5.6, that respond to the mechanical oscillation of the NW with opposite shifts in emission energy. The shifts in energy induced by strain are a consequence of the change in the fundamental bands resulting from the compression or extension of the lattice constant. Therefore, for a given strain, exciton transitions from the same QD should show energy shifts of the same sign and similar magnitude. Conversely, emission lines showing drastically different shift amplitudes or even shifts with different signs correspond to QDs located at different positions within the NW cross-section. In particular, two identical QDs within the same optical collection spot, located on opposite sides of the NW neutral axis, result in opposing strains produced for the same cantilever free-end displacement. On the other hand, differences in the extension and composition of each QD may also account for the varying responses to NW motion<sup>30</sup>. When two spatially and spectrally close QD excitons display strong opto-mechanical couplings of opposite sign, their energies may become degenerate for a particular time in the oscillation period (or equivalently for a particular position of the



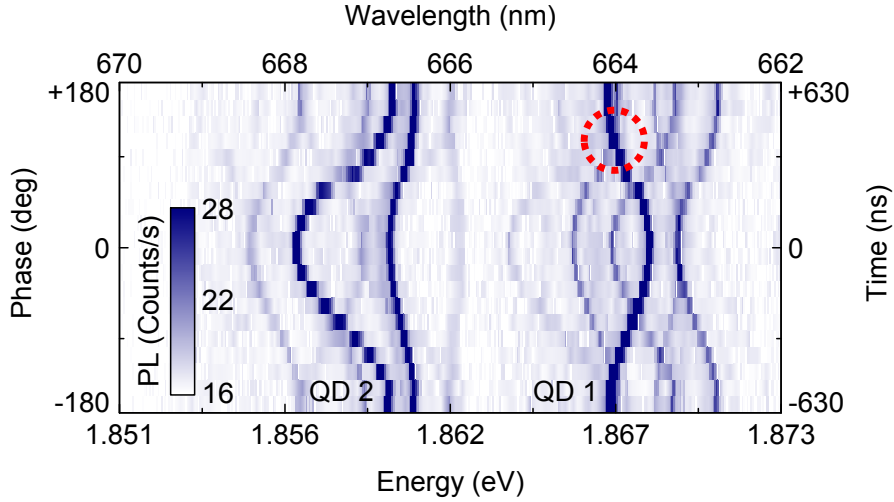


Fig. 5.6. Time-resolved PL evolution. Stroboscopic PL spectra of several neighboring QDs as a function of the phase (left axis) and the time delay (right axis) between the excitation-laser modulation and the PZT drive ( $\Omega = \Omega_0$ ,  $V_{\text{PZT}} = 250 \text{ mV}_{\text{pk}}$ ). The dashed circle highlights two exciton spectral lines dynamically tuned to the same energy.

NW free end), as for the spectral lines outlined by the dashed circle in Fig. 5.6. In the future, exploiting this mechanically mediated tuning may allow us to couple two nearby QDs within a single NW. In addition, the sinusoidal time evolution of the PL spectral lines emerging from the measurement provides a confirmation of the mechanical origin of the QD emission broadening. Note that the modulation of the QD energy has no measurable influence on the corresponding PL intensity.

## 5.6 Conclusion

Both here and in Yeo *et al.*, the ratio  $\lambda/\Omega_0$  is not far from unity, which makes these kinds of systems particularly promising for the quantum non-demolition (QND) readout of a QD state through a precise measurement of the NW displacement<sup>13</sup>. In particular, using Eqs. 5.1 and 5.2, we find that the displacement between the rest positions of the NW free end in the QD states  $|g\rangle$  and  $|e\rangle$  is  $4x_{\text{ZPF}}\lambda/\Omega_0$ . This displacement, in order to be observable, must be larger than  $x_{\text{ZPF}}$ ; in fact, at a finite temperature  $T$ , the displacement must be larger than the NW's thermal fluctuations  $x_{\text{th}}$ . This implies that a determination of the QD state can be made through a displacement measurement, if  $\lambda/\Omega_0 > \frac{1}{4}\sqrt{1+2N}$ , where  $N$  is the average phonon occupation number of the NW's fundamental mode. In the high temperature limit  $k_B T \gg \hbar\Omega_0$ , the requirement is that

$\lambda/\Omega_0 > \sqrt{\frac{k_B T}{8\hbar\Omega_0}}$ , where  $k_B$  is the Boltzmann constant. However, for our experimental parameters, the ratio  $\lambda/\Omega_0$  is still  $10^3$  times too small for such effects to be observed.

Auffèves and Richard<sup>33</sup> have recently proposed an alternative approach to such a non-demolition measurement, which takes advantage of the high  $Q$  of the NW oscillator. In their scheme, the QD is optically excited by a continuous-wave laser modulated at the NW resonance frequency. This process builds up, through constructive interference, a large coherent mechanical excitation of the NW. On resonance with a QD transition, the amplitude of the excitation is roughly  $Q$  times larger than the displacement difference calculated in the aforementioned static case. For our experimental parameters, this amplitude would be 6 times larger than the NW thermal fluctuations, making it detectable by a high-sensitivity interferometer<sup>34</sup>. It should be noted that a QND measurement also requires the time necessary to build up such a coherent phonon field ( $T_r$ ) to be smaller than the quantum transition lifetime ( $\tau_{\text{ex}}$ ), which is not the case here ( $T_r \approx 18$  ms, while  $\tau_{\text{ex}} \approx 1$  ns) nor in the experiment of Yeo *et al.*<sup>13</sup>. The use of a longer-lived QD state such as a dark exciton ( $1 \mu\text{s}$ <sup>35</sup>) or a spin state ( $0.5$  s<sup>36</sup>) could bring the system closer to the required lifetime. In addition, given a detection of the NW displacement with a large enough signal-to-noise ratio,  $T_r$  could be reduced using feedback damping, which can modify a mechanical oscillator’s response time without affecting its intrinsic properties<sup>37</sup>.

We note that prospects of quantum control over a mechanical resonator, or proposals for using a mechanical resonator as a transducer for quantum information, require the hybrid interaction to be large compared to the rates at which the coupled systems decohere into their local environments<sup>9,38</sup>. Some proposals require the condition of “large cooperativity”<sup>39,40</sup>:  $\lambda/\sqrt{\gamma_{\text{ex}}\Gamma_{\text{th}}} > 1$ , where  $\gamma_{\text{ex}}$  is the decoherence rate of the quantum transition, in our case associated to a QD exciton ( $> 1$  GHz<sup>17</sup>) and  $\Gamma_{\text{th}} = \frac{k_B T}{\hbar Q}$  is the mechanical heating rate. Using the values from this experiment, the cooperativity is  $10^{-3}$ . Nevertheless, the QD-in-NW system is particularly promising given that  $\lambda$  could be improved by a factor 2 (or bigger) for second order (or higher) flexural modes of the NW (see supporting information). Assuming that the experiment can be carried out in a dilution refrigerator at  $T = 10$  mK and that the mechanical  $Q$  can be improved to a few times  $10^6$  – perhaps by surface treatment, as was demonstrated in Si cantilevers with similar aspect ratios<sup>41</sup> – the large cooperativity limit would then become accessible.

In summary, we demonstrate an “as-grown” opto-mechanical system produced entirely by bottom-up self-assembly. The structure’s intrinsic properties couple multiple QDs to the same NW mechanical oscillator. This interaction enables the tuning of QD energies over a broad range exceeding 14 meV, opening the way for mechanically induced cou-

pling between different QDs in the NW. The sensitivity of the QDs in our system to the resonant vibration of the NW could also be used to reveal variations in the mechanical resonance frequency due to the application of electrical or magnetic forces or to a change of the mass of the NW. This fact opens the perspective of using our QD-in-NW system as an integrated force probe or as a nanomechanical mass sensor (see supporting information). By measuring the QD PL, one could monitor the NW motion in a technically simpler way than optical interferometry<sup>34,42-44</sup> or other schemes<sup>45-47</sup>.

## References

1. Teufel, J. D., Donner, T., Li, D., Harlow, J. W., Allman, M. S., Cicak, K., Sirois, A. J., Whittaker, J. D., Lehnert, K. W., and Simmonds, R. W. *Nature* **475**, 359–363 (2011).
2. Chan, J., Alegre, T. P. M., Safavi-Naeini, A. H., Hill, J. T., Krause, A., Gröblacher, S., Aspelmeyer, M., and Painter, O. *Nature* **478**, 89–92 (2011).
3. O’Connell, A. D., Hofheinz, M., Ansmann, M., Bialczak, R. C., Lenander, M., Lucero, E., Neeley, M., Sank, D., Wang, H., Weides, M., Wenner, J., Martinis, J. M., and Cleland, A. N. *Nature* **464**, 697–703 (2010).
4. Treutlein, P., Genes, C., Hammerer, K., Poggio, M., and Rabl, P. *arXiv:1210.4151* (2012).
5. Rabl, P., Kolkowitz, S. J., Koppens, F. H. L., Harris, J. G. E., Zoller, P., and Lukin, M. D. *Nat. Phys.* **6**, 602–608 (2010).
6. Kolkowitz, S., Bleszynski Jayich, A. C., Unterreithmeier, Q. P., Bennett, S. D., Rabl, P., Harris, J. G. E., and Lukin, M. D. *Science* **335**, 1603–1606 (2012).
7. McGee, S. A., Meiser, D., Regal, C. A., Lehnert, K. W., and Holland, M. J. *Phys. Rev. A* **87**, 053818 (2013).
8. Palomaki, T. A., Harlow, J. W., Teufel, J. D., Simmonds, R. W., and Lehnert, K. W. *Nature* **495**, 210–214 (2013).
9. Verhagen, E., Deléglise, S., Weis, S., Schliesser, A., and Kippenberg, T. J. *Nature* **482**, 63–67 (2012).
10. Bochmann, J., Vainsencher, A., Awschalom, D. D., and Cleland, A. N. *Nat. Phys.* **9**, 712–716 (2013).
11. Armour, A. D., Blencowe, M. P., and Schwab, K. C. *Phys. Rev. Lett.* **88**, 148301 (2002).
12. Camerer, S., Korppi, M., Jöckel, A., Hunger, D., Hänsch, T. W., and Treutlein, P. *Phys. Rev. Lett.* **107**, 223001 (2011).
13. Yeo, I., de Assis, P.-L., Gloppe, A., Dupont-Ferrier, E., Verlot, P., Malik, N. S., Dupuy, E., Claudon, J., Gérard, J.-M., Auffèves, A., Nogues, G., Seidelin, S., Poizat, J.-P., Arcizet, O., and Richard, M. *Nat. Nanotech.* **9**, 106–110 (2014).

14. Arcizet, O., Jacques, V., Siria, A., Poncharal, P., Vincent, P., and Seidelin, S. *Nat. Phys.* **7**, 879–883 (2011).
15. Teissier, J., Barfuss, A., Appel, P., Neu, E., and Maletinsky, P. *arXiv:1403.3405* (2014).
16. Ovarthaiyapong, P., Lee, K. W., Myers, B. A., and Bleszynski Jayich, A. C. *arXiv:1403.4173* (2014).
17. Heiss, M., Fontana, Y., Gustafsson, A., Wüst, G., Magen, C., O’Regan, D. D., Luo, J. W., Ketterer, B., Conesa-Boj, S., Kuhlmann, A. V., Houel, J., Russo-Averchi, E., Morante, J. R., Cantoni, M., Marzari, N., Arbiol, J., Zunger, A., Warburton, R. J., and Fontcuberta i Morral, A. *Nat. Mater.* **12**, 439–444 (2013).
18. Fontana, Y., Corfdir, P., Van Hattem, B., Russo-Averchi, E., Heiss, M., Sonderegger, S., Magen, C., Arbiol, J., Phillips, R. T., and Fontcuberta i Morral, A. *arXiv:1406.0163* (2014).
19. Weiß, M., Kinzel, J. B., Schüle, F. J. R., Heigl, M., Rudolph, D., Morkötter, S., Döblinger, M., Bichler, M., Abstreiter, G., Finley, J. J., Koblmüller, G., Wixforth, A., and Krenner, H. J. *Nano Lett.* **14**, 2256–2264 (2014).
20. Uccelli, E., Arbiol, J., Magen, C., Krogstrup, P., Russo-Averchi, E., Heiss, M., Mugny, G., Morier-Genoud, F., Nygård, J., Morante, J. R., and Fontcuberta i Morral, A. *Nano Lett.* **11**, 3827–3832 (2011).
21. Russo-Averchi, E., Heiss, M., Michelet, L., Krogstrup, P., Nygård, J., Magen, C., Morante, J. R., Uccelli, E., Arbiol, J., and Fontcuberta i Morral, A. *Nanoscale* **4**, 1486–1490 (2012).
22. Heigoldt, M., Arbiol, J., Spirkoska, D., Rebled, J. M., Conesa-Boj, S., Abstreiter, G., Peiró, F., Morante, J. R., and Fontcuberta i Morral, A. *J. Mater. Chem.* **19**, 840 (2009).
23. Högele, A., Seidl, S., Kroner, M., Karrai, K., Schulhauser, C., Sqalli, O., Scrimgeour, J., and Warburton, R. J. *Rev. Sci. Instrum.* **79**, 023709 (2008).
24. Bruland, K. J., Garbini, J. L., Dougherty, W. M., Chao, S. H., Jensen, S. E., and Sidles, J. A. *Rev. Sci. Instrum.* **70**, 3542–3544 (1999).
25. Nichol, J. M., Hemesath, E. R., Lauhon, L. J., and Budakian, R. *Appl. Phys. Lett.* **95**, 123116 (2009).

26. Braakman, F., Cadeddu, D., Fontcuberta i Morral, A., and Poggio, M. *arXiv:1406.5961* (2014).
27. Montinaro, M., Mehlin, A., Solanki, H. S., Peddibhotla, P., Mack, S., Awschalom, D. D., and Poggio, M. *Appl. Phys. Lett.* **101**, 133104 (2012).
28. Bryant, G. W., Zieliński, M., Malkova, N., Sims, J., Jaskólski, W., and Aizpurua, J. *Phys. Rev. B* **84**, 235412 (2011).
29. Signorello, G., Karg, S., Björk, M. T., Gotsmann, B., and Riel, H. *Nano Lett.* **13**, 917–924 (2013).
30. Jöns, K. D., Hafenbrak, R., Singh, R., Ding, F., Plumhof, J. D., Rastelli, A., Schmidt, O. G., Bester, G., and Michler, P. *Phys. Rev. Lett.* **107**, 217402 (2011).
31. Chandrasekhar, M. and Pollak, F. H. *Phys. Rev. B* **15**, 2127–2144 (1977).
32. Van de Walle, C. G. *Phys. Rev. B* **39**, 1871–1883 (1989).
33. Auffèves, A. and Richard, M. *arXiv:1305.4252* (2013).
34. Nichol, J. M., Hemesath, E. R., Lauhon, L. J., and Budakian, R. *Appl. Phys. Lett.* **93**, 193110 (2008).
35. McFarlane, J., Dalgarno, P. A., Gerardot, B. D., Hadfield, R. H., Warburton, R. J., Karrai, K., Badolato, A., and Petroff, P. M. *Appl. Phys. Lett.* **94**, 093113 (2009).
36. Bar-Gill, N., Pham, L. M., Jarmola, A., Budker, D., and Walsworth, R. L. *Nat. Commun.* **4**, 1743 (2013).
37. Poggio, M., Degen, C. L., Mamin, H. J., and Rugar, D. *Phys. Rev. Lett.* **99**, 017201 (2007).
38. Gröblacher, S., Hammerer, K., Vanner, M. R., and Aspelmeyer, M. *Nature* **460**, 724–727 (2009).
39. Clerk, A. A., Marquardt, F., and Jacobs, K. *New J. Phys.* **10**, 095010 (2008).
40. Hammerer, K., Aspelmeyer, M., Polzik, E. S., and Zoller, P. *Phys. Rev. Lett.* **102**, 020501 (2009).
41. Rast, S., Gysin, U., Ruff, P., Gerber, C., Meyer, E., and Lee, D. W. *Nanotechnology* **17**, S189 (2006).

42. Carr, D. W. and Craighead, H. G. *J. Vac. Sci. Technol. B* **15**, 2760–2763 (1997).
43. Belov, M., Quitoriano, N. J., Sharma, S., Hiebert, W. K., Kamins, T. I., and Evoy, S. *J. Appl. Phys.* **103**, 074304 (2008).
44. Favero, I., Stapfner, S., Hunger, D., Paulitschke, P., Reichel, J., Lorenz, H., Weig, E. M., and Karrai, K. *Opt. Expr.* **17**, 12813–12820 (2009).
45. Treacy, M. M. J., Ebbesen, T. W., and Gibson, J. M. *Nature* **381**, 678–680 (1996).
46. Montague, J. R., Dalberth, M., Gray, J. M., Seghete, D., Bertness, K. A., George, S. M., Bright, V. M., Rogers, C. T., and Sanford, N. A. *Sens. Act. A* **165**, 59–65 (2011).
47. Hoch, S. W., Montague, J. R., Bright, V. M., Rogers, C. T., Bertness, K. A., Teufel, J. D., and Lehnert, K. W. *Appl. Phys. Lett.* **99**, 053101 (2011).





# Chapter 6

## Conclusions and outlook

### Nuclear magnetic resonance on a quantum dot

In the first part of this thesis NMR techniques are applied to investigate the nuclear spin ensemble of a semiconductor quantum dot. The challenges are the mesoscopic size ( $\sim 10^5$  spins) and the high inhomogeneity (4 different isotopes with widely different gyromagnetic ratios, high spin numbers, atom dependent quadrupolar shifts) of the ensemble. Resonance fluorescence is used to set and read the nuclear spin polarization optically. To generate the high amplitude radio frequency (RF) pulses needed for efficient nuclear spin manipulation a low impedance, high bandwidth gold micro-wire was fabricated on top of a standard charge tunable device.

We show that frequency swept RF pulses can invert the nuclear spin polarization back and forth over one hundred times before the signal is lost. More detailed measurements enable the determination of all key properties of the nuclear spin ensemble: the chemical composition, the effective temperatures and quadrupole frequency distribution of each isotope. These properties determine the pulse parameters (sweep rate, frequency range and amplitude) needed for the preparation of non-thermal states. In the next experiment, this knowledge is exploited to maximize the population difference between the central transition, enabling the observation of Rabi oscillations and Hahn echo  $T_2$  measurements. For an uncharged dot  $T_2$  is on the order of 5 ms. Charging with a single electron reduces  $T_2$  to 20  $\mu$ s. We present a theory attributing this drastic reduction to electron mediated coupling between the nuclei, an RKKY-type interaction. This is supported by the recovery of  $T_2$  when the dot is charged with two electrons.

As an outlook, we note that the techniques used for the preparation of non-thermal states in principle allow for fast population inversion and the observation of Stückelberg oscillations, a fascinating quantum interference phenomenon. Furthermore, fabricating a sample with a p-doped back contact would enable to investigate the effect of a hole on nuclear spin coherence. This could lead to new insights in the hyperfine coupling between hole spin and nuclear spins.

### A quantum dot in a nanowire

We investigate the emission from a fully self-assembled quantum-dot-in-nanowire system. The NWs consist of a GaAs core surrounded by an AlGaAs shell. During the growth of the shell segregation effects lead to the formation of Al poor regions encapsulated by a thin Al rich barrier establishing a 3D confinement. Under non-resonant excitation the quantum dots emit around 650-730 nm. Interestingly, this is at shorter wavelengths than emission from the nearby continuum formed by the GaAs core ( $\sim 830$  nm). CW and pulsed second order intensity correlation measurements demonstrate the highly antibunched nature of the emission ( $g^{(2)}(t=0) \leq 2\%$ ). Single photon count rates of 2 MHz are observed on a conventional single photon detector. Decay curve measurements following pulsed excitation determine the radiative lifetime  $\tau_{rad} \sim 0.5$  ns. We emphasise that the CW  $g^{(2)}$  measurement perfectly mimics the behaviour of a two level atom, no additional assumptions are needed to describe the data.

In the next experiment we investigate the opto-mechanical coupling between QD emission energy and the driven mechanical motion of the NW. Here, tensile/compressive stress alters the lattice constant and consequently changes the band gap, thus modulating the QD emission energy. These modulations can exceed 14 meV, when the NW's oscillation modes are driven on resonant. Interferometric calibration of the NW's free end motion enables determination of the opto-mechanical coupling rate  $\lambda = 66 \pm 12$  kHz. Furthermore, stroboscopic measurements reveal the time evolution of QD emission and show that two QDs within the focal spot can be tuned dynamically into resonance.

As an outlook, we note that constructing radial p-n junctions could enable electrically driven single photon generation and charge control, the latter would greatly simplify the implementation of resonant laser spectroscopy. The opto-mechanical coupling is a route to non-demolition readout of QD states by detecting the NW's free end position. Strain can also modulate the  $g$ -factor and thus facilitate the coupling between the electron/hole spin located in the QD and the NW motion. Furthermore, the QD is natural probe to detect shifts in the NW's resonance frequency. This enables detection of electrical and magnetic forces or changes in mass.

# Appendix A

## Supplementary information to chapter 2

### A.1 Experimental details

#### A.1.1 Sample

The sample consists of low density self-assembled InGaAs/GaAs quantum dots (QDs) grown by molecular beam epitaxy embedded in the intrinsic region of an n-type GaAs Schottky diode (Fig. A.1). The layers in the heterostructure are:

1. Back gate: 50 nm Si-GaAs, doping  $n = 1.7 \times 10^{18} \text{ cm}^{-3}$
2. Tunnel barrier: 25 nm i-GaAs
3. Active region: InGaAs QDs
4. Capping layer: 434.3 nm i-GaAs
5. Blocking barrier: 64 periods of 3 nm/1 nm AlAs/GaAs
6. Top cap: 10 nm i-GaAs
7. Top gate: 3 nm/7 nm Ti/Au

To generate the longitudinal radio frequency (RF) field we fabricate a gold microwire directly on the sample. With a shadow mask we first deposit a 464 nm ( $= \frac{3}{4}\lambda$ ,  $\lambda = 950 \text{ nm}$ ) thick  $\text{SiO}_2$  spacer onto the top gate, which serves as an electrical and thermal insulator and as an anti-reflection coating. We then deposit a 10/200 nm Ti/Au microwire with a photolithography procedure. The wire is 20  $\mu\text{m}$  long, 6  $\mu\text{m}$  wide and has a 2  $\mu\text{m}$  by 6  $\mu\text{m}$  hole, through which QD emission is detected (Fig. A.2). On top of the structure, a  $\text{ZrO}_2$  solid immersion lens (SIL) (refractive index 2.15) is used to increase the detection efficiency by a factor of  $\sim 5$ . Markers fabricated together with the microwire allow the SIL to be centred precisely. To contact the back gate we deposit 120 nm AuGe and 10 nm Ni and anneal the sample at 450 °C.

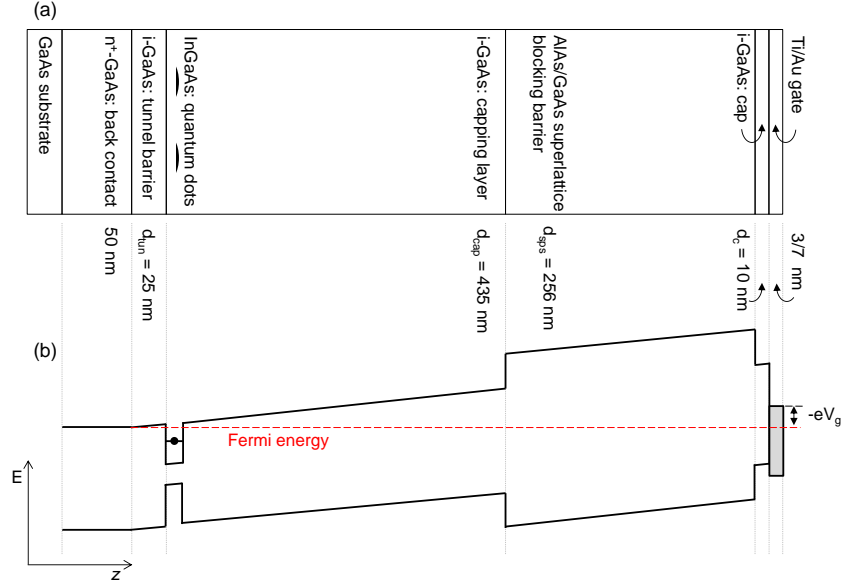


Fig. A.1. **Sample structure.** (a) Layer structure of our sample. (b) Associated band structure. Applying a voltage  $V_g$  between top gate and back gate allows the QD energy levels to be tuned relative to the Fermi energy, which is determined by the  $n^+$ -doping of the back gate. Here the ground state of the  $X^{1-}$  is shown. The lever arm (distance between top and back gate divided by the thickness of the tunnel barrier) is 28.6.

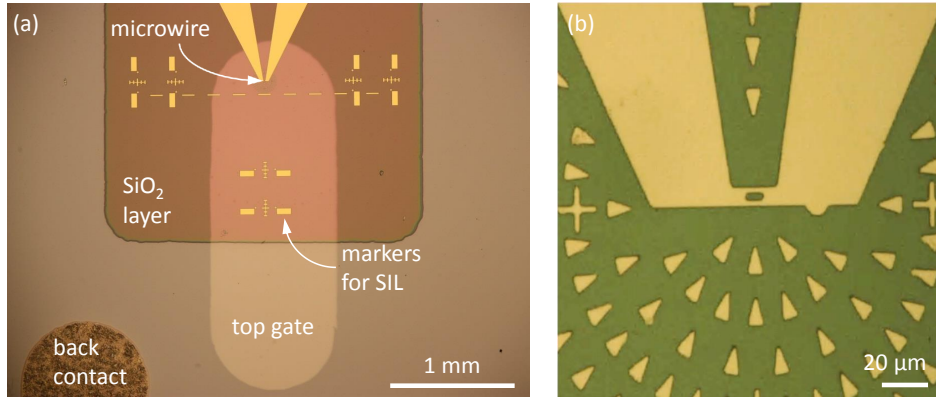


Fig. A.2. **Top view of sample.** (a) Shadow masks are used to deposit back contact, top gate and  $\text{SiO}_2$  spacer layer. Microwire and markers for positioning the solid immersion lens are fabricated in one photolithography step. We minimize the overlap of the microwire and the top gate to reduce the risk of electrical shorts. Reducing the area of the  $\text{SiO}_2$  layer circumvents adhesion problems. (b) Zoom in on the microwire. A hole in the wire enables optical access to the QD emission. Triangular markers facilitate the positioning of the sample in the microscope.

### A.1.2 Set-up

The sample is cooled down to 4.2 K in a helium bath cryostat (Fig. A.3). A superconducting magnet provides a static field  $B_z$  up to 9 T along the growth direction (Faraday geometry).

Initialization and read-out of the nuclear spin polarization is performed optically. We use resonant excitation of the  $X^0$  transition which leads to the creation of a single electron-hole pair with no excess carriers. The resonance fluorescence is detected with a confocal dark-field microscope<sup>1</sup>. At  $B_z = 0$  T, the ultra-high quality of the sample is revealed by the small measured linewidth of 1.2  $\mu\text{eV}$ , close to the ideal transform limit of  $\sim 0.9$   $\mu\text{eV}$  (Fig. 2.3) of chapter 2). At  $B_z = 6$  T sweeping the laser energy across the blue Zeeman transition of the  $X^0$  leads to dynamical nuclear spin polarization via the so called “dragging effect”<sup>2,3</sup>. The result is a characteristic flat-top spectrum. In practice, the detuning is achieved by sweeping the voltage applied to the gate,  $V_g$ . For the  $X^0$ , the Stark shift amounts to  $0.447 \pm 0.002$   $\mu\text{eV}/\text{mV}$ .

Two arbitrary waveform generators (AWGs) control and synchronize the experiment. The first one controls the voltage applied to the gate, as well as the laser intensity via an acousto-optic modulator (AOM) double passage set-up. The second one generates chirped pulses at radio frequencies. Its 512 MB internal memory allows for a maximum pulse duration of 1.3 s at a maximum sampling rate of 200 MHz. The output voltage is sent to a RF amplifier and corrected for the frequency dependent gain of the amplifier. High pass (HP) filters at 25 MHz and low pass filters (LP) at 150 MHz eliminate possible noise. The signal is then split into two co-axial cables of the same length which go down into the cryostat. The last  $\sim 5$  cm of the connection is made by a twisted pair. In one arm, the phase of the signal is shifted by  $\pi$  to avoid electric fields at the microwire which could influence the QD signal via the Stark effect. The DC-resistance measured at the top of the cryostat is  $R = 3.5 \Omega$ . The amplitude of the output voltage at the top of the cryostat is measured over a  $50 \Omega$  resistance and kept at  $V_{\mu\text{wire}} = 10$  V for all data presented in this work.

We sometimes observe random “rigid” shifts in the QD spectrum. For high voltages ( $V_{\mu\text{wire}} \geq 12$  V) these shifts become disruptively large (up to 100  $\mu\text{eV}$  to both higher or lower energy). We attribute these rigid shifts to a reorganisation of the defect charges in the vicinity of the QD. Importantly, our read-out technique allows us to distinguish between these rigid shifts and the nuclear spin effects. In particular, the Overhauser shift is measured by the width of the dragging plateau which does not depend on the absolute frequency of the QD resonance. The data in Fig. 2.4 of chapter 2 are corrected from these rigid shifts.

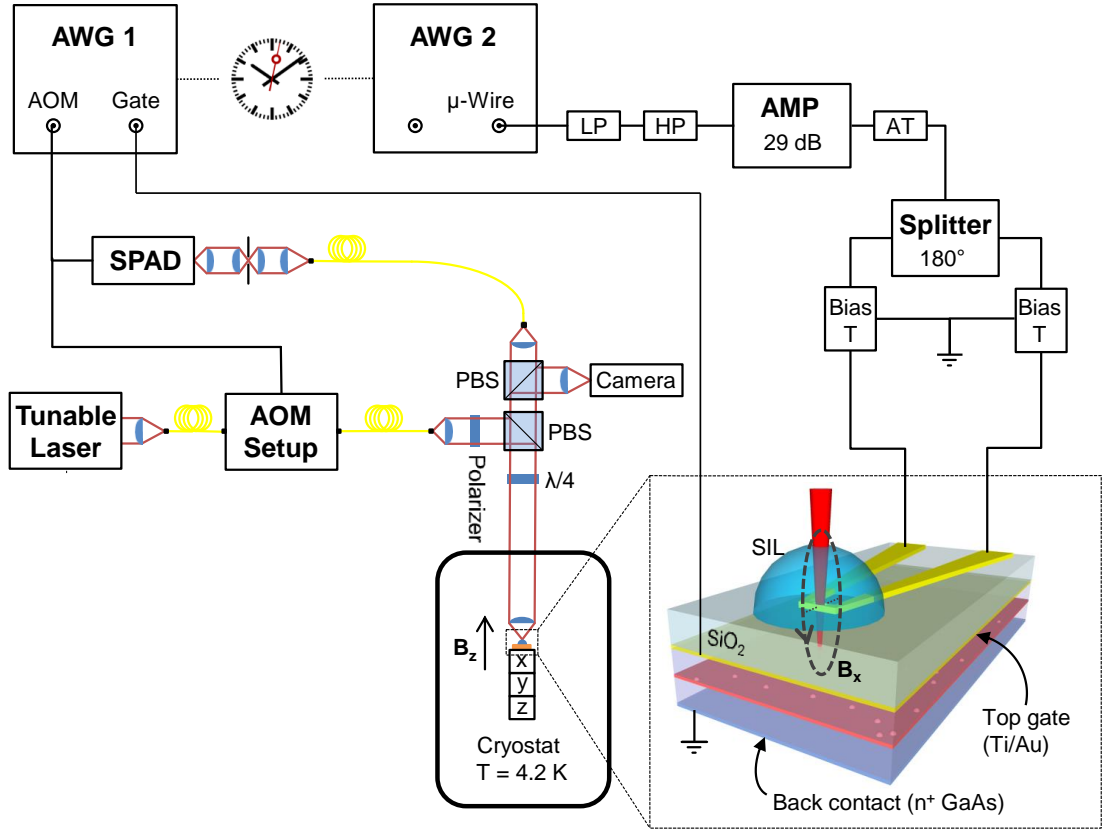


Fig. A.3. **Experimental set-up.** The sample is mounted on a stack of X/Y/Z-piezo positioners and held at  $T = 4.2$  K. Polarizing beam splitters (PBS), a polarizer and a quarter wave plate ( $\lambda/4$ ) within the resonance fluorescence head enable high quality cross polarization between detection and excitation. A spatial filter in front of the single photon avalanche diode ensures a low dark count rate of  $\sim 10$  counts/s. AWG 1 controls the laser intensity (via an AOM setup) and the laser detuning by sweeping the gate voltage. AWG 2 generates the chirped RF pulses which are then sent to a current amplifier (AMP). High pass (HP) and low pass (LP) filters eliminate any unwanted noise and attenuators (AT) are used to adjust the amplitude. The signal is then sent through a splitter which induces a  $180^\circ$  phase shift between the different arms, thereby minimizing the electric field at the wire.

## A.2 Supporting experimental results

### A.2.1 Depolarization procedure

In order to randomize the QD spin ensemble, we use a series of short pulses whose frequencies cover the whole 55 MHz bandwidth spanned by the QD nuclei at  $B_z = 6$  T. After a few minutes, the system reaches a stationary state, which corresponds to com-

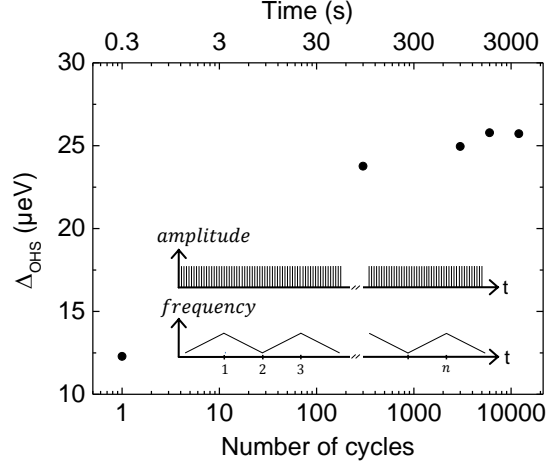


Fig. A.4. **Randomization of the QD nuclear spin ensemble.** The randomization signal is obtained with current pulses in the wire at 25 kHz, with a duty cycle of 10% (see inset). The frequency is swept over 55 MHz to cover the complete bandwidth spanned by the QD nuclear spins. After  $\sim 600$  s the system reaches a stationary state.

plete depolarization of the sample. This is reported in Fig. A.4, where we plot the dragging plateau width as a function of the number of cycles. Before each measurement the system is initialized by dragging the QD transition from the blue, as described in chapter 2. The pulse duration is set to  $4 \mu\text{s}$ , with a repetition rate of 25 kHz.

## A.2.2 Nuclear-spin lifetime

A measurement of the nuclear spin relaxation in the lab frame shows that, after 22 hours, less than 30% of the initial polarization has relaxed (Fig. A.5). The  $T_1$  time of the nuclear spin ensemble clearly exceeds one day (we note that the decay is not a simple exponential). This extremely long decay time arises as a consequence of the suppression of nuclear spin diffusion into the bulk due to the strained environment of the QD<sup>4</sup> and the low temperature. Hence for experiments on an uncharged QD, we can neglect relaxation on the time scale of our experiments.

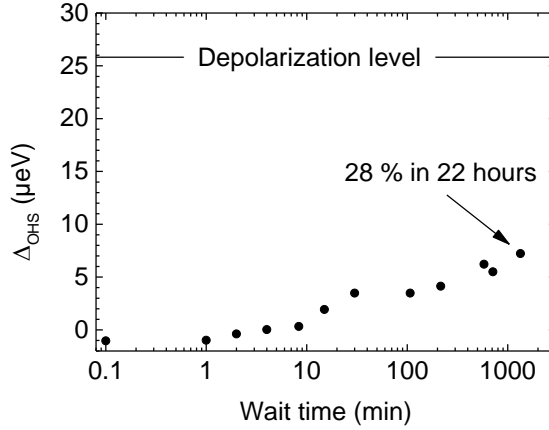


Fig. A.5. **Nuclear spin relaxation in the laboratory frame.** The change in Overhauser shift following the decay of nuclear spin polarization is extremely slow and can be neglected on the few minute time scale of our experiments.

### A.2.3 Measurement of Rabi oscillations and estimate of $B_x$

In order to estimate the magnitude of the radio frequency (RF) transverse magnetic field  $B_x$  produced by the microwire used in our optical experiments, we performed nutation measurements using a similar microwire in a magnetic resonance force microscope (MRFM). Using the method described in Poggio *et al.*<sup>5</sup>, we measure the transverse field experienced by an ensemble of  $\sim 10^6$   $^{115}\text{In}$  spins 350 nm from the microwire. These spins are contained within an InP nanowire in a 6 T magnetic field at a temperature of 1 K. The experiment is carried out with an adiabatic rapid passage pulse protocol similar to the one used in the optical experiment at a carrier frequency of 57.25 MHz. To contact the microwire similar lengths of exactly the same type of coaxial lines and twisted pairs are used. Identical hardware is used to generate, split and filter the chirped pulses.

As shown in Fig. A.6, the microwire in the MRFM generates 50 mT of transverse magnetic field (25 mT in the rotating frame). The amplitude of the drive voltage measured across  $50 \Omega$  at the same point at the top of the cryostat for the MRFM and the optical experiments is  $8.5 \text{ V}_{\text{p-to-p}}$  and  $10 \text{ V}_{\text{p-to-p}}$ , respectively. Also, the geometry of the microwire in the MRFM differs from that used in the optical experiment (Fig. A.6). Finally, the spin ensemble in the MRFM is located 350 nm above the microwire, while the QD in the optical experiment lies  $1.17 \mu\text{m}$  below the microwire. By taking these differences into account, we use the magnitude of the transverse field measured by MRFM to estimate the field produced at the QD location in the optical experiment. In particular, these differences result in different currents passing through the two microwires



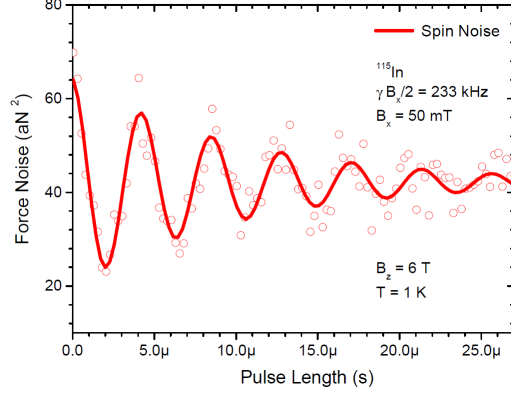
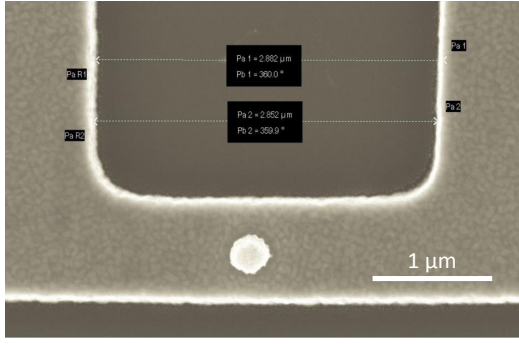


Fig. A.6. **Nutation measurement for  $^{115}\text{In}$  at  $T = 1\text{ K}$ .** (a) SEM micrograph of the 260 nm thick Au microwire with integrated FeCo tip used in the MRFM measurements. The microwire is 900 nm wide and 2.87  $\mu\text{m}$  long. The structure is patterned on a Si chip. (b) Resonant force noise from  $^{115}\text{In}$  spins (points) is measured as a function of pulse length according to the protocol described by Poggio *et al.*<sup>5</sup>. A frequency of 233 kHz is obtained from a decaying sinusoidal fit (solid line) to the Rabi oscillations, resulting in  $B_x = 50\text{ mT}$ .

and in different distances between the detection volume and the respective RF current. By approximating the two microwires as infinite wires, which produce a field decreasing inversely with the distance, we calculate the transverse field at the QD position. For a drive of  $10V_{\text{p-to-p}}$  across  $50\ \Omega$ , the QD microwire should generate  $B_x = 5\text{ mT}$ . The value  $B_x = 3.8\text{ mT}$  extracted from fits to our data is close to this estimation.

## A.3 Theory

### A.3.1 Concepts

#### Hamiltonian of a single spin $I$

During the manipulation step of our experiment, the evolution of a spin  $I$  can be described by the time-dependent Hamiltonian

$$H(t) = H_Z + H_Q + H_{RF}(t). \quad (\text{A.1})$$

$H_Z$  is the Zeeman energy,  $H_Q$  describes the interactions between the nuclear quadrupole moment and the electric field gradient (EFG) for a spin  $I > \frac{1}{2}$  in a non-cubic lattice, and  $H_{RF}(t)$  corresponds to the coupling to the transverse radio-frequency field. This is most conveniently expressed in the frame rotating at the Larmor frequency  $\nu_L = \gamma B_z$ ,

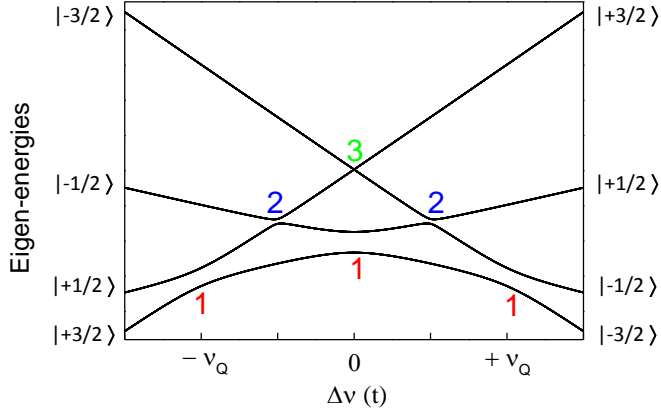


Fig. A.7. **Energy level diagram for a spin  $I = \frac{3}{2}$  in the rotating frame.** The calculation is carried out with  $\frac{\nu_{RF}}{\nu_Q} = 0.15$ . The eigenstates are labelled with the diabatic quantum number  $m$  in the limit of large detunings. The numbers in colour represent the order  $\Delta m$  associated with each transition.

where  $\gamma$  is the gyromagnetic ratio of the nuclei and  $B_z$  the magnetic field applied along the  $z$ -direction (here the quantization axis). Using the rotating wave approximation to neglect fast oscillating terms<sup>6</sup> and assuming cylindrical symmetry of the EFG,  $H(t)$  reduces to

$$H^{(1)}(t) = h\Delta\nu(t)I_z + \frac{h\nu_Q}{6} [3I_z^2 - I(I+1)] + \frac{h\nu_{RF}}{2} I_x \quad (\text{A.2})$$

where  $\Delta\nu(t)$  is the time-dependent detuning between the radio frequency and the Larmor frequency,  $\nu_{RF} = \gamma B_x$  the amplitude of the RF field and  $\nu_Q$  the quadrupole frequency.  $\nu_Q$  describes the strength of the quadrupole interaction and depends on the nuclear quadrupole moment  $Q$  and on the EFG  $V_{zz'}$ , along the symmetry axis  $z'$ . Writing  $\theta$  as the angle between  $z$  and  $z'$ , we find

$$\nu_Q = \frac{3eQV_{zz'}}{4hI(2I-1)} [3\cos^2\theta - 1]. \quad (\text{A.3})$$

We are interested in the eigenvalues of the problem for  $I > \frac{1}{2}$ . As an example, Fig. A.7 shows the energy eigenstates for a spin  $I = \frac{3}{2}$  as a function of the detuning  $\Delta\nu(t)$ . Six different transitions can be observed: three first-quantum transitions (QTs), often referred to as the central peak and its two satellites, two second-QTs and one third-QT, corresponding to a change in angular momentum of  $|\Delta m| = 1, 2$  and  $3$ , respectively. We note that each transition is well isolated, a consequence of  $\nu_Q \gg \nu_{RF}$ . A clear hierarchy of avoided crossings can be observed: the lower the order of the QT, the more pronounced the splitting. This result can be derived analytically in the limit where  $\nu_Q \gg \nu_{RF}$  using

an effective pseudo-spin 1/2 approach<sup>7,8</sup>, which yields the following expression for the coupling strengths

$$\nu_{\text{eff}}(\Delta m) = k(m_i, m_j) \nu_{RF} \left( \frac{\nu_{RF}}{\nu_Q} \right)^{|\Delta m|-1} \quad (\text{A.4})$$

where  $k(m_i, m_j)$  is a scaling factor associated with the  $|m_i\rangle \rightarrow |m_j\rangle$  transition. As an example we show, in Table A.1, the scaling factors associated with the  $\frac{3}{2}$ -spin. Since  $\nu_Q \gg \nu_{RF}$  it is clear from Eq. A.4 that  $\nu_{\text{eff}}(\Delta m = 1) \gg \nu_{\text{eff}}(\Delta m = 2) \gg \nu_{\text{eff}}(\Delta m = 3)$ . Remarkably,  $\nu_{\text{eff}}(\Delta m = 1)$  does *not* depend on the quadrupole frequency to first order.

| $m_i / m_j$ | 3/2        | 1/2        | -1/2          | -3/2          |
|-------------|------------|------------|---------------|---------------|
| 3/2         | –          | $\sqrt{3}$ | $\frac{7}{2}$ | $\frac{3}{2}$ |
| 1/2         | $\sqrt{3}$ | –          | 2             | $\frac{7}{2}$ |

Table A.1. **Effective RF field scaling factors  $k(m_i, m_j)$  for the first and multiple-quantum transitions of  $I = \frac{3}{2}$ .**<sup>8</sup>.

### Adiabaticity criteria for a quadrupolar nucleus

To quantify the degree of adiabaticity of the manipulation, we assign a probability to each type of transition according to the Landau-Zener model (Eq. 2.2 of chapter 2)

$$P_{LZ}(\Delta m) = \exp \left( -\pi^2 \frac{\nu_{\text{eff}}^2(\Delta m)}{\alpha \Delta m} \right). \quad (\text{A.5})$$

Note that, for higher-order transitions, the sweep rate  $\alpha$  is replaced by an effective sweep rate  $\alpha \Delta m$ , which accounts for the magnified detuning rate (steepness of the level crossings in Fig. A.7)<sup>9</sup>.  $P_{LZ}$  corresponds to the probability that the system “tunnels” through the avoided crossing and stays on the same *adiabatic* state. The condition for adiabatic passage is thus  $P_{LZ} \ll 1$ , which translates into low  $\alpha$  and/or large  $\nu_{\text{eff}}$ . Generally speaking, from Eqs. A.4 and A.5 it is clear that nuclei experiencing large quadrupole interactions are harder to manipulate. However, to first order, adiabatic passage is independent of the quadrupole interaction if it is possible to prepare the spins in their ground state, since the first QTs do not depend on  $\nu_Q$  (see also end of the section).

In order to study the dynamics of the Landau-Zener problem in more detail we solve

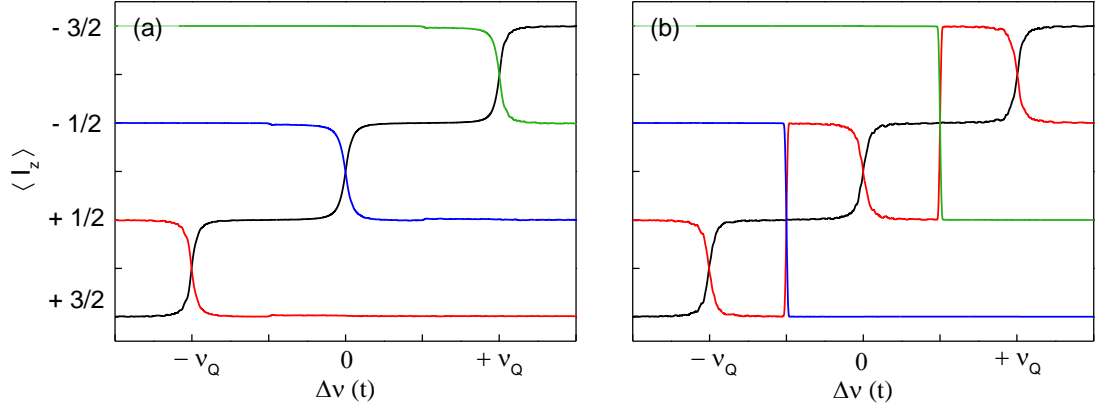


Fig. A.8. **Evolution of the average nuclear spin projection  $\langle I_z \rangle$  for a linear RF sweep.** The RF field is swept from negative to positive detunings (left to right). In (a),  $P_{LZ}(\Delta m = 1) = 1.4\%$  and  $P_{LZ}(\Delta m = 2) = P_{LZ}(\Delta m = 3) = 100\%$ . In (b),  $P_{LZ}(\Delta m = 1) = 0$ ,  $P_{LZ}(\Delta m = 2) = 0.5\%$  and  $P_{LZ}(\Delta m = 3) = 99.8\%$ . For both cases four different initial conditions are considered, corresponding to the pure states of the system. Black:  $|\psi(t=0)\rangle = |+\frac{3}{2}\rangle$ , red:  $|\psi(t=0)\rangle = |+\frac{1}{2}\rangle$ , blue:  $|\psi(t=0)\rangle = |-\frac{1}{2}\rangle$  and green:  $|\psi(t=0)\rangle = |-\frac{3}{2}\rangle$

numerically the time-dependent von Neumann equation. Neglecting dissipation operators, the time-evolution of the density matrix  $\rho(t)$  obeys

$$i\hbar\dot{\rho}(t) = [H(t), \rho(t)]. \quad (\text{A.6})$$

In the following, we return to the example of a spin  $I = \frac{3}{2}$  to illustrate some concepts of adiabatic passage for a quadrupolar nucleus. We first focus on the evolution of the average spin projection  $\langle I_z(t) \rangle = \text{Tr}[I_z \rho(t)]$  as we proceed with a linear sweep from  $\Delta\nu(t=0) = -\nu_0$  to  $\Delta\nu(t=\tau) = +\nu_0$ . Fig. A.8 shows the result for four different initial conditions corresponding to the pure states of the system. In (a), the adiabatic conditions are fulfilled for the first QTs only. This is evidenced by the exchange of population at the transitions associated with the central peak ( $\Delta\nu = 0$ ) and its two satellites ( $\Delta\nu = \pm\nu_Q$ ). On the contrary, nothing happens at the second QTs ( $\Delta\nu = \pm\frac{\nu_Q}{2}$ ). In (b), the “opening” of the second QTs is evidenced by two additional steps at  $\Delta\nu = \pm\frac{\nu_Q}{2}$ . As a consequence of the smaller coupling strength, these transitions are sharper compared to the ones observed for the first QTs.

In the next step we retain only the polarization  $\langle I_z(\tau) \rangle$  after the sweep is complete and study the effect of a decreasing sweep rate. We first focus on the same set of initial

conditions as in Fig. A.9. At high sweep rates (here,  $\alpha \geq 10^5$  GHz/s) the passage is sudden,  $P_{LZ} \simeq 1$ , and the polarization remains unchanged after the sweep. For lower values of  $\alpha$ , the polarization is modified by the RF pulse. We identify the three thresholds corresponding to fulfilling the adiabatic conditions for the first, second and third QT, respectively. In Fig. A.9(b), we turn to a more realistic thermal distribution at  $t = 0$ . The evolution of  $\langle I_z(\tau) \rangle$  shows a step-like behaviour, with the steps corresponding to the  $\Delta m = 1$ ,  $\Delta m = 2$  and  $\Delta m = 3$  thresholds.

Several comments should be made. First, if  $\frac{\nu_{RF}}{\nu_Q} \sim 1$ , the different transitions identified in Fig. A.7 and Fig. A.8 are no longer isolated one from the other, and the step-like behaviour of Fig. A.9 vanishes. Second, the efficiency of the manipulation for a given sweep rate is not only related to the quadrupole field but also to the initial polarization. To clarify this point, let us consider an initial thermal distribution described by a temperature  $T$ . In the high temperature limit ( $k_B T \gg h\nu_L$ , with  $h\nu_L$  the Zeeman energy), it is possible to show analytically that the manipulation efficiencies associated with the successive opening of the first, second and third QTs are 60%, 90%, and 100%, respectively. Conversely, in the limit where  $k_B T \ll h\nu_L$ , complete inversion is achieved as soon as the adiabatic condition is satisfied for the first QT, which does not (to first order) depend on  $\nu_Q$ .

### A.3.2 Quantitative analysis

The nuclear spin ensemble in an  $\text{In}_x\text{Ga}_{1-x}\text{As}$  QD is highly inhomogeneous. The first obvious reason is the presence of various isotopes, mainly  $^{75}\text{As}$ ,  $^{115}\text{In}$ ,  $^{69}\text{Ga}$  and  $^{71}\text{Ga}$  (see Table A.2). A second reason, which is intrinsic to self-assembled QDs, is the strain which is not homogeneously distributed over the QD<sup>10</sup>. This results in a position dependent electric-field gradient, and thus a distribution of quadrupole frequencies over the spin ensemble. This inhomogeneity, associated with the exact chemical composition of the QD, influences the overall degree of adiabaticity that can be reached for a given experiment. In the following we derive the effective nuclear spin temperature following optical polarization, a quantitative value for the chemical composition, as well as the isotope dependent quadrupole frequency distribution in the QD.

#### Chemical composition and nuclear spin temperature

Since the orbital part of the hole wave function is predominantly p-like, the contact interaction of the nuclear spin ensemble with the hole spin can be neglected. Initialization

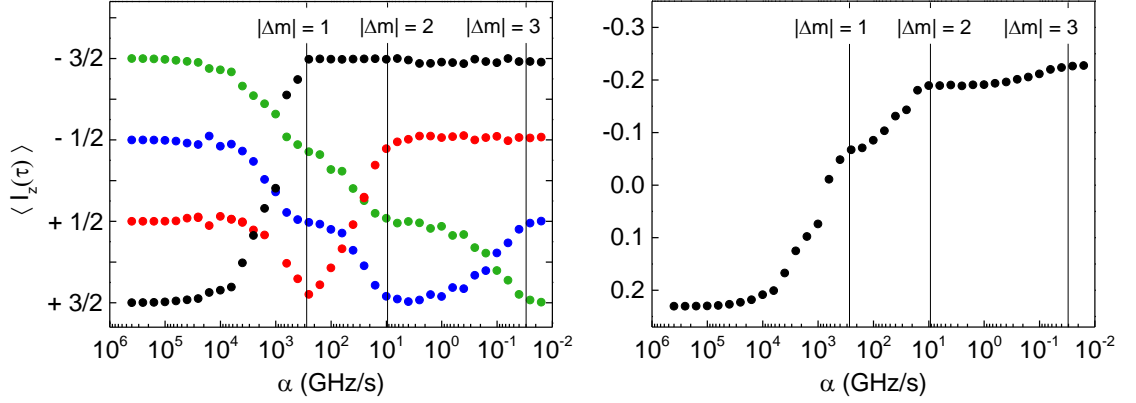


Fig. A.9. **Average spin projection  $\langle I_z \rangle$  as a function of the sweep rate.** The simulations are carried out on  $^{71}\text{Ga}$  with  $B_z = 6\text{ T}$ ,  $B_x = 16\text{ mT}$  and  $\nu_Q = 1\text{ MHz}$  for different initial polarizations. In (a), we consider the same pure states as in Fig. A.8. For  $\alpha \geq 10^5\text{ GHz/s}$  the passage is sudden. After the first threshold, the adiabatic condition is satisfied for the first QTs ( $|\Delta m| = 1$ ). We observe, for example,  $|+\frac{3}{2}\rangle \rightarrow |-\frac{3}{2}\rangle$  and  $|-\frac{3}{2}\rangle \rightarrow |+\frac{1}{2}\rangle$  as expected from the energy level diagram in Fig. A.7. After the second (third) threshold, the adiabatic condition is also satisfied for  $|\Delta m| = 2$  ( $|\Delta m| = 3$ ). This has no impact if the population was initially all in the  $|+\frac{3}{2}\rangle$  state (black line), but now  $|-\frac{3}{2}\rangle \rightarrow |+\frac{1}{2}\rangle$  ( $|-\frac{3}{2}\rangle \rightarrow |+\frac{3}{2}\rangle$ , green line). In (b) we start with a thermal distribution with  $T = 20\text{ mK}$ . The vertical lines correspond to  $P_{LZ} = 1\%$  for the first, second and third quantum transitions.

and read-out thus depends primarily on the contact hyperfine interaction between the nuclear spin ensemble and the electron spin. The effect of the nuclear spin ensemble on the electron spin is described by an effective magnetic field  $B_N$ , the Overhauser field, which shifts the energy levels of the electron spin states. This Overhauser shift is given by  $\text{OHS} = g_e \mu_B B_N S_z$ , where  $g_e$  is the effective electron g-factor,  $\mu_B$  the Bohr magneton and  $S_z$  the electron spin quantum number along the  $z$ -direction. For a spin ensemble of isotope  $j$  with average polarization  $\langle I_{z,j} \rangle$ ,  $\text{OHS} = \sum_j A \langle I_{z,j} \rangle S_z$ , where  $A$  is the hyperfine coupling constant<sup>11,12</sup>. The experiments presented in chapter 2 are all carried out on the blue transition such that  $S_z = -\frac{1}{2}$ . Each nuclear spin interacts with the same pumped electron spin so that it is safe to assume that the initial populations of the nuclear spin levels for each isotope can be described with a temperature. It is not necessarily the case that each isotope can be described with the same temperature. For simplicity, we describe all isotopes with the same nuclear spin temperature and we return to this assumption in section A.3.4. We now show that measurements of OHS, the initial Overhauser shift, and  $\Delta_{\text{OHS}}(\Delta m = 1)$ , the change in Overhauser shift measured

|                   | $I$ | $C$ [%] | $\gamma$ [MHz/T] | $A$ [μeV] | $Q$ [mb] |
|-------------------|-----|---------|------------------|-----------|----------|
| $^{69}\text{Ga}$  | 3/2 | 60.18   | 10.219           | 74        | 171      |
| $^{71}\text{Ga}$  | 3/2 | 39.89   | 12.984           | 96        | 107      |
| $^{75}\text{As}$  | 3/2 | 100     | 7.219            | 86        | 314      |
| $^{113}\text{In}$ | 9/2 | 4.29    | 9.310            | 110       | 759      |
| $^{115}\text{In}$ | 9/2 | 95.71   | 9.330            | 110       | 770      |

Table A.2. **Relevant parameters of the QD main isotopes:** Nuclear spin number  $I$ , natural abundance  $C$ , gyromagnetic ratio  $\gamma$ , contact hyperfine coupling strength  $A$  and quadrupole moments  $Q$  for the relevant isotopes. Since  $^{113}\text{In}$  abundance is only 4.3% and its difference in  $\gamma$  compared to  $^{115}\text{In}$  is beyond the resolution of our experiment we neglect this isotope in our analysis. Data taken from<sup>11</sup>.

at the first plateau (Fig. 2.6 of chapter 2), we can determine the In composition  $x$  and the initial nuclear spin temperature  $T$ .

Using Boltzmann statistics the occupation probability of the  $m^{\text{th}}$  level for isotope  $j$  is

$$p_{j,m} = \frac{1}{Z_j} \exp\left(-\frac{E_{j,m}}{k_B T}\right) \quad (\text{A.7})$$

where  $E_{j,m} = -mh\gamma_j B_z$  is the Zeeman energy of the  $m^{\text{th}}$  level\*,  $Z_j = \sum_m \exp(-E_{j,m}/k_B T)$  is the partition function,  $k_B$  is the Boltzmann constant and  $m = \frac{3}{2}, \frac{1}{2}, -\frac{1}{2}, -\frac{3}{2}$  for  $I = \frac{3}{2}$  spins ( $m = \frac{9}{2}, \frac{7}{2}, \dots, -\frac{9}{2}$ , for  $I = \frac{9}{2}$  spins). Thus the average nuclear spin polarization for  $j^{\text{th}}$  isotope amounts to

$$\langle I_{z,j} \rangle = \sum_m p_{j,m} m. \quad (\text{A.8})$$

By weighting each  $\langle I_{z,j} \rangle$  with its corresponding coupling coefficient  $A_j$  (see Table A.2) and relative concentration  $c_j$  the initial Overhauser shift for each isotope is

$$\text{OHS}_j = -\frac{1}{2} c_j A_j \langle I_{z,j}^{\text{initial}} \rangle. \quad (\text{A.9})$$

Since Ga substitutes to In, the  $^{75}\text{As}$  concentration is known and equals to 50%, whereas the other concentrations depends on  $x$ .

---

\*Corrections to the level spacings due to first order quadrupolar effects (Eq. A.1) were included in a mean approach by using the average quadrupole frequency determined in the below (subsection Quadrupolar field) for each isotope. Note that, given  $\langle \nu_Q \rangle \ll \gamma B_z$ , the effect on  $T$  and  $x$  are small and fall within the error bars.

An adiabatic sweep leads to a change in nuclear spin polarization

$$\Delta I_{z,j} = \langle I_{z,j}^{final} \rangle - \langle I_{z,j}^{initial} \rangle. \quad (\text{A.10})$$

Thus the related change in Overhauser shift is

$$\Delta_{\text{OHS}}^j = \frac{1}{2} c_j A_j \Delta I_{z,j}. \quad (\text{A.11})$$

For  $\frac{3}{2}$ -spins, assuming adiabatic conditions for the first order QTs only, one can determine the final nuclear spin polarization (see energy level diagram of Fig. A.7):

$$\langle I_{z,j}^{final} \rangle (\Delta m = 1) = +\frac{3}{2} p_{j,\frac{1}{2}} + \frac{1}{2} p_{j,-\frac{1}{2}} - \frac{1}{2} p_{j,-\frac{3}{2}} - \frac{3}{2} p_{j,\frac{3}{2}} \quad (\text{A.12})$$

The same is done analogously for the  $\frac{9}{2}$ -spins of indium.

We are finally left with the following set of equations

$$\text{OHS} = \sum_j \text{OHS}_j \quad (\text{A.13})$$

$$\Delta_{\text{OHS}}(\Delta m = 1) = \sum_j \Delta_{\text{OHS}}^j(\Delta m = 1) \quad (\text{A.14})$$

where  $T$  and  $x$  as the only unknowns. Solving the system with inputs from the experiment  $\text{OHS} = (27.0 \pm 0.85) \mu\text{eV}$  and  $\Delta_{\text{OHS}} = (28.8 \pm 0.85) \mu\text{eV}$ , we obtain an initial temperature  $T = 8.2 \pm 0.8 \text{ mK}$  and an In concentration for this specific QD of  $x = 0.202 \pm 0.057$ .

### Quadrupolar field

In section A.3.1 we showed how we use the von Neumann equation to simulate the evolution of the (projected) nuclear spin polarization with a linear sweep of the radio-frequency. Now assuming an initial spin temperature of 8.2 mK, we are in a position to model the NMR spectra measured in our experiment.

We first plot the expected change of polarization in the case of a single  $^{71}\text{Ga}$  spin for different quadrupole frequencies (Fig. A.10). The simulations show clear steps associated with the transfer of population at the first and second quantum transitions. As expected, the total  $\langle \Delta I_z \rangle$  reduces as  $\nu_Q$  increases, a consequence of the smaller  $\nu_{\text{eff}}$  for the high order QTs. In order to account for the inhomogeneity in the sample, we then average



this behaviour over a distribution of quadrupole frequency ( $\nu_Q = 0 \rightarrow \nu_Q^{max}$ ) using (truncated) Gaussian distributions of the form

$$p(\nu_Q) = \lambda \exp \left[ -\frac{(\nu_Q - \nu_Q^0)^2}{2\sigma_Q^2} \right] \quad \text{with } \nu_Q > 0, \quad (\text{A.15})$$

where  $\lambda$  normalizes the distribution,  $\int_0^{\nu_Q^{max}} p(\nu_Q) d\nu_Q = 1$ . The result is shown in Fig. A.10(b). We note in particular that the steps associated with the satellite peaks are smeared out as the distribution spreads. Ultimately, the NMR spectrum of the  $\frac{3}{2}$ -spin reduces to one step at the position of the central frequency surrounded by a steady (almost linear) increase due to the satellite transitions.

For In, the situation is similar (Fig. A.11(b)). After the averaging however, no step remains, a consequence of the large number of transitions.

We finally compute an average quadrupole frequency  $\langle \nu_Q \rangle = \int_0^{\nu_Q^{max}} p(\nu_Q) \nu_Q d\nu_Q$ , which slightly differs from  $\nu_Q^0$  if  $p(\nu_Q)$  is truncated.

In order to describe the experimental data, we derive such spectra using the experimental sweep rate  $\alpha = 0.09$  GHz/s for  $\frac{3}{2}$ -spins, and a slightly larger value  $\alpha = 0.25$  GHz/s for  $\frac{9}{2}$ -spins\*. Weighting each isotope's contribution with its concentration determined in section A.3.2, and multiplying by the corresponding coupling coefficient (Table A.2), we obtain the theoretical spectra shown in Fig. 2.7 of chapter 2. In the case of  $^{75}\text{As}$  and  $^{71}\text{Ga}$ , the resonances are well isolated and it is straightforward to adjust  $p(\nu_Q)$  to fit the data. On the other hand, for  $^{115}\text{In}$  and  $^{69}\text{Ga}$ , the spectra overlap. Assuming a homogeneous distribution of both Ga isotopes within the QD (and thus similar electric field gradient distributions), we can however predict the  $^{69}\text{Ga}$  spectrum simply by the ratio of both isotope's nuclear quadrupole moments using Eq. A.3 (see also Table A.2). The remaining signal is then due to In. With this procedure we can thus determine an approximate distribution of quadrupole frequencies for all the main isotopes, see Table A.3 and inset of Fig. 2.7 of chapter 2.

### A.3.3 Discussion and conclusions

Now using the temperature, In concentration and the average quadrupole frequencies for each isotopes determined in previous sections, we can simulate the expected change in the average nuclear spin polarization as a function  $\alpha$  (Fig. 2.6 of chapter 2). With  $B_x = 3.8$  mT, the calculations show remarkable agreement with the experimental data.

---

\*By doing so we significantly speed up calculations without modifying the expected result since both rates belong to the second plateau for In (Fig. 2.6 of chapter 2)

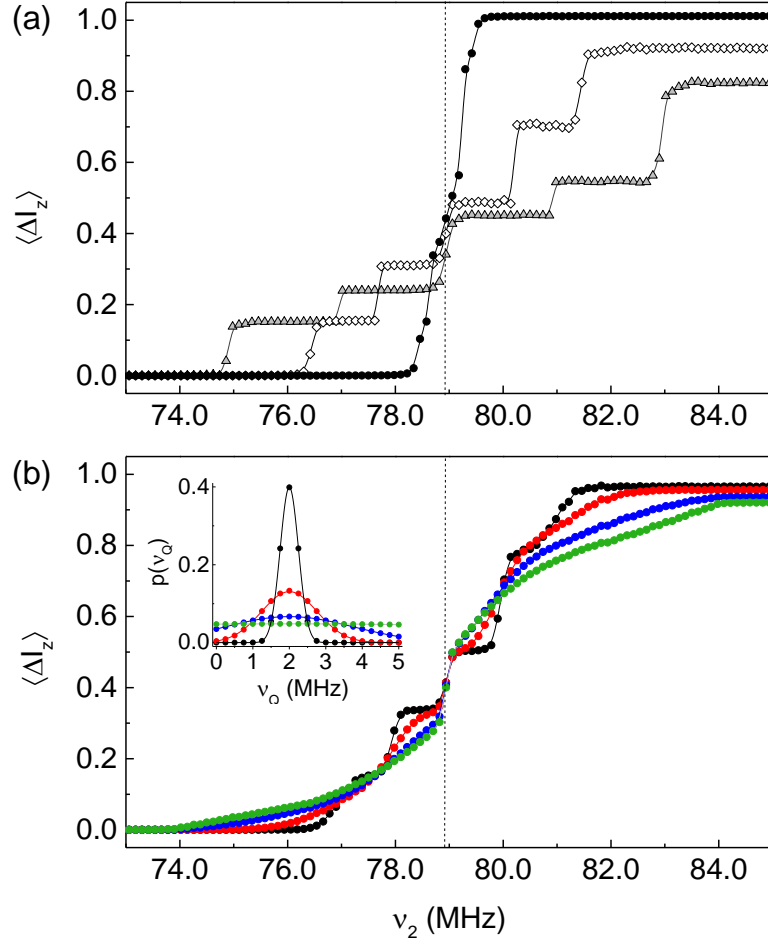


Fig. A.10. NMR spectrum of  $\frac{3}{2}$ -spins. (a) Change in polarization for a single  $^{71}\text{Ga}$  spin. The sweep rate is set to  $\alpha = 0.04$  GHz/s (first and second QTs opened). Three different quadrupole frequencies are shown: black circles  $\nu_Q = 0.5$  MHz, open diamonds  $\nu_Q = 2.5$  MHz and gray triangles  $\nu_Q = 4.5$  MHz. (b) Change in polarization for an inhomogeneous ensemble of  $^{71}\text{Ga}$  spins. In black, red and blue, the distribution of quadrupole frequencies are Gaussian functions centered around  $\nu_Q^0 = 2$  MHz. In green we consider a flat distribution. Insets: the quadrupole frequency distributions. For all calculations,  $B_z = 6$  T,  $B_x = 3.8$  mT and the initial temperature is set to  $T = 8.2$  mK.

In particular the plateau associated with the first QTs is reproduced, a signature of a large quadrupole field for all isotopes. One can note that the first QTs are not reached at the same  $\alpha$  for all isotopes. This is due to different gyromagnetic ratios (see Table A.2) and, in the case of In, to the different spin number. As can be seen from the isotope selective  $\alpha$ -dependency, the second step-like feature at low  $\alpha$  arises due to In spins reaching the plateau associated with the second QTs before the  $\frac{3}{2}$ -spins. The large

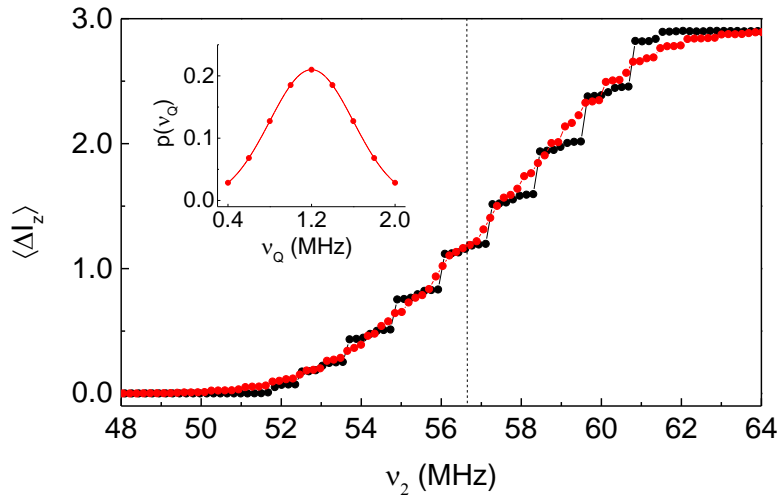


Fig. A.11. **NMR spectrum of  $\frac{9}{2}$ -spins.** Change in polarization for In, with  $\alpha = 1$  GHz/s. In black, the signal associated with a single spin with  $\nu_Q = 1.2$  MHz; in red, an inhomogeneous ensemble with a Gaussian distribution of quadrupole frequencies centred around  $\nu_Q^0 = 1.2$  MHz (see inset).

|                               | $^{75}\text{As}$ | $^{115}\text{In}$ | $^{69}\text{Ga}$ | $^{71}\text{Ga}$ |
|-------------------------------|------------------|-------------------|------------------|------------------|
| $\nu_Q^0$ [MHz]               | 0                | 1.5               | 2.9              | 1.8              |
| $\sigma_Q$ [MHz]              | 4.0              | 0.4               | 1.6              | 1.6              |
| $\langle \nu_Q \rangle$ [MHz] | 3.0              | 1.5               | 3.1              | 2.1              |

Table A.3. Parameters of the (truncated) Gaussian distributions used in the description of the experimental data (Fig. 2.6 of chapter 2).  $\nu_Q^0$  is the central frequency, corresponding to the highest density,  $\sigma_Q$  is the width of the distribution and  $\langle \nu_Q \rangle$  is the average quadrupole frequency, which differs from  $\nu_Q^0$  when the distribution is truncated.

contribution of the In spins along with the small dispersion in In quadrupole frequencies explain the observed second step-like feature.

Finally, we gather all the results obtained from our calculations and compare them with the experimental data. The results are shown in Fig. A.12 and Table A.4 and commented hereafter:

*Initial polarization:* The initial polarization for each isotope  $\langle I_{z,j} \rangle / I_{z,j}^{max}$  is determined solely by  $T$ . Due to the different gyromagnetic ratios and the much higher spin number of In, the polarization is not equally distributed among the different isotopes (Table A.4). For example, the initial polarization of As is only 21%, whereas the initial polarization

of In reaches 50%. Weighting each isotope with its concentration yields a value of 32% for the initial polarization of the ensemble. Finally, using the coupling coefficients  $A_j$  from Table A.2 and our measured value  $g_e = -0.71 \pm 0.05$  of the electron g-factor, we calculate the Overhauser field corresponding to 32% polarization,  $B_N = 2.0$  T.

*Efficiency of the nuclear spin manipulation:* The inversion efficiency for each isotope is defined as  $\Delta I_{z,j}/(2I_{z,j}^{initial}) = \Delta_{\text{OHS}}^j/(2\text{OHS}_j)$ . The efficiency depends on three parameters, first the spin quantum number  $I$ , second the initial polarization, and third the quadrupole frequency.  $^{75}\text{As}$  has the lowest initial polarization, a broad quadrupole frequency distribution and a large  $\langle\nu_Q\rangle$ , thus the inversion efficiency (75%) is lower than that for  $^{71}\text{Ga}$  (94%), which has a higher initial polarization and a smaller  $\langle\nu_Q\rangle$  with a narrower distribution. Conversely, In has a much more complex level structure and despite the high initial polarization the inversion efficiency is only 64%. By weighting the efficiency for each isotope with its concentration we compute the efficiency for the whole ensemble, which is 72%.

*Sensitivity of the measurement:* The sensitivity to the change in Overhauser shift is obtained from the statistical distribution of the experimental results. Averaging over more than 20 measurements, we obtain a standard deviation of 0.85  $\mu\text{eV}$  for  $\Delta_{\text{OHS}}$ . Using the value  $\text{OHS}^{\text{max}} = 81.8 \mu\text{eV}$  for the maximum Overhauser shift and  $10^5$  nuclei<sup>12</sup>, we conclude that we are sensitive to the Overhauser field generated by the full polarization of  $\sim 1,000$  nuclei. The errors in  $x$  and  $T$  correspond to the statistical fluctuations in the change of the plateau width. For all numbers deduced from the model the errors in the change of dragging plateau width were propagated to find the error in a particular quantity.

### A.3.4 Nuclear spin temperature

The analysis so far has assumed an isotope-independent initial nuclear spin temperature. An alternative assumption is that the polarization for all spin- $\frac{3}{2}$  nuclei is the same such that there is a spread of temperatures in accord with the spread in gyromagnetic ratios. This second Ansatz would hold if the only significant interaction is the first-order contact hyperfine interaction<sup>13</sup>. We have attempted to describe the experimental data also with this assumption, explicitly that the ratio  $\beta = (E_{j,m+1} - E_{j,m})/k_B T$  (ratio Zeeman energy to thermal energy) is the same for all isotopes. We find with this approach that  $\beta = 0.302 \pm 0.033$ ,  $x = 0.221 \pm 0.067$  with temperatures  $^{75}\text{As}$ :  $(6.9 \pm 0.8)$  mK; In:  $(8.9 \pm 1.0)$  mK;  $^{69}\text{Ga}$ :  $(9.7 \pm 1.1)$  mK;  $^{71}\text{Ga}$ :  $(12.4 \pm 1.4)$  mK. Some important comments are in order.

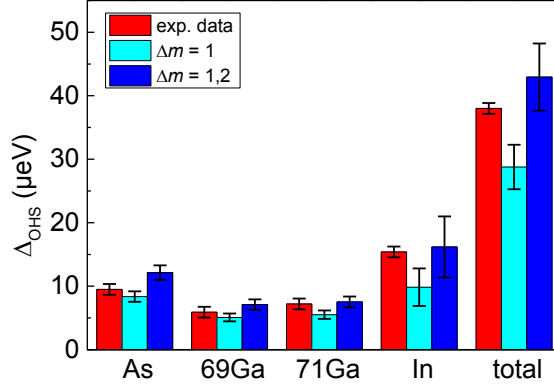


Fig. A.12. **Comparison of the measured change in Overhauser shift  $\Delta_{\text{OHS}}$  with the single spin model at first and second quantum transitions.** The results indicate that, for the slowest rate, we achieve inversion at the second QT for In and  $^{71}\text{Ga}$ . The second QT is however not yet opened for As and  $^{69}\text{Ga}$ . Input parameters to the model are  $T = 8.2 \pm 0.8 \text{ mK}$  and  $x = 0.20 \pm 0.06$ .

| -   | $^{75}\text{As}$ | $^{69}\text{Ga}$ | $^{71}\text{Ga}$ | $^{115}\text{In}$ | total           |
|---|------------------|------------------|------------------|-------------------|-----------------|
| OHS [ $\mu\text{eV}$ ]                                    | $-6.6 \pm 0.6$   | $-3.80 \pm 0.4$  | $-4.0 \pm 0.4$   | $-12.6 \pm 3.6$   | $-27.0 \pm 0.9$ |
| Initial Polarization [%]                                  | $21 \pm 3$       | $29 \pm 3$       | $36 \pm 3$       | $50 \pm 3$        | $32 \pm 1$      |
| $\Delta_{\text{OHS}}(\Delta m = 1)$ [ $\mu\text{eV}$ ]    | $8.4 \pm 0.8$    | $5.1 \pm 0.6$    | $5.5 \pm 0.7$    | $9.8 \pm 4.8$     | $28.8 \pm 0.9$  |
| Efficiency ( $\Delta m = 1$ ) [%]                         | $63.0 \pm 0.5$   | $66.3 \pm 0.7$   | $68.8 \pm 0.9$   | $39.2 \pm 1.3$    | $55.0 \pm 2.3$  |
| $\Delta_{\text{OHS}}(\Delta m = 1,2)$ [ $\mu\text{eV}$ ]  | $12.1 \pm 1.1$   | $7.1 \pm 0.8$    | $7.5 \pm 0.9$    | $16.2 \pm 4.8$    | $42.9 \pm 5.3$  |
| Efficiency ( $\Delta m = 1,2$ ) [%]                       | $91.6 \pm 0.2$   | $92.9 \pm 0.3$   | $93.9 \pm 0.3$   | $64.5 \pm 1.5$    | $81.3 \pm 2.4$  |
| $\Delta_{\text{OHS}}(\text{measured})$ [ $\mu\text{eV}$ ] | $9.5 \pm 0.9$    | $5.9 \pm 0.9$    | $7.2 \pm 0.9$    | $15.4 \pm 0.9$    | $38 \pm 0.9$    |
| Efficiency (measured) [%]                                 | $75 \pm 9$       | $71 \pm 14$      | $94 \pm 15$      | $64 \pm 19$       | $72 \pm 10$     |

Table A.4. **Initial polarizations and inversion efficiencies for the main isotopes.** Values in red are obtained from Figs. 2.4, 2.6 and 2.7. Values in black are deduced from the single spin model described in section A.3.1 with  $T = 8.2 \text{ mK}$  and  $x = 20\%$ .

First, the indium concentration from the common polarization assumption is the same to within the random error as before (common temperature assumption). The random error is determined by noise in the initialization/read-out process. In other words, the random error is larger than any systematic error arising from assumptions on the temperature.

Secondly, the temperatures for  $^{75}\text{As}$ , In and  $^{69}\text{Ga}$  are also the same as before to within the random error: the common temperature and common polarization assumptions do

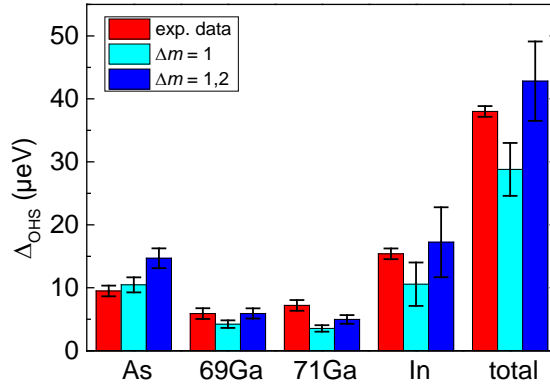


Fig. A.13. Comparison of the measured change in Overhauser shift  $\Delta_{\text{OHS}}$  with the single spin model at first and second quantum transitions with the common polarization assumption. As in Fig. A.12, for the slowest rate we achieve inversion at the first and second QT for In and  $^{71}\text{Ga}$  but inversion at the first QT only for As and  $^{69}\text{Ga}$ . Input parameters to the model are  $\beta = 0.302$  and  $x = 0.221$ . The calculations for  $^{71}\text{Ga}$  lie below the experimental result and in this respect, the common polarization assumption is inferior to the common temperature assumption of Fig. A.12.

not lead to significant differences. In principle, the experiment is capable of determining a nuclear spin temperature for each isotope separately. In practice, the present resolution is insufficient to reveal small differences.

Thirdly, the two assumptions, common temperature versus common polarization, lead to significantly different temperatures for  $^{71}\text{Ga}$ . A detailed comparison of the two models is shown in Fig. A.13 which plots  $\Delta_{\text{OHS}}$ , measured and calculated. The  $^{71}\text{Ga}$  result from the common polarization model is significantly too small, and this discrepancy cannot be resolved by including full inversion at the second quantum transition or by reducing the In concentration. The conclusion is that the common temperature assumption is more realistic than the common polarization assumption. This points to the presence of another interaction in the initialization process. A likely explanation is that the electron spin in the exciton provides a mechanism by which all the nuclear spins are coupled together, a second-order process, in the presence of spontaneous emission of the exciton which blurs energy conservation of the electron-nuclear interactions by up to 1  $\mu\text{eV}$ .

## References

1. Kuhlmann, A. V., Houel, J., Brunner, D., Ludwig, A., Reuter, D., Wieck, A. D., and Warburton, R. J. *Review of Scientific Instruments* **84**, 073905 (2013).
2. Latta, C., Hoegele, A., Zhao, Y., Vamivakas, A. N., Maletinsky, P., Kroner, M., Dreiser, J., Carusotto, I., Badolato, A., Schuh, D., Wegscheider, W., Atature, M., and Imamoglu, A. *Nature Physics* **5**, 758–763 (2009).
3. Högele, A., Kroner, M., Latta, C., Claassen, M., Carusotto, I., Bulutay, C., and Imamoglu, A. *Phys. Rev. Lett.* **108**, 197403 (2012).
4. Maletinsky, P., Badolato, A., and Imamoglu, A. *Phys. Rev. Lett.* **99**, 056804 (2007).
5. Poggio, M., Degen, C. L., Rettner, C., Mamin, H., and Rugar, D. *Applied Physics Letters* **90**, 263111 (2007).
6. Harris, R. and Roderick, W., editors. *NMR of Quadrupolar Nuclei in Solid Materials*. Wiley, (2012).
7. Vega, S. *The Journal of Chemical Physics* **68**(12), 5518–5527 (1978).
8. van Veenendaal, E., Meier, B. H., and Kentgens, A. P. M. *Molecular Physics* **93**, 195–213 (1998).
9. Haase, J., Conradi, M., Grey, C., and Vega, A. *Journal of Magnetic Resonance, Series A* **109**, 90–97 (1994).
10. Bulutay, C. *Phys. Rev. B* **85**, 115313 (2012).
11. Coish, W. A. and Baugh, J. *physica status solidi (b)* **246**, 2203–i;  $\frac{1}{2}$ 2215 (2009).
12. Kloeffel, C., Dalgarno, P. A., Urbaszek, B., Gerardot, B. D., Brunner, D., Petroff, P. M., Loss, D., and Warburton, R. J. *Phys. Rev. Lett.* **106**, 046802 (2011).
13. Abragam, A. *Principles of Nuclear Magnetism*. Oxford University Press, (2007).





# Appendix B

## Supplementary information to chapter 3

### B.1 Supporting experimental results

#### B.1.1 High accuracy measurement of the central NMR transition

Since the amplitude of Rabi oscillations decreases rapidly for excitation detuned more than the Rabi frequency it is crucial to determine the resonance frequency with high accuracy. Our method is to apply a frequency-swept pulse across all the side bands of a particular isotope with a Gaussian amplitude dip and vary the center frequency  $\nu_{\text{center}}$  of the Gaussian (Fig. B.1(a)). When  $\nu_{\text{center}}$  comes close central transition population exchange between the  $+1/2$  and  $-1/2$  state is interrupted and hence a dip in the NMR signal is observed (Fig. B.1(b)). A Gaussian fit determines the CT resonance with accuracy of  $\pm 3$  kHz for In ( $\pm 8$  kHz for As), considerably smaller than the Rabi frequency  $\nu_{\text{eff}} = 250$  kHz for In ( $\nu_{\text{eff}} = 65$  kHz for As) and the recently measured linewidth of the CT of 40 kHz for In at  $B_0 = 5.3 \text{ T}^1$  (30 kHz for As at  $B_0 = 8 \text{ T}^2$ ).

#### B.1.2 Gate switching bandwidth

In principle the characteristic time constant for the charge tunable device is given by  $1/RC$ , where  $R$  is the resistance of the back contact and  $C$  is the capacitance between top gate and back contact. To measure the bandwidth of the device we use the QD as a sensor: the DC gate voltage  $V_g$  is modulated with a square wave ( $V_{pp} = 200$  mV) and the resonant excitation wavelength is fixed. If we now scan the DC component  $V_g$  across the  $X^0$  resonance we observe two lines in the resonance fluorescence spectra separated by 200 mV (Fig. B.2). Increasing the modulation frequency, we find that the bandwidth of the device is around 100 kHz, i.e a switching time  $\sim 10 \mu\text{s}$ . This is one order of magnitude smaller than the 100  $\mu\text{s}$  delay we introduce between switching to a charging state and applying the RF pulse.

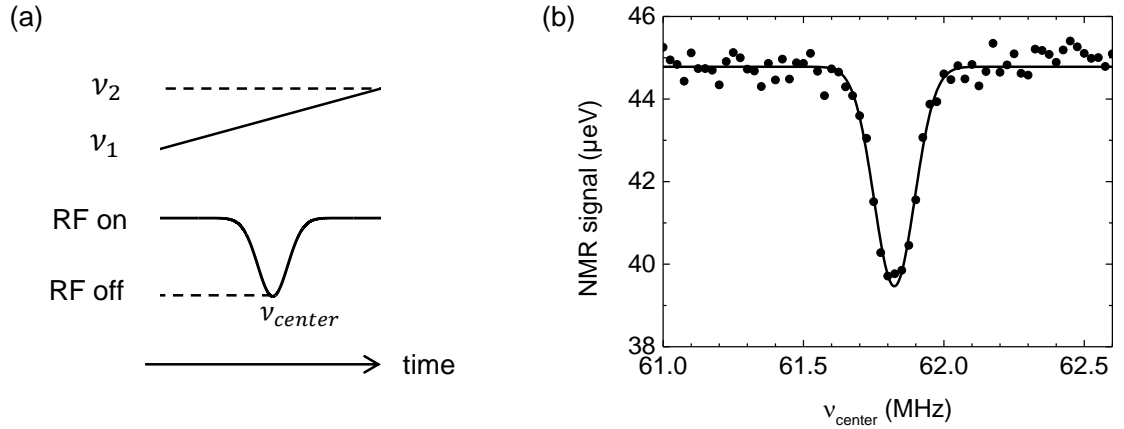


Fig. B.1. **Determining the resonance of the central transition.** (a) Sketch of a chirped pulse with a Gaussian amplitude modulation. (b) NMR signal vs center frequency  $\nu_{center}$  of the Gaussian amplitude modulation for Indium, where  $\nu_1 = 49$  MHz,  $\nu_2 = 74$  MHz,  $\alpha = 10$  GHz/s, FWHM of Gaussian = 0.3 MHz. The solid line is a Gaussian fit, where the error on the spectral position is less than 4 kHz.

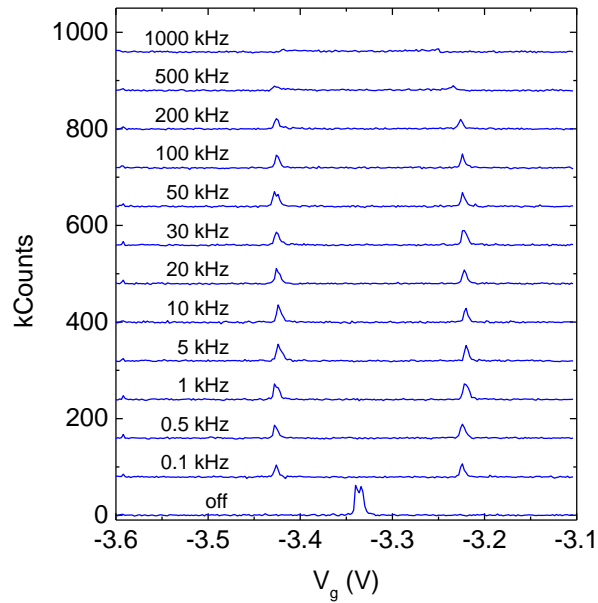


Fig. B.2. **Switching speed of the charge tunable device.** Resonance fluorescence spectra of the neutral exciton, while the gate voltage is modulated with a square wave ( $V_{pp} = 200$  mV) for different frequencies. The maximum bandwidth of the device is  $\sim 100$  kHz.

### B.1.3 g-factors and branching ratio

From PL measurements of the  $X^{1-}$  transition for different external magnetic fields (Fig. B.3(a),(c)) we can determine the electron g-factor  $g_e = -0.67 \pm 0.06$  and hole g-factor  $g_h = 1.59 \pm 0.06$  by comparing the resonance positions (Fig. B.3(b)). The corresponding gyromagnetic ratios are  $\gamma_e = -38.9 \pm 3.4 \mu\text{eV/T}$  and  $\gamma_h = -92.3 \pm 3.2 \mu\text{eV/T}$ .

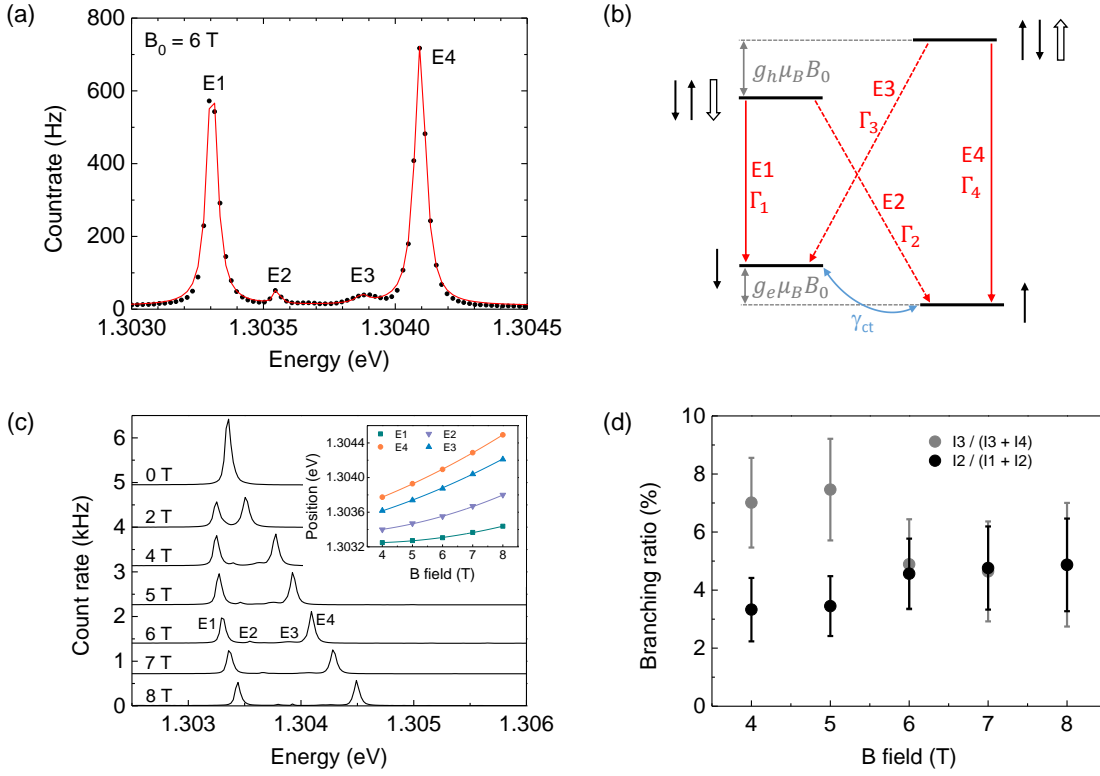


Fig. B.3. **Branching ratio and g-factors** (a) PL from the  $X^{1-}$  transition recorded at  $B_0 = 6 \text{ T}$  and  $V_g$  corresponding to maximum co-tunneling. Spectral positions  $E_i$  and intensities  $I_i$  for the four transitions are determined with a multiple peak fit (solid line). (b) Energy levels for the  $X^{1-}$  ground and excited states, where single (double) arrows represent the electron (hole) spin states. Solid (dashed) red arrows indicate transitions allowed (forbidden) according to the optical selection rules. The forbidden transitions are enabled by a weak light hole contribution to the hole wave function.  $\Gamma_i$  denote the transition rates and  $\gamma_{ct}$  the electron spin flip rate of the ground states resulting from co-tunneling to the back contact. (c)  $X^{1-}$  PL for different external magnetic fields. Zeeman splitting and diamagnetic shift are observed. We determine electron  $g_e = -0.67 \pm 0.06$  and  $g_h = 1.59 \pm 0.06$ . (d) Branching ratios (see legend) are determined by comparing the intensities. With the knowledge of  $\Gamma_1 = \Gamma_4 \approx 1 \text{ GHz}$  we can determine the diagonal rates  $\Gamma_2 = \Gamma_3 \approx 50 \text{ MHz}$ . Since we do not observe spin pumping under resonant excitation the  $\gamma_{ct}$  also must be on the order of tens of MHz.

The diagonal transitions (dashed red arrows in Fig. B.3(b)) are in principle forbidden by the optical selection rules, but are enabled by a weak light hole contribution to the hole wave function. Knowing that the vertical transitions rates (solid red arrows in Fig. B.3(b)) are about 1 GHz/s we can determine the diagonal transition rates to be a few tens of MHz. The signature of spin pumping, a decrease of resonance fluorescence counts at the center of the  $X^{1-}$  plateau, is not observed (Fig. 3.5(a)). Hence we deduce that the co-tunneling rate  $\gamma_{ct}$ , which couples the spin split ground states, is of the same order as the diagonal transition rates.

## B.2 Theory: Decoherence of the nuclear spin ensemble

The work in this section was conducted by Franziska Maier and Daniel Loss.

### B.2.1 Decoherence rate of a single nuclear spin

In this section, we describe the dynamics of the transverse spin component of a single nuclear spin interacting with a narrowed nuclear spin bath in a quantum dot. The interaction between the nuclei is mediated by a single electron due to hyperfine interactions and we neglect effects due to the dipolar and quadrupole interactions of the nuclear spins. We consider a self-assembled quantum dot loaded with a single electron in a strong magnetic field pointing perpendicular to the substrate along  $z$ . The Hamiltonian used in this work,  $H \simeq H_0 + V$ , is only valid in large magnetic fields and corresponds to the effective Hamiltonian derived in Ref.<sup>3</sup>, where we omitted diagonal terms in  $V$ . The single terms read

$$H_0 = \epsilon_z S_z + \eta_z \sum_j I_j^z + S_z h_z, \quad (\text{B.1})$$

$$V = \frac{1}{8\omega} \sum_{j \neq l} A_j A_l \left[ \left( \frac{1}{2} + S_z \right) (I_j^- I_l^+ + I_l^- I_j^+) - \left( \frac{1}{2} - S_z \right) (I_j^+ I_l^- + I_l^+ I_j^-) \right]. \quad (\text{B.2})$$

Here,  $S_z$  is the  $z$  component of the electron spin operator,  $I_j^{z,\pm}$  ( $I_j^\pm = I_j^x \pm iI_j^y$ ) are the components of the nuclear spin operator of the  $j$ th nuclear spin, and  $\epsilon_z$  and  $\eta_z$  are the electron spin and nuclear spin Zeeman splitting, respectively. The Overhauser field in  $z$  direction is denoted by  $h_z = \sum_j A_j I_j^z$  with  $A_j = A\nu_0 |\psi(r_j)|^2$ , where  $A$  is the total hyperfine coupling constant,  $\nu_0$  is the volume of a single nucleus unit cell and

$\psi(r_j) = \psi(0)e^{-(r_j/a_B)^2/2}$  is the electron envelope function. Here, the effective Bohr radius  $a_B$  defines the total number of nuclear spins interacting with the electron spin,  $N_e$ . Eventually, the effective Zeeman splitting of the electron is given by  $\omega \approx \epsilon_z + \langle h_z \rangle = g\mu_B B + pIA$ , where  $g$  is the electron  $g$  factor,  $\mu_B$  is the Bohr magneton,  $B$  is the magnetic field along  $z$ ,  $p$  is the nuclear spin polarization and  $I$  denotes the nuclear spin. Following Refs.<sup>3,4</sup>, we describe the transverse nuclear spin dynamics of a single nuclear spin in the quantum dot. For factorized initial conditions, i.e.  $P_k\rho(0) = \rho(0)$  we are able to derive the exact Nakajima-Zwanzig general master equation<sup>5</sup>,

$$P_k\dot{\rho}(t) = -iP_kLP_k\rho(t) - i\int_0^t dt'\Sigma(t-t')\rho(t') \quad (\text{B.3})$$

with the memory kernel  $\Sigma(t) = -iP_kLe^{-iQ_kLt}Q_kLP_k$ . Here, we introduced a superoperator  $P_k$  that projects onto the subspace of a single nuclear spin  $k$  and is defined as  $P_k\mathcal{O} = \rho_{eI'}(0)\text{Tr}_{eI'}\mathcal{O}$ , with its complement  $Q_k = 1 - P_k$ . We have  $\rho(0) = \rho_e(0) \otimes \rho_I(0)$  and the density matrix  $\rho_{eI'} = \rho_e \otimes_{j \neq k} \rho_{i_j}$ . Furthermore,  $L = L_0 + L_V$  denotes the complete Liouvillian, where  $L_0\mathcal{O} = [H_0, \mathcal{O}]$  and  $L_V\mathcal{O} = [V, \mathcal{O}]$ , respectively. Assuming  $I = 1/2$ , we find in the Born approximation

$$\langle \dot{I}_k^+ \rangle_t = -i\omega_n \langle I_k^+ \rangle_t - i\int_0^t dt'\Sigma_{++}^{(2)}(t-t')\langle I_k^+ \rangle_{t'} \quad (\text{B.4})$$

where  $\omega_n = \eta_z + A_k[S_z]^{mm} - A_k^2/2\omega$ , with  $[S_z]^{mm}|m\rangle = S_z|m\rangle$ , and where  $\Sigma_{++}^{(2)}(t)$  is the matrix element of the memory kernel describing the transverse nuclear spin dynamics to second order in  $L_V$ . In Laplace space, the memory kernel is given by

$$\Sigma_{++}^{(2)}(s) = \frac{-i}{16\omega^2} \sum_{j \neq k} \frac{(c_+ + c_-)A_k^2 A_j^2}{s - i[\eta_z + A_j[S_z]^{mm} - A_j^2/2\omega]}, \quad (\text{B.5})$$

with the coefficients  $c_{\pm}$  defined in Ref.<sup>4</sup>. To remove fast oscillations in Eq. (B.4), we transform to a rotating frame with frequency shift  $\Delta\omega = -\text{Re}[\Sigma_{++}^{(2)}(s = i(\omega_n + \Delta\omega) + 0^+)]$  determined self-consistently, where  $0^+$  denotes a positive infinitesimal. In the Born-Markov approximation, the decoherence rate of a single nucleus  $k$  is given by  $\Gamma_k = -\text{Im}[\Sigma_{++}^{(2)}(s = i(\omega_n + \Delta\omega) + 0^+)]$ , see Ref.<sup>6</sup>, Appendix C. We find

$$\Gamma_k = \frac{A^3\nu_0^2}{4\pi^{5/2}\hbar\omega^2 a_B^6} e^{-3(r_k/a_B)^2} \frac{r_k}{a_B}. \quad (\text{B.6})$$

In Fig. B.4, we plot  $\Gamma_k$  for a realistic set of parameters as a function of  $r_k$ .

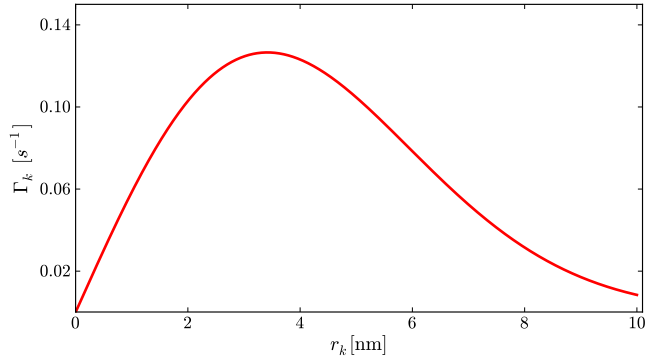


Fig. B.4. The decoherence rate  $\Gamma_k$  of a single nuclear spin  $k$  as a function of its position  $r_k$  in the quantum dot. Here, we assumed an In-concentration of 20% in the quantum dot,  $g = -0.7$ ,  $B = 6$  T,  $p = 0.5$ , and  $A_{\text{InGaAs}} = 87$   $\mu\text{eV}$ . Furthermore,  $\nu_0 = 23.5$   $\text{\AA}^3$  and  $N_e = 10^5$ , thus we obtain an effective Bohr radius  $a_B = 8.25$  nm.

## B.2.2 Coherence rate of a NMR signal

In NMR experiments, the combined signal of an ensemble of  $N$  nuclear spins is measured. We approximate the measured quantity,  $\langle I_N^+(t) \rangle$ , by

$$\langle I_N^+(t) \rangle \sim \sum_k \langle I_k^+(t) \rangle = \sum_k e^{-\Gamma_k t} \langle I_k^+(0) \rangle \propto \sum_k e^{-\Gamma_k t}, \quad (\text{B.7})$$

where the sum  $\sum_k$  runs over all nuclear spins contributing to the signal. In the last step, we assumed that  $\langle I_k^+(0) \rangle$  is constant over the dot. Note that the brackets describing the averaging,  $\langle \dots \rangle$ , correspond to different traces for  $I_N^+$  and  $I_k^+$ . For small times  $t$  with  $\Gamma_k t \ll 1$ , we find that

$$\langle I_N^+(t) \rangle \propto N - 1 + e^{-\hat{\Gamma}_N t} \quad (\text{B.8})$$

with

$$\hat{\Gamma}_N = \sum_k \Gamma_k = \frac{A^3 \nu_0}{18\pi^{3/2} \hbar \omega^2 a_B^3}. \quad (\text{B.9})$$

Inserting the parameters given below Fig. B.4, we find  $\hat{\Gamma}_N^{-1} \approx 117$   $\mu\text{s}$ . In Fig. B.5, we plot both the exact and approximated decay of  $\langle I_N^+(t) \rangle$ , again for the parameters given below Fig. B.4. We see that approximation captures the onset of the decay quite well, however, at  $t \sim 10^{-4}$  s, the approximation starts to deviate from the exact result. Interestingly, the exact result then evolves into a linear decay.

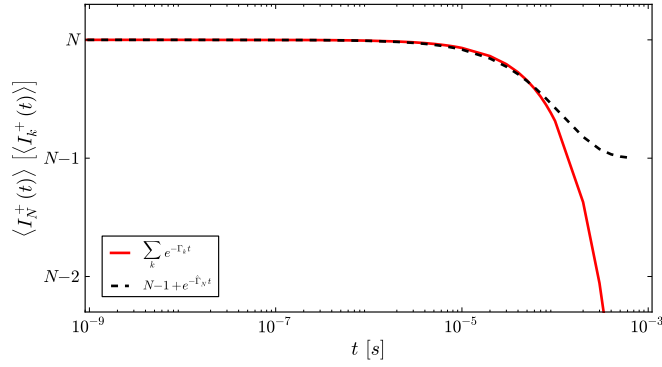


Fig. B.5. The NMR signal  $\langle I_N^+(t) \rangle$  as a function of  $t$ , where we compare the exact (red) and the approximated (black) decay. Here we used the same parameters as given below Fig. B.4.

## References

1. Chekhovich, E., Kavokin, K., Puebla, J., Krysa, A., Hopkinson, M., Andreev, A., Sanchez, A., Beanland, R., Skolnick, M., and Tartakovskii, A. *Nature Nanotechnology* **7**, 646–650 (2012).
2. Chekhovich, E., Hopkinson, M., Andreev, A., Skolnick, M., and Tartakovskii, A. *ArXiv preprint, arXiv:1403.1510v2* (2014).
3. Klauser, D., Coish, W. A., and Loss, D. *Phys. Rev. B* **78**, 205301 (2008).
4. Coish, W. A. and Loss, D. *Phys. Rev. B* **70**, 195340 (2004).
5. Fick, E. and Sauermann, G. *The Quantum Statistics of Dynamic Processes*. Springer-Verlag, Berlin, (1990).
6. Coish, W. A., Fischer, J., and Loss, D. *Phys. Rev. B* **77**, 125329 (2008).





# Appendix C

## Supplementary information to chapter 4

### C.1 Methods

**Nanowire growth** The nanowires were grown using a DCA P600 MBE machine. The nanowire core structures were obtained under rotation of 7 rpm at a temperature of 640°C under a flux of Ga equivalent to a planar growth rate of 0.03 nm/s and a V/III ratio of 60. The conditions were then switched from axial to radial growth by increasing the As pressure and reducing the substrate temperature. A 50 nm  $\text{Al}_x\text{Ga}_{1-x}\text{As}$  shell was grown with Al compositions  $x = 0.33, 0.51$  and  $0.70$  and capped with 5 nm GaAs to prevent oxidation. One sample was grown with alternating layers of GaAs/AlGaAs at  $x = 0.33$ .

**Electron microscopy** Cross-sections of the nanowires perpendicular to the growth axis were prepared by mechanical polishing and ion milling. 3D atomic models were obtained using the Rhodius software package<sup>1</sup> which allows complex atomic models to be created, including nanowire-like heterostructures<sup>2</sup>. High angle annular dark-field (HAADF) scanning transmission electron microscopy (STEM) analyses were performed in an aberration corrected probe FEI Titan 60-300 keV microscope. EDX analysis was performed using a FEI Tecnai OSIRIS microscope operated at 200 kV using the Super-X (0.9 radian collection angle) detector and Bruker Esprit software.

**Optical spectroscopy** The nanowires were transferred to a fresh silicon substrate and subsequently probed side-on. Cathodoluminescence was realized in an adapted scanning electron microscope<sup>3</sup>. Photoluminescence measurements were made with a confocal optical microscope with sample scanning, exciting with a low power HeNe laser at 632.8 nm or  $\text{Ar}^+\text{Kr}^+$  laser at 488 nm and 514 nm. The PL was dispersed with a monochromator-array detector system. PL in a bandwidth of 0.5 nm was sent to a Hanbury Brown-Twiss photon coincidence setup with two nominally identical silicon avalanche photodiodes.

The pulsed measurements (see SI) were performed with a Q-switched semiconductor laser diode at 635 nm using time-correlated single photon counting for recording the decay curve (SI).

**Pseudopotential calculations** The screened atomic potentials are adjusted by the empirical pseudopotentials method to correct for the DFT errors in band gaps, effective masses, inter-valley splittings and band offsets<sup>4</sup>. The single particle problem is solved numerically in a plane-wave basis, including spin-orbit (340 meV for GaAs), using the folded spectrum method<sup>5</sup> which allows eigensolutions to be obtained in a physically interesting energy window (about 300 meV from band edges) rather than at all energies. The calculation is carried out with a fixed potential without iterating to self-consistency.

**Self-consistent DFT calculations** Using linear-scaling density functional theory (DFT)<sup>6</sup>, as implemented in the ONETEP method<sup>7-9</sup>, which captures charge redistribution effects both efficiently and accurately<sup>10,11</sup>, we have performed simulations on structures containing 5,000 and 12,168 atoms (one of the largest fully self-consistent calculations ever performed). The 5,000 atom calculation was carried out by iteratively refining a compact real-space Wannier basis with respect to a primary plane-wave basis, whereas in the 12,168 atom calculation, the real-space basis was pre-optimized for isolated atoms, and thereafter fixed. In order to capture both the polar [121] and non-polar facets of the observed quantum-dots-in-nanowires, our simulation cells consist of fully-periodic slabs (1.3 nm thick, along the [1 - 11] direction) of an effective [1 - 21] wire. Simulations at the interface with the GaAs outer shell (Fig. 5) and with the Al<sub>0.3</sub>Ga<sub>0.7</sub>As nanowire core were separately carried out (see SI), using norm-conserving pseudopotentials, the local-density approximation (LDA)<sup>12</sup>, and random alloying at each stated concentration.

## References

1. Bernal, S., Botana, F. J., Calvino, J. J., Lopez-Cartes, C., Perez-Omil, J. A., and Rodriguez-Izquierdo, J. M. *Ultramicroscopy* **72**, 135–164 (1998).
2. Arbiol, J., Cirera, A., Peiro, F., Cornet, A., Morante, J. R., Delgado, J. J., and Calvino, J. *Appl. Phys. Lett.* **80**, 329–331 (2002).
3. Heiss, M., Gustafsson, A., Conesa-Boj, S., Peiro, F., Morante, J. R., Abstreiter, G., Arbiol, J., Samuelson, L., and Morral, A. F. i. *Nanotechnology* **20**, 075603 (2009).
4. Luo, J.-W., Bester, G., and Zunger, A. *Phys. Rev. B* **79**, 125329 (2009).
5. Wang, L. W. and Zunger, A. *J. of Chem. Phys.* **100**, 2394–2397 (1994).
6. Bowler, D. R. and Miyazaki, T. *Rep. Prog. Phys.* **75**, 036503 (2012).
7. Skylaris, C. K., Haynes, P. D., Mostofi, A. A., and Payne, M. C. *J. Chem. Phys.* **122**, 084119 (2005).
8. Hine, N. D. M., Haynes, P. D., Mostofi, A. A., and Payne, M. C. *J. Chem. Phys.* **133**, 114111 (2010).
9. Hine, N. D. M., Haynes, P. D., Mostofi, A. A., Skylaris, C.-K., and Payne, M. C. *Comput. Phys. Comms.* **180**, 1041–1053 (2009).
10. Avraam, P. W., Hine, N. D. M., Tangney, P., and Haynes, P. D. *Phys. Rev. B* **85**, 115404 (2012).
11. O'Regan, D. D., Hine, N. D. M., Payne, M. C., and Mostofi, A. A. *Phys. Rev. B* **85**, 085107 (2012).
12. Perdew, J. P. and Zunger, A. *Phys. Rev. B* **23**, 5048–5079 (1981).



# Appendix D

## Supplementary information to chapter 5

### D.1 Mechanical properties of the nanowire

We calculate the lowest order flexural vibrations and the induced dynamic strain of the nanowire (NW) using a finite element model (FEM) of the experimental system. We approximate the NW structure as an isotropic and homogeneous hexagonal prism of AlGaAs, with a density given by the average of the densities of the different GaAs and AlGaAs layers, each weighted according to its thickness (see main text). The dimensions of the NW as well as its length that is tightly glued to the Si substrate on a lateral facet are measured by scanning electron microscopy (SEM).

The FEM provides the eigenfrequencies of the NW flexural vibrations and the corresponding mode shapes. While a symmetric clamping of the NW would result in doubly degenerate vibrational modes, the asymmetry of the actual clamping geometry, i.e. with only one lateral facet in contact with the substrate, splits each mode into a doublet of flexural vibrations oriented either parallel or perpendicular to the Si surface, with the former having the lower eigenfrequency. Figure D.1 shows the mode shape of the lowest four non-degenerate vibrations. The spectral separation between two non-degenerate modes in each doublet depends, aside from the nature of the clamping, on the symmetry of the NW geometry: a dilatation of the hexagonal cross-section by only 1% along one axis is enough to invert the spectral positions of the two modes.

As discussed in the main text, in this experiment we focus our attention on the lowest order perpendicular mode. This orientation is preferentially driven by the piezoelectric transducer attached to the sample, is more easily detected by the interferometer, and driving higher order modes requires higher mechanical excitation power or a more sensitive displacement detection. The calculation of the mode shape of the favored flexural mode  $u_{\perp}(\mathbf{r})$  as a function of the position  $\mathbf{r}$  allows us to determine the corresponding

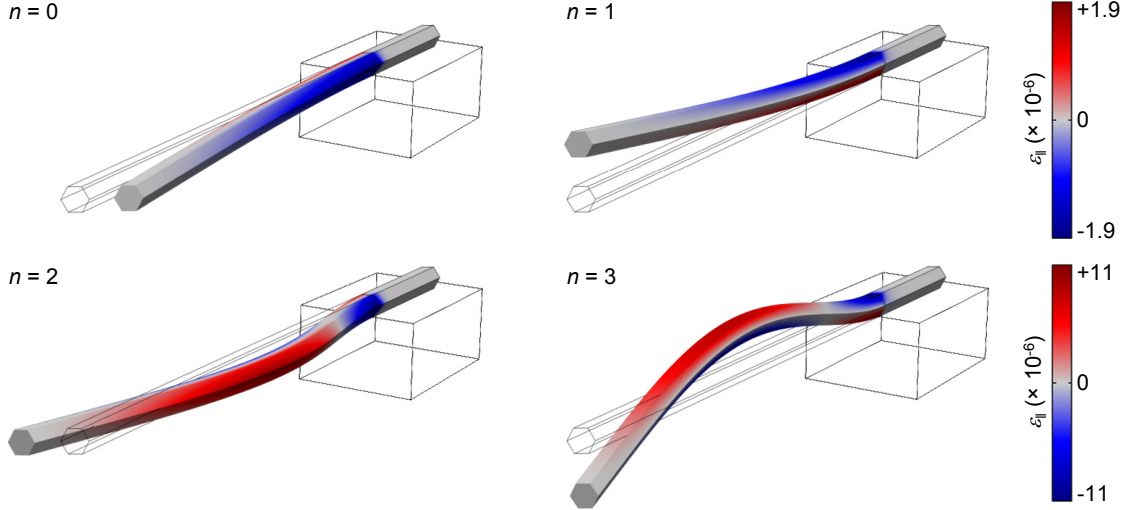


Fig. D.1. **FEM of the NW mechanical properties.** Each subfigure shows the mode shape of the lowest four non-degenerate vibrations,  $n$  being the mode index. The colour scale is proportional to the component  $\varepsilon_{||}$  of the material strain in the NW, for a 1-nm displacement of its free end.

motional mass  $m$  at the NW free-end, according to the definition:

$$m \equiv \int \rho |u_{\perp}(\mathbf{r})|^2 dV, \quad (\text{D.1})$$

where the integral is calculated over the entire NW volume  $V$ ,  $\rho$  is the NW density, which in our model does not depend on  $\mathbf{r}$ , and  $u_{\perp}(\mathbf{r})$  is normalized so that its maximum value is unity<sup>1</sup>. The result is  $m = (3.5 \pm 0.7) \times 10^{-15}$  kg, where the error is dominated by the measurement imprecision of the NW thickness.

The flexural vibrations produce a time-varying material strain in the NW, which translates into a dominant uniaxial stress along the NW growth direction ( $[1 \bar{1} 1]$  in crystallographic notation). This oscillating material strain is responsible for the modulation of the QD emission energy, therefore it is important to evaluate its strength and its spatial distribution. For this purpose, it is necessary to determine the values of the Young's modulus  $E_Y$  and of the Poisson's ratio  $\nu$ , which fully characterize the elastic properties of isotropic materials<sup>2</sup>.

To our knowledge, for a GaAs/AlGaAs nanostructure grown along  $\langle 111 \rangle$ ,  $E_Y$  has not yet been measured. The only reference is the value along this axis measured for bulk GaAs (141.2 GPa)<sup>3</sup>. For this reason, we initially set  $E_Y$  as a free parameter in our FEM, while calculating the NW eigenfrequencies. We then tune  $E_Y$  in the FEM

until the calculated resonance frequency of the lowest perpendicular mode matches our experimentally measured value of 795.4 kHz. The corresponding Young's modulus is  $E_Y = 153$  GPa, which is 8% larger than the aforementioned value measured for bulk GaAs. Possible reasons for this increase of the stiffness of our NW reside in its finite size and in its core-shell structure, which introduces an additional intrinsic material strain.

The Poisson ratio expresses the relative strength of the strain tensor components. By setting an  $xyz$  reference system with  $\hat{z}$  oriented along the NW growth direction, the strain tensor in our case assumes the following form:

$$\varepsilon_{ij} = \begin{bmatrix} \varepsilon_{\perp} & 0 & 0 \\ 0 & \varepsilon_{\perp} & 0 \\ 0 & 0 & \varepsilon_{\parallel} \end{bmatrix}. \quad (\text{D.2})$$

In this reference system, the Poisson's ratio can be written as follows:

$$\nu = -\frac{\varepsilon_{\perp}}{\varepsilon_{\parallel}}. \quad (\text{D.3})$$

Signorello *et al.*<sup>4</sup> have recently measured  $\nu$  for Zinc-Blende GaAs/AlGaAs core-shell NWs grown along  $\langle 111 \rangle$ , as in our case, at a temperature of 100 K (see Table D.1).

Once these fundamental parameters have been inserted into our FEM, we compute the strain distribution along the NW structure. Figure D.1 shows in color scale  $\varepsilon_{\parallel}$  for the lowest four non-degenerate flexural vibrations, for a NW free-end displacement of 1 nm. The largest strain is obtained at the clamped end of the NW, at the borders of its hexagonal cross-section perpendicular to the oscillation direction. The mode doublet described by the indices  $n = 2$  and 3 results in a maximum strain at the clamped end

| Parameter | Value           | Unit |
|-----------|-----------------|------|
| $\nu$     | $0.16 \pm 0.04$ |      |
| $a$       | $-8.6 \pm 0.7$  | eV   |
| $d$       | $-5.2 \pm 0.7$  | eV   |

Table D.1. Electro-mechanical material parameters. The values have been measured for Zinc-Blende GaAs/AlGaAs core-shell NWs grown along  $\langle 111 \rangle$ , at a temperature of 100 K. Taken from Ref. 4.

that is a factor 6 larger than the value of the lower index doublet. As confirmed by the FEM analysis, flexural modes of even higher index result in a further increase of the strain at the clamped end. Improvements in the detection of these higher modes should provide an opto-mechanical coupling parameter increased as the strain. However, the coupling rate  $\lambda$  defined in the main text also depends on the NW's zero-point motion  $x_{\text{ZPF}} = \sqrt{\hbar/(2m_n\Omega_n)}$ . While the mode motional mass  $m_n$  does not depend in our geometry on  $n$ , the mode resonance frequency  $\Omega_n$  increases with  $n$ , by a factor 6 for the second order doublet with respect to the first one. This dependence implies an increase of  $\lambda$  by a factor 2 (or bigger) for the second order (or higher) flexural modes of the NW.

## D.2 Effect of strain on the exciton transition energy

The application of mechanical strain to the NW alters the lattice constant and the symmetry of the solid. These effects, in turn, cause significant changes in the electronic band structure that manifest themselves in the optical properties. The hydrostatic and shear components of the strain both contribute to such opto-mechanical coupling, with a weight given by their respective deformation potential, conventionally indicated as  $a$  for the hydrostatic deformation and  $d$  for the shearing induced by a stress along  $\langle 111 \rangle$ <sup>5,6</sup>. The aforementioned work of Signorello *et al.*<sup>4</sup> has obtained these deformation potentials for NWs similar to ours (but without embedded QDs); the measured values are reported in Table D.1.

The brightest exciton transition in our QDs concerns the conduction and the heavy-hole bands, each responding in a different way to the applied strain. The variation of the energy gap between these bands ( $\Delta E^{\text{C-HH}}$ ) under mechanical excitation can be connected to the strain component  $\varepsilon_{\parallel}$  through the following model<sup>5</sup>:

$$\Delta E^{\text{C-HH}} = \left[ (1 - 2\nu)a + \frac{1}{\sqrt{3}}(1 + \nu)d \right] \varepsilon_{\parallel}. \quad (\text{D.4})$$

From the FEM of the NW, we extract the profile of  $\varepsilon_{\parallel}$  along  $\hat{z}$  corresponding to the lowest order perpendicular mode, for a given displacement of the NW free end. The graph in Fig. D.2 shows such a plot for  $\varepsilon_{\parallel}$  at 10 nm below the NW surface, a distance where the QDs best coupled to strain are located. The red spot, in particular, marks the position where the QDs analyzed in the main text are placed,  $2.0 \pm 0.3 \mu\text{m}$  away from the clamped edge of the NW. Inserting the value of  $\varepsilon_{\parallel}$  at the QD position into the Eq. D.4, we obtain a displacement-dependent energy shift of  $13 \pm 2 \mu\text{eV/nm}$ . Though this estimation does not take into account the detailed QD band structure, the value we



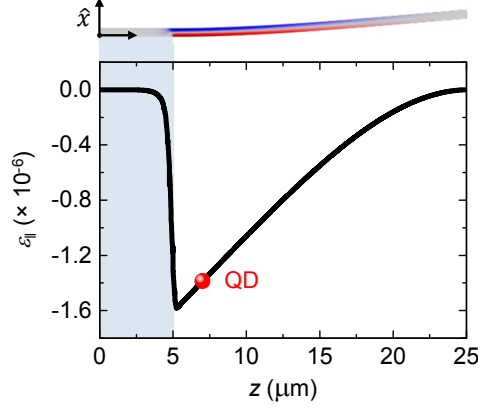


Fig. D.2. **Strain profile along  $\hat{z}$ .** The strain component  $\varepsilon_{||}$  at 10 nm below the NW surface is plotted for the NW free-end displaced through  $u_{\perp}$  by 1 nm along  $\hat{x}$ . The shaded area from  $z = 0$  to  $z = 5 \mu\text{m}$  marks the region of the NW which is clamped to the substrate. The red spot at  $z = 2.0 \pm 0.3 \mu\text{m}$  from the edge of the clamped region marks the position where the QDs analyzed in the main text are located. The upper inset shows the mode shape in consideration, with the strain amplitude in color scale as in Fig. D.1.

have found is close to our experimental result ( $9.9 \pm 0.7 \mu\text{eV}/\text{nm}$ ), therefore confirming the strain-dependence of the band structure as the dominant coupling mechanism.

### D.3 Distribution of the exciton energy shifts

We analyze the distribution of energy shifts of PL lines from QDs located in the same position along the NW length (within the laser detection spot), and emitting in a spectral range of 30 meV centered around 1.860 eV. This relatively narrow energy window restricts our analysis to QDs with similar size and composition. We consider the energy shift induced in the QDs by a resonant mechanical excitation of the NW. In order to exclude the effect of asymmetric energy modulation, due to the different response of the QD band structure under compressive or tensile stress<sup>4,7</sup>, we consider energy shifts only towards higher energies. The distribution of the data is plotted in Fig. D.3(a).

The experimental result is compared to two different models for the spatial distribution of the QDs in the shell of the NW. The first model, illustrated in Fig. D.3(b), assumes QDs located at the apexes of the NW hexagonal cross-section. The histogram in Fig. D.3(c), instead, results from a model of QDs uniformly distributed along the shell perimeter.

The experimental distribution conforms more closely to the model of QDs located at

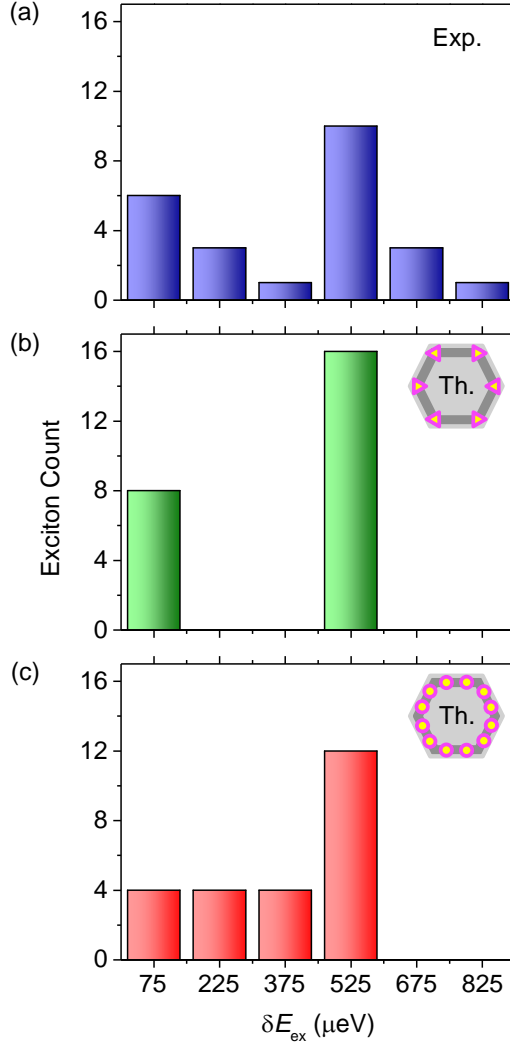


Fig. D.3. **Distributions of energy shifts.** (a) Experimental distribution of energy shifts for QDs emitting within a 30-meV spectral range and located at the same position along the NW length. (b) Model distribution for QDs located at the apexes of the NW shell. (c) Model distribution for QDs uniformly distributed along the shell perimeter. The two model distributions are normalized to the total exciton count of the experimental analysis.

the apexes of the cross-section. Though not conclusive, this analysis lends support to the interpretation of the QD spatial distribution in our NW structures originally given by Heiss *et al.*<sup>8</sup> and recently confirmed by Fontana *et al.*<sup>9</sup>. The observed deviations from such a model can be explained as weak fluctuations of size and composition of the analyzed QDs<sup>10</sup>, and to different distances from the center of the cross-section.

## D.4 Interferometric displacement detection

We use a 780-nm laser interferometer to detect the displacement of the NW free-end. Due to the low finesse of our cavity, the interferometer fringe as a function of the cavity length or of the laser wavelength is well approximated by a sinusoid. The NW oscillation modulates the interferometer response in a small range around the fringe average, where the response becomes linear. We stabilize the interferometer in this linear regime, by controlling the laser wavelength via a PID feedback loop.

The cavity free spectral range measures  $(2.6 \pm 0.1) \times 10^{-13}$  m, from which we derive a cavity length of  $118 \pm 5$  cm. Measurements of the NW displacement are calibrated by an accurate determination of the laser wavelength. In order to double-check this calibration, we measure the displacement amplitude  $A_{\text{osc}}$  of the positioning stage along  $\hat{x}$ , while the stage is driven by a low-frequency oscillation (117 Hz). As shown in Fig. D.4, the measurement is repeated for several drive voltages in order to extract, through a linear fit, a conversion factor for the piezoelectric positioning stage equal to  $11.6 \pm 0.1$  nm/V. The entire procedure is repeated with the interferometer aligned to a variety of different positions on the  $yz$  plane, including the position of the NW free end. The values measured using our interferometer are close to the specifications of the positioning stage, which provide a rough conversion factor of 8 nm/V.

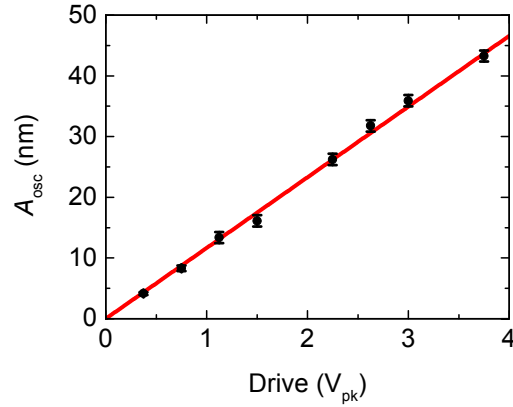


Fig. D.4. **Interferometer test.** Amplitude of the positioning stage displacement oscillation at 117 Hz as a function of the amplitude of the drive voltage, measured at a temperature of 4.2 K. The error bars correspond to the peak-to-peak amplitude of the interferometric noise. The red line is a linear fit, from which we extract a conversion factor of  $11.6 \pm 0.1$  nm/V.

## D.5 Displacement, force, and strain sensitivities

The sensitivity of the QDs in our system to the resonant vibration of the NW could be used to reveal displacement variations due to the application of electrical or magnetic forces or to a change of the NW mass.

We estimate the sensitivity of our apparatus as a displacement transducer and as a force or strain detector. To this purpose, we first measure, for a QD emission line, the intrinsic fluctuation in time of the photon count in a narrow spectral bin around the transition energy  $E_{\text{ex}}^0$ . The amplitude of such fluctuation depends on the bin size and on the integration time  $\tau$ . An external force applied to the NW produces, through the deformation potential coupling, a variation of the QD photon count in a given spectral interval. For such a force to be detectable, the induced photon count variation has to be bigger than the intrinsic fluctuation. This count variation is in turn a direct consequence of the emission energy modulation, whose amplitude  $\delta E_{\text{ex}}$  can be calculated through the model described in the main text. From the opto-mechanical coupling parameter  $\left. \frac{\partial E_{\text{ex}}}{\partial x} \right|_{x=0}$  measured for QD 2, we are then able to convert the emission energy modulation into a root-mean-squared displacement  $x_{\text{rms}}$  of the NW free-end. Finally, by multiplying such displacement to the square root of  $\tau$ , we obtain a displacement sensitivity  $\approx 3 \text{ nm Hz}^{-1/2}$ . Note that this result is limited, in particular, by the resolution of our spectrometer, equal to  $60 \mu\text{eV}$ . On the other hand, the sensitivity could be improved by 4 orders of magnitude by means of resonant laser spectroscopy<sup>11</sup>.

The applied force is proportional to the NW displacement  $x_{\text{rms}}$  through the spring constant  $k = m\Omega_0^2 = 90 \pm 20 \text{ mN/m}$ . Therefore we are able to estimate a force sensitivity  $\approx 300 \text{ pN Hz}^{-1/2}$ .

Our setup is also sensitive to strain variations in the NW. The finite element model described in Section D.1 relates the strain to the NW displacement. It is then possible to express a strain sensitivity of our setup,  $\approx 5 \times 10^{-6} \text{ strain Hz}^{-1/2}$ . This result is of the same order of the sensitivity recently estimated for strain-mediated coupling of a diamond cantilever to the spin of an embedded nitrogen-vacancy center<sup>12</sup>.

## References

1. Hauer, B. D., Doolin, C., Beach, K. S. D., and Davis, J. P. *Ann. Phys.* **339**, 181–207 (2013).
2. Cleland, A. N. *Foundations of Nanomechanics*. Eds. Springer: Berlin, (2003).
3. Brantley, W. A. *J. Appl. Phys.* **44**, 534–535 (1973).
4. Signorello, G., Karg, S., Björk, M. T., Gotsmann, B., and Riel, H. *Nano Lett.* **13**, 917–924 (2013).
5. Chandrasekhar, M. and Pollak, F. H. *Phys. Rev. B* **15**, 2127–2144 (1977).
6. Van de Walle, C. G. *Phys. Rev. B* **39**, 1871–1883 (1989).
7. Bryant, G. W., Zieliński, M., Malkova, N., Sims, J., Jaskólski, W., and Aizpurua, J. *Phys. Rev. B* **84**, 235412 (2011).
8. Heiss, M., Fontana, Y., Gustafsson, A., Wüst, G., Magen, C., O’Regan, D. D., Luo, J. W., Ketterer, B., Conesa-Boj, S., Kuhlmann, A. V., Houel, J., Russo-Averchi, E., Morante, J. R., Cantoni, M., Marzari, N., Arbiol, J., Zunger, A., Warburton, R. J., and Fontcuberta i Morral, A. *Nature Mater.* **12**, 439–444 (2013).
9. Fontana, Y., Corfdir, P., Van Hattem, B., Russo-Averchi, E., Heiss, M., Sonderegger, S., Magen, C., Arbiol, J., Phillips, R. T., and Fontcuberta i Morral, A. **2014**, (2014).
10. Jöns, K. D., Hafenbrak, R., Singh, R., Ding, F., Plumhof, J. D., Rastelli, A., Schmidt, O. G., Bester, G., and Michler, P. *Phys. Rev. Lett.* **107**, 217402 (2011).
11. Kuhlmann, A. V., Houel, J., Ludwig, A., Greuter, L., Reuter, D., Wieck, A. D., Poggio, M., and Warburton, R. J. *Nature Phys.* **9**, 570–575 (2013).
12. Ovarthaiyapong, P., Lee, K. W., Myers, B. A., and Bleszynski Jayich, A. C. **2014**, (2014).



# Acknowledgements

First and foremost I would like to thank Richard Warburton for accepting me as a PhD student in his group. Your passion for physics, creativity and great experience are the rock on which this work was built. I would also like to thank Val Zwiller for reading and co-refereeing my thesis on rather short notice.

Many thanks to all the members of the nano-optics group. In particular I would like to highlight the great team spirit during the build-up phase: Andreas, Julien, Lukas, Jonathan it was a great honour and a lot of fun setting up the labs with you guys. Also, I would like to thank Mathieu for his co-work on the NMR project. Many thanks go to Martino for sharing his great expertise on how to set-up and interpret the NMR experiments, to Fei for showing me some very useful tricks in the micro wire fabrication process and to Michele for his co-work on the opto-mechanical coupling project. In addition, I would like to thank the mechanical and electronic workshop for their fast and excellent work. Moreover, I would like to thank Daniel and Franziska for their work on the RKKY theory.

Furthermore, I would like to thank Andreas Wieck and Anna Fontcuberta i Morral and their group members for supplying the samples used in this work.

Last, but not least I would like to thank my family for their love and support throughout my whole life.





# Curriculum Vitae

## Gunter Wüst

Belchenstrasse 11  
4054 Basel  
Switzerland

## Background

*Birth:* 27th February 1983, Kandel, Germany  
*Citizenship:* German

## Education

- 2015 PhD in Experimental Physics  
University of Basel, Switzerland  
Advisor: Prof. Richard J. Warburton  
Thesis: *Nuclear magnetic resonance on a single quantum dot and a quantum dot in a nanowire system: quantum photonics and opto-mechanical coupling*
- 2010 Diploma in Physics  
Karlsruhe Institute of Technology  
Advisor: Prof. Heinz Kalt  
Thesis: *Feinstrukturuntersuchungen sowie Kernspinpolarisation durch optische und elektrische Anregung an einzelnen Halbleiterquantenpunkten*
- 2008 MPhys in Physical Science  
Heriot-Watt University, Edinburgh, UK  
Advisor: Prof. Richard J. Warburton  
Thesis: *Resonant laser transmission spectroscopy on a single semiconductor quantum dot*
- 2002 Abitur at the Alfred Grosser Gymnasium, Bad Bergzabern, Germany



# List of Publications

(\*) Publication covered in this thesis.

1. D. Brunner, B. D. Gerardot, P. A. Dalgarno, G. Wüst, K. Karrai, N. G. Stoltz, P. M. Petroff, and R. J. Warburton,  
*A Coherent Single-Hole Spin in a Semiconductor*,  
Science **325**, 70-72 (2009).
2. P. Asshoff, G. Wüst, A. Merz, D. Litvinov, D. Gerthsen, H. Kalt, and M. Hetterich,  
*Nuclear spin polarization in single self-assembled  $In_{0.3}Ga_{0.7}As$  quantum dots by electrical spin injection*,  
Phys. Rev. B **84**, 125302 (2011).
3. (\*) M. Heiss, Y. Fontana, A. Gustafsson, G. Wüst, C. Magen, D. D. O'Regan, J. W. Luo, B. Ketterer, S. Conesa-Boj, A. V. Kuhlmann, J. Houel, E. Russo-Averchi, J. R. Morante, M. Cantoni, N. Marzari, J. Arbiol, A. Zunger, R. J. Warburton, and A. Fontcuberta i Morral,  
*Self-assembled quantum dots in a nanowire system for quantum photonics*,  
Nature Mater. **12**, 439 (2013).
4. (\*) M. Munsch, G. Wüst, A. V. Kuhlmann, F. Xue, A. Ludwig, D. Reuter, A. D. Wieck, M. Poggio, and R. J. Warburton,  
*Manipulation of the nuclear spin ensemble in a quantum dot with chirped magnetic resonance pulses*,  
Nature Nano. **9**, 671-675 (2014).
5. (\*) M. Montinaro, G. Wüst, M. Munsch, Y. Fontana, E. Russo-Averchi, M. Heiss, A. Fontcuberta i Morral, R. J. Warburton, and M. Poggio,  
*Quantum Dot Opto-Mechanics in a Fully Self-Assembled Nanowire*, Nano Letters **14**, 4454-4460 (2014).